Università degli Studi di Ferrara

DOCTORAL COURSE IN ENGINEERING SCIENCE

CYCLE XXXIV

COORDINATOR Prof. Stefano Trillo

THE IWC METHOD IN THE ANALYSIS OF TURBULENCE: FIRE RELATED FLOWS

Scientific/Disciplinary Sector (SDS) ING/IND 10

Candidate
Dott. Francesco Saverio Ciani

Supervisor
Prof. Stefano Piva

Co-supervisor
Prof. Nicola Prodi

Year 2018/2021

*To my beloved wife Sonia and
my newborn daughter Aurora.*

ABSTRACT

Nowadays, the use of the Computational Fluid Dynamics (CFD) allows to analyse fire scenarios otherwise expensive to conduct experimentally or too complex to assess with analytical solutions. During the assessment of fire structural resistance and of occupants' life safety, the study of the fire plume and its ceiling jet is a critical task. Here, a test case concerning these two flows is numerically addressed using the *LES* code Fire Dynamics Simulator (FDS).

The aim of the thesis is to gain an insight into the physics of the time and length scales of the two flows, with regard to the characteristics of the code, its turbulence solver approach and the choice of the grid. To this aim, a spectral analysis is discussed in both the frequency and wavenumber domains for three different grids. If the spectral analysis in the frequency domain simply involves the use of the Fourier Transform, in the wavenumber domain the methodology to obtain the spectra is more challenging due to some limitations in the use of the direct method or in the Taylor's hypothesis for the fire related flows: inhomogeneous turbulence, high turbulence intensity and lack of a large number of points closely spaced. We present a viable alternative using the Inhomogeneous Wave Correlation (IWC) method, which looks for the frequency/wavenumber correlation, avoiding physical models and their limitations. Special care in the spectral analyses is given to assess the influence of the implicit filtering used in FDS, the quality of the grids and the power law in the inertial subrange of the spectra.

The analyses show that for the test case the inertial sub-range of the specific turbulent kinetic energy spectra follows the Kolmogorov power law. The use of the coarser grid, even following the rule of thumb proposed by the FDS user guide, brings to a restricted extension of the inertial sub-range for the plume, and to grid dependent results for the ceiling jet. For our plume and its ceiling jet, practical rules able to predict the cutoff frequencies and wavenumbers in the spectra are developed. The IWC method allows to obtain a correlation between the frequencies and wavenumbers that is not in

agreement with the Taylor's hypothesis for both the flows. Thus the phase and group velocity do not coincide. Furthermore, the IWC method has the attractive advantage of pointing out the differences in the turbulence dissipation behaviour between the fire plume and the following ceiling jet.

SOMMARIO

L'applicazione della termo-fluidodinamica numerica (CFD) all'ambito della *Fire Safety Engineering* consente di analizzare scenari di incendio altrimenti eccessivamente costosi da riprodurre sperimentalmente o troppo complessi da valutare con soluzioni analitiche. La valutazione della resistenza delle strutture e dell'incolumità degli occupanti in caso di incendio verte principalmente sullo studio di due moti: il *plume* e il *ceiling jet*. In questa tesi, si è affrontato un caso di studio riguardante proprio tali moti utilizzando il codice *Fire Dynamics Simulator (FDS)*, il quale adotta per la turbolenza la formulazione *Large Eddy Simulation (LES)*.

Lo scopo della tesi è quello di analizzare le scale temporali e spaziali dei due moti, tenendo in considerazione le caratteristiche del codice numerico, il suo approccio alla turbolenza e la scelta della griglia. A tale scopo, si è eseguita un'analisi spettrale sia nel dominio delle frequenze che in quello dei numeri d'onda su tre griglie differenti. L'analisi spettrale nel dominio delle frequenze prevede semplicemente l'uso della trasformata di Fourier, mentre nel dominio dei numeri d'onda le metodologie per ottenere tali spettri sono più impegnative. L'impiego diretto della trasformata di Fourier sui dati spaziali richiede, per ottenere risultati soddisfacenti, che i dati siano ottenuti in punti molto ravvicinati tra di loro, mentre l'adozione dell'ipotesi di Taylor è limitata a moti con turbolenza omogenea ed a bassa intensità di turbolenza, condizioni generalmente non soddisfatte nei moti tipici dell'incendio. A fronte di tali criticità, in questa tesi, si è riconosciuta come valida alternativa l'utilizzo del metodo *Inhomogeneous Wave Correlation (IWC),* che individua la correlazione frequenza/numero d'onda, evitando modelli fisici e le rispettive limitazioni. Le analisi spettrali sono state svolte ponendo particolare attenzione sull'influenza della filtrazione implicita di *FDS* sugli spettri, sulla qualità delle griglie e sulla legge di potenza nel *sub-range* inerziale negli spettri.

Le analisi eseguite hanno dimostrato che, per il nostro caso il *sub-range* inerziale degli spettri dell'energia cinetica turbolenta specifica segue la legge di potenza di Kolmogorov. L'uso della griglia più lasca, pur seguendo la regola pratica proposta dal

manuale di *FDS*, ha portato, nel nostro caso, ad un'estensione ristretta del *sub-range* inerziale degli spettri relativi al *plume*, e a risultati *grid-dependent* per il *ceiling jet*. Per entrambi i moti si sono sviluppate regole pratiche in grado di prevedere le frequenze e i numeri d'onda di *cut-off* negli spettri. Il metodo *IWC* ha consentito l'ottenimento di una correlazione tra frequenze e i numeri d'onda, che si è rivelata non essere in accordo con l'ipotesi di Taylor con la conseguenza che le velocità di fase e di gruppo non coincidono. Inoltre, il metodo *IWC* ha dimostrato l'interessante vantaggio di evidenziare le differenze tra *plume* e *ceiling jet* in termini di dissipazione della turbolenza.

ACKNOWLEDGMENT

CONTENTS

LIST OF FIGURES

LIST OF TABLES

NOMENCLATURE

$\langle\ \rangle$	time-averaged
a	constant in the fitting function (m^{-1});
b	constant in the fitting function ($m^{-1}s^{-1}$);
c	constant in the fitting function (s^{-1});
c_p	specific heat at constant pressure(J/K kg);
CHRR	cumulative heat release rate (kW)
d	distance from the centre-line (m);
D	characteristic length (m);
D*	fire characteristic diameter (m);
DFT	Discrete Fourier Transform;
F	Fourier Transform;
f	frequency (Hz);
FFT	Fast Fourier Transform;
g	gravity acceleration (m/s^2);
ht	height from the burner to the ceiling (m)
H	number of points for the discretization in the direction x_1 (-);
HRR'	heat release rate per unit length (kW/m);
HRRPUV	heat release rate per unit volume (kW/m^3)
I	turbulence intensity (-)
IWC	Inhomogeneous Wave Correlation;
J	number of frequency step (-);
k	wavenumber (m^{-1});
K	number of time step (-);
L	hydraulic diameter of the burner (m);
LH	flame height (m);
$\bar{n}$	versor normal to the considered plane having surface S

per	perimeter (m)
PSD	Power Spectral Density;
psd	half of the sum of the PSDs of the fluctuating velocity component (m^2/s);
q'''	specific heat release rate (kW/m^3)
Q	number of points for the discretization in the direction x_2 (-);
$\dot{Q}$	maximum heat release rate (kW);
Q*	non dimensional heat release rate (-);
$\bar{r}$	the pointing vector centred in the source of the signal
R	two times correlation function of the fluctuating velocity components (m^2/s^2);
Re	Reynolds number (-);
S	surface (m^2)
t	time (s)
T	temperature (K);
tke	turbulent kinetic energy (m^2/s^2);
TKE	Fourier Transform of the turbulent kinetic energy (m^2/s^2);
$\bar{u}$	velocity vector (m/s);
$\tilde{u}$	velocity components (m/s);
U	time-averaged velocity components (m/s);
V	group or phase velocity
u	velocity component fluctuations (m/s);
w	generic signal (-);
W	Fourier Transform of the generic signal w (-);
x	component of the position vector (m);

Greek Symbol

Δx	uniform grid size (m);
Δ	filter size size (m);

η	second coefficient of the McCaffrey analytical model;
χ	first coefficient of the McCaffrey analytical model;
ν	kinematic viscosity (m^2/s^2)
φ	carbon dioxide concentration fraction (-);
ρ	air density (kg/m^3);
σ	inhomogeneous general wave;

Subscript

1,h	discrete along the direction x_1;
2,q	discrete along the direction x_2;
3, d	vertical stream-wise direction of the dissipative wavenumber;
3,m	discrete along the direction x_3;
3, n	vertical stream-wise direction of the position vector, related to a sector of annulus;
3, p	vertical stream-wise direction of the propagative wavenumber;
3, d	discrete along the direction x_3 for the flame height calculation;
Alpert	calculated with the Alpert's model;
bulk	bulk average;
c	lower limit of the of the attenuated region;
cj	ceiling jet
CO2	derived from the carbon dioxide concentration along the x_1-axis;
CO2,D	carbon dioxide concentration along the x_1-axis at the characteristic length scales;
CO2,min	minimum value of carbon dioxide concentration along the x_1-axis;
CO2,max	maximum value of carbon dioxide concentration along the x_1-axis;
d	dissipative
fc	upper limit of the attenuated region;
FDS	derived from the cutoff defined by the FDS User Guide;
FDS/2	derived from the cutoff defined by the FDS, and divided by 2;
g	group

h	hydraulic
i	direction of the axis (1,2,3);
IWC	calculated with the correlation law;
j	discrete in frequency;
k	discrete in time;
L,m	discrete along the longitudinal direction;
L,p	longitudinal direction, propagative;
L,d	longitudinal direction, dissipative;
m	discrete in space;
McCaffrey	calculated with the McCaffrey's analytical model;
n	index of the sector of annuli
p	propagative;
ph	phase;
PL	time-averaged HRR in the time interval $20\,s \leq t_k \leq 100\,s$;
sgs	related to the subgrid model;
U/2	associated to the point where it is reached the half of the maximum vertical component of the time-averaged velocity;
T/2	associated to the point where it is reached the half of the maximum vertical component of the time-averaged temperature;
S-C	from square to circular burner;
$\pi/2$	divided by the factor $\pi/2$;
∞	far field;

Chapter 1

INTRODUCTION

In events of fire in civil or industrial buildings, fire "plumes" of hot gases, soots and aerosols, produced by the incomplete burning of combustibles in fire sources, rise by buoyancy. When the hot gases and the incomplete combustion products of a plume impinge on a horizontal ceiling surface, they deviate, flow along the ceiling, and the plume turns into a "ceiling jet" [1-5]. The study of this configuration is necessary during the assessment of fire structural resistance and of occupants' life safety. Fire plumes and ceiling jets are usually characterised by reacting flows, turbulence, and buoyancy and hence are complex phenomena.

In the plume, over the fire source, a buoyancy force driving upwards the combustion products is induced by the temperature difference between flame and surrounding air, the "smoke plume zone" [1]. This typically shows a truncated cone pattern starting from the source of the fire (Morton [6]). The region around the plume, where the flow interacts with the solid ceiling, is named "turning zone" (Alpert [7]). As the flow moves away from the impingement area, the ceiling jet begins [8]. It consists of a flow of hot combustion products in the shallow layer below the ceiling surface, driven by the momentum of flowing products moved by buoyancy. In flows of practical interest, both plume and its ceiling jet are turbulent.

The open source CFD code "Fire Dynamics Simulator" (FDS in the following) is commonly used for the numerical modelling of these flows. The code is characterized by a turbulent LES solver able to show the evolution of flames and smoke and their turbulent nature. The LES approach allows to resolve the larger eddies and to model the finer ones. Except for the explicit filtering, the resolved scales are proportional to the dimension of the cells: the finer this size the finer the solved scale. This means that to solve highly turbulent flows, characterized by large and small characteristic dimensions connected by an extended inertial sub-range, and to show a significant number of turbulent structures,

a large number of cells and of time steps (FDS uses an explicit time solver) is needed. It is therefore important to understand where to place the bound between resolved and modelled turbulence.

1.1   SPECTRAL ANALYSIS IN A LES FRAMEWORK

Significant information on the bound between resolved and modelled turbulence in a LES code can be obtained with a spectral analysis of the specific turbulent kinetic energy (*tke* in the following) [9]. To gain an insight about the study of the spectra obtained by using the results of a LES code, an overview of the spectral analysis in turbulence, and the influence of the LES approach on the spectra are briefly described in Par 1.1.1 and Par 1.1.2, respectively.

1.1.1   Spectral Analysis of Turbulent Flows

At high Reynolds number the dynamics of flows is described by the existence of a vast number of length-scales, some of which play a specific role in the elucidation of these turbulent flows. In these flows a wide range of length scales occurs, bounded from above by the size of the flow field and from below by the diffusive effect of the viscosity [10]. The observation that a broad range of eddy sizes exists, and that dissipation is associated mainly with the finest eddies, led Richardson [11] to introduce the concept of the energy cascade for high Reynolds turbulence. Richardson's hypothesis states that, in a turbulent flow, the *tke* is continually passed down from large-scales to small scales, at which it is dissipated by viscous stresses. The Author [11] considered it as a multi-stage process involving a hierarchy of vortex sizes.

A further major feature of the turbulent flows is the randomness. This makes the application of a deterministic approach to turbulence problems impossible because of the difficulty to describe all the individual time variations in the parameter of interest such as velocity, pressure or temperature. Thus, the only possibility in the theory of turbulence is an approach based on a statistical elucidation [12]. Many of the fundamental ideas in the statistical theory of turbulence were formulated already in the 30's by Taylor. The Author

introduced the application to the turbulence of the concept of the "two points correlation function" at a certain time, between the fluctuating velocity components in a point and in the surroundings points, and its Fourier transform [13] (see Eq (A.1) in the Appendix A for more details). The "two points correlation function" allows to describe the evolution of a fluctuating function in order to know how the values at different locations are related. In the 1940s the statistical theory of turbulence was the subject of Kolmogorov's research [14-16] assuming homogeneous and isotropic turbulence. Kolmogorov's theory asserts that the statistical properties of the small scales depend only on the kinematic viscosity and on the rate at which energy is passed down the energy cascade. Furthermore, this theory states that, at high Reynolds numbers, the small scales are statistically isotropic and have structures, which are statistically universal [12].

The most used statistical tool for the turbulence elucidation is the spectral analysis [17]. In Taylor's paper [13], the Author also introduced the spectral representation of turbulence. In particular, He introduced the Fourier Transform of the "two point correlation function", named Power Spectral Density (PSD) in the wavenumber domain (see Eq. (A.2)). The analysis proposed by Taylor [13] in the space domain can be performed, analogously, for the time domain. In particular, the "two times correlation function" can be calculated in a point, between the fluctuating velocity component in an instant and in the other instants and its Fourier Transform is named PSD in the frequency domain (see Eqs. (A.3, A.4)).

The spectral analysis in the turbulence framework can be applied to many different variables, such as pressure, velocity, temperature or directly to *tke* (see Eq. (A.5)). One of the applications of the spectral analysis consists in the direct use of the Fourier Transform to the time history of the *tke* (see Eq. (A.6)), which allows to obtain a complex-valued function of frequency, whose magnitude represents the amount of that frequency present in the original *tke* time history, and whose argument is the phase offset of the basic sinusoid in that frequency. This application of the Fourier Transform to the time history of *tke* is not the only tool to investigate the *tke* properties. Thus, in the time domain framework, a spectrum is calculated (*psd*(f) in the following) that is the sum of the PSDs of the fluctuating velocity components multiplied by 0.5. The most important property of this spectrum regards its integral, which is the time-averaged *tke*. In the space domain, a

further spectrum can be calculated as explained in several textbooks [10 -11], and it is named 'three-dimensional spectrum'. The use of the 'three-dimensional spectrum' is not widespread due to its limitations to isotropic and homogeneous turbulence. For this reason, one-dimensional spectra are usually preferred, limiting the separating vector between the two points of the correlation function to one single direction.

Each of the above mentioned spectra may be divided into three ranges of frequencies or wavenumbers [10]:

- the energy-containing range,
- the inertial sub-range
- the dissipation range.

The energy-containing range shows the behaviour of the larger eddies that are characterized by anisotropy. Here, the larger eddies supply energy to the finer eddies and there is no viscous dissipation.

The inertial sub-range and its fundamental features were brought to light thanks to the pioneering work of Kolmogorov [14-16]. Kolmogorov demonstrated with the hypothesis of homogeneous and isotropic turbulence that when the Reynolds number is large enough, in a locally isotropic range of length scales named inertial sub-range, the statistical functions depend only on the dissipation rate and on a particular power law of frequency or wavenumber. It can be noted that the inertial sub-range has a $1/f^{\alpha}$ power law (or $1/k^{\alpha}$ in the wavenumber domain) dependence, which is typical of the fractal phenomena such as the one happening in the energy cascade, as described by Mandelbrot [18]. In particular the *psd(f)*, the three dimensional spectrum and the one dimensional spectrum follow the "-5/3 power law". The "-5/3 power law" is often attributed to Kolomogorov because it is an immediate consequence of his studies [14-16] on the so-called "structure function" which has a 2/3 power law. The "-5/3 power law" was not explicitly written in Kolmogorov's first turbulence paper. It was found for the first time in Obukhov's paper [19], but this theory was actually independently discovered during the same period, by different famous scientists. Therefore, at the end of 1945 Heisenberg [20] and von Weizsacker [21] developed a closure theory of fully developed turbulence quite similar to that of Obukhov, which also leads to the "-5/3 power law" for the *psd*(k). Onsager arrived at the "-5/3 power law" by considering the energy cascade and

requesting, like Kolmogorov, the dependence only on the wavenumber and on the energy dissipation rate [22]. A detailed history of the discovery of the "-5/3 power law", can be found in the paper of Battimelli and Vulpiani [23].

The *tke* spectrum has an inertial sub-range also characterised by a $1/f^\alpha$ power law dependence. For the *tke* spectrum, the inertial range follows a "-2/3 power law" (see Appendix C). A further consequence of Kolmogorov's studies is that, for any given kind of turbulent flow, it is well known that this locally isotropic, inertial subrange should be broader in frequency or wavenumber as the Reynolds number increases [24].

Finally in the dissipation range, the small-scale eddies are affected by viscous forces, and it is there, ultimately, that turbulent energy is dissipated.

1.1.2   Large Eddy Simulation and Filtering Approach

The concept expressed by Kolmogorov [14-16] with reference to the statistical properties of the small scales, which at large Reynolds number are statistically isotropic and have structures which are statistically universal led to the invention of the Large Eddy Simulation (LES in the following).

The LES is a mathematical approach for turbulence modelling used in computational fluid dynamics, originally applied by Smagorinsky [25] in 1963. While in the Direct Numerical Simulation approach all the turbulent scales are resolved (the grid is finer than the finest turbulent eddy), in LES the aim is to resolve only the large energy-carrying scales, and to model instead the effect of the small scales of turbulence. Since the small scales tend to be more homogeneous and universal, their models can be simple and require fewer adjustments when applied to different flows than for the larger scales [26].

The partition of the scales in large resolved scales and the small non-resolved ones is formally achieved by applying a spatial filtering operator to the Conservation Equations. For a generic scalar field containing all the scales, the filtered variable that "captures" the resolvable-scale is the integral over the entire domain of the product between the scalar field and a function named "filter function" (or filter kernel), which depends on the spatial coordinates and on a length scale also defined as "filter width". This integrating operation to obtain the filtered variable is intended to be a low pass

filtering in the wavenumber domain, and allows us to decompose the generic scalar field as a sum of a function representing the resolved large-scale and a further function representing in LES the unresolved component that is obtained, instead, through the models [27-28].

For the small scales, different models, named sub-grid scales models, have been developed, usually imposing an eddy viscosity model to provide dissipation. The Smagorinsky model [25], the Dynamic Smagorinsky model [29-30] the Deardorff models [31] and the Vreman model [32] are some of the most used sub-grid scale models, to mention just a few.

Before proceeding we have to distinguish between two types of filtering in LES: the explicit and the implicit filtering.

In the explicit filters, the filter function is directly specified and can be of different kinds: gaussian, top-hat, sharp cutoff, to mention just a few (see [27] for a detailed description).

In the implicit filtering approach, the one originally used at the beginning of the LES approach [25-26], the filtering operation is not invoked. Instead, it is based on numerically solving the Navier-Stokes Equations with the available spatial resolution. Thus, the quantity of resolved scales and the quantity of modelled ones by the sub-grid scale model is assumed to be implicitly determined by several factors.

Firstly, in the implicit filtering the geometric mean of the filter dimensions Δ can be considered the filter width, because it directly affects the scale partition. Therefore, we can only resolve the wavenumbers up to the Nyquist wavenumber $k_c=\pi/\Delta$.

Secondly, the numerical method and their related truncation error, even if it cannot be considered as a filter, can affect the cutoff wavenumber and the trend of the spectra in the wavenumber domain.An implicit filter is always to be considered, also when applying an explicit filtering. Thus, the explicit filter is effective only if its width is larger than the grid dimension.
Figure 1.1 shows the comparison between the spectrum obtained with LES calculation that adopt an implicit filtering only (fine dashed line), the one obtained with an explicit filtering (blue solid line) and the "true" spectrum (black solid line), which can be calculated with t he DNS approach. The LES spectrum (fine dashed line) diminishes

more sharply than the "true" spectrum (black solid line), preceeding the grid cut-off wavenumber. The region named 'numerical error' is proportional to the missing energy that could have been in theory resolved with its grid. (Jameson and Bull [33]). The effect of the modelled sub-grid scales (the region marked as SGS) on the resolved scales is usually approximated by the above-mentioned sub-grid scale models. In general, a region of the spectrum characterized by an attenuation, where the influence of the implicit filtering occurs, can be identified. This "attenuated region" is bounded by two characteristic wavenumbers: the wavenumber where the trend of the spectrum deviates from the true spectrum and the wavenumber where the filter completes its action on the spectrum. In the spectrum obtained by explicit filtering (blue solid line), the energy in the resolved wavenumbers close to explicit filter wavenumber cutoff is closer to the true spectrum than in the one obtained with implicit filtering ([33]).
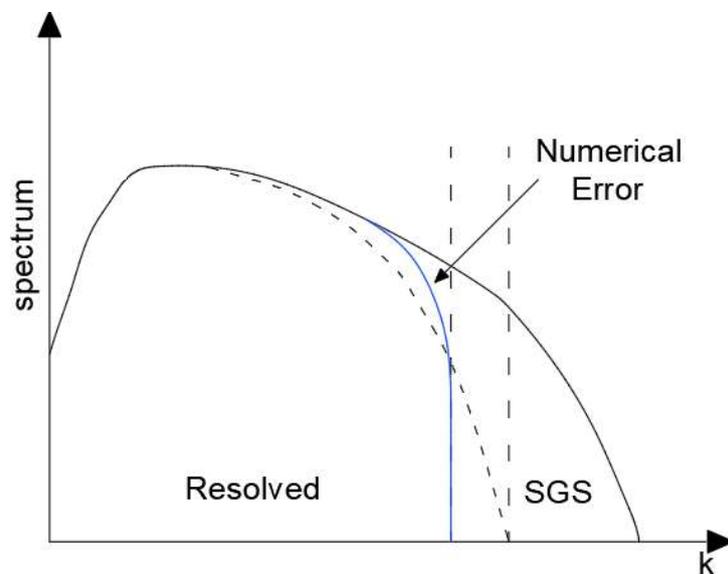
Figure 1.1: Exact DNS spectrum (solid black line), explicit filtering (solid blue line), implicit filtering (fine dashed line)

1.2   LITERATURE REVIEW AND STATE OF ART

An overview of the literature about the spectral analyses of the plumes and the ceiling jets is presented in Par 1.2.1. Despite its importance in Fire Safety engineering, the spectral analysis of the ceiling jet has received less attention by the researchers than that of the plumes. As explained in Par. 1.1.1 the spectral analysis involves the study of the frequency domain or the wavenumber domain. If the spectral analysis in the frequency domain simply involves the use of the Fourier Transform, in the wavenumber domain the methodology to obtain the spectra is more challenging. Thus, an overview of the available method to obtain the spectra in the wavenumber domain is presented in Par. 1.2.2 .

1.2.1   Spectral Analysis of Fire Plume and Ceiling Jet

In the past, the spectral analyses of the plumes have been widely discussed in the time and space domain. Ting and Hay [34] experimentally analysed, with an instrumented tower, the plume caused by the strong insulation on the terrain. Following the well-known Taylor's hypothesis (TH in the following) described in detail in Par. 1.2.1, the Authors studied PSDs of temperature and vertical velocity in the wavenumber domain. In more details, the TH was applied by using the mean wind velocity to relate frequencies and wavenumbers. The PSDs show a "- 5/3 power law" in accordance with the Kolmogorov theory.

Limiting the spectral analysis just to the frequency domain, other Authors studied the PSDs for the plumes. Papanicolaou and List [35] studied experimentally round vertical buoyant plumes by using optical techniques. PSDs were produced for vertical and longitudinal components of velocity fluctuations, separately. Dai et al. [36] carried out an experimental study of the structure of round buoyant turbulent plumes to analyse the PSD in the frequency domain of the mixture fraction fluctuations. The Authors observed that this PSD was in accordance with the "- 5/3 power law".

A considerable amount of literature about the plume concerns the application of the spectral analyses to the data obtained with numerical calculations. In particular, Zhou et

al. [37], Chung and Devaud [38], McGrattan et al. [39] performed numerical calculations, using CFD codes following a LES approach. These Authors [37-39] calculated the PSD in the frequency domain for the axial velocity fluctuations, identifying, in the inertial region, the "-5/3 power law" of the Kolmogorov decay. Rankin et al. [40], for a buoyant fire with and without an impingement, compared experimental measurements performed using the radiation intensity imaging technique, with numerical simulations produced with a LES approach. The agreement between measured and computed PSDs in the frequency domain was good. Fabregat et al. [41] numerically investigated, by using the Spectral Element Method, a deep-water oil blowout generated by a multiphase plume where the total inlet buoyancy flux was set by the combined presence of gas, oil, and heat. The PSD in the frequency domain limited to the axial velocity fluctuations in the flow direction shows the "- 5/3 power law" of the Kolmogorov decay. Cerminara et al. [42] developed a LES CFD code to study the PSD of temperature and pressure fluctuations in the frequency domain. Both the PSDs follow the expected decay with the "- 5/3 power law". Kumar and Verma [43] performed numerical simulations with a DNS approach to analyse a thermal buoyant plume in a cubic domain. They obtained the spectra in the wavenumber domain by invoking the TH. Their PSD follows a decay with the "- 5/3 power law".

If the spectral analyses of the plume flows have been widely discussed in the literature [35-43], only one reference [44] about the spectral analysis of a ceiling jet have been found. Husted [44] analysed a ceiling jet of a fire in a retail store, using FDS with different sub-grid models. In particular, the Author analyzed in one point the time domain obtaining a PSD in the frequency domain. The different cases showed a similar decay of the PSDs following the "- 5/3 power law".

To gather more information we also focused on flows having similar characteristics to the ceiling jet. In particular, we paid our attention to the jet impinging on a surface. Both the flows after the impingement on a surface deflect along the surface as shear flows. However, it has to be taken in account that in the jet impinging on a surface, the buoyancy forces can be totally absent. Shukla and Dewan [45] discussed the results of a LES calculation pertaining the flow and the thermal characteristics of a jet impingement. In

particular, they analysed the PSDs of the vertical velocity component at different locations in the wall jet region. The PSDs follow a decay with the "- 5/3 power law", but there are also spectra with different slopes. Different cutoff frequencies can be noted in the PSDs along the flows deflecting on the impingement. Grenson and Deniau [46] analysed using a LES code an impinging heated jet for a small nozzle-to-plate distance. In particular they [46] presented a PSD placed in the wall region away from the centre-line, following a decay with the "- 5/3 power law". Xu et al. [47] analysed with a LES code an impinging jet on a Semi-Cylinder Concave Target. In particular they analysed the PSDs of the radial velocity component at different locations far from the centre-line of the jet. The PSDs at the different locations follow the "- 5/3 power law", but with different frequency range extensions.

From our review of the literature [34-47], we can argue some considerations.

Most of the quoted literature [34-41] for the plumes discusses the spectral analyses in the time domain.

In the experimental investigations, the issue of avoiding a measurement apparatus with multiple devices able to simultaneously acquire the data, allows for an experimental set-up limited to the gathering of the data of velocity components in a single point or in a limited number of points.

For the plumes, in part of the literature reviewed [34,43], the PSDs in the wavenumber domain were analysed only by using the TH, which implies a linear correlation between frequencies and wavenumbers.

For the ceiling jet and the flows having similar features, in the reviewed literature [45-47], the PSDs generally follow the "- 5/3 power law". In particular, for the flows having features similar to the ceiling jet, moving away from the centre-line of the jet, the PSDs change in terms of extension of the inertial sub-range. Furthermore, using the LES codes, the cutoff frequency changes, moving away from the jet impingement centre-line.

1.2.2 Spectra in the Wavenumbers Calculation Technique

In the wavenumber domain, the main method for the calculation of the spectra is the direct one, (see for instance Tennekes and Lumley [10]), which goes through "the spatial

correlation function" at a certain instant between the fluctuating velocity components in a point and in the surrounding points. A use of particular interest of the direct method was discussed by McMahan et al. [48] for a river. They analysed a two points and two times correlation function, and its Fourier transforms in time and space obtaining the so-called frequency-wavenumber spectrum. Regrettably, we did not find papers using this direct method for plumes. In the application of the direct method, a difficulty stems from the necessity of data in a large number of points closely spaced. This issue has consequences not only in the experiments where a lot of probes need to be involved simultaneously, but also in the numerical calculations, where refining the grid to have more available data points increases the amount of resources in terms of computational efforts and has implications on the geometry of the domain. In turbulence calculation the lower computational effort allowing to obtain a PSD is the LES. However, this approach focuses on two main concepts: resolving an adequate portion of the spectrum and limiting the number of nodes to save computing effort. Thus, the difficulty due to the necessity of data in a large number of closely spaced points is not overcome even with the use of LES. Therefore, a limited number of points where the data are available affects the resolution of the PSD in the wavenumber domain. Regrettably, we did not find papers using the direct method for plumes.

As an alternative to the direct method, for the plumes, in part of the reviewed literature [34, 43], the PSDs in the wavenumber domain were obtained only by using the Taylor's hypothesis, relating the spatial and temporal characteristics of turbulence. Taylor [13] theorized that if the root mean square of the fluctuating velocity is small compared to the time-averaged flow velocity U and the turbulence is homogeneous, then the temporal response at a fixed point in space can be viewed as the result of an unchanging spatial pattern, also named frozen turbulence, advecting turbulence uniformly past the point at the time-averaged flow velocity. This assumption implies a linear transformation between time and space, $x = Ut$. Thence, it is possible to express the wavenumber k as a function of the frequency f, using the relationship $k=2\pi f/U$. Thus, if a PSD in the frequency domain shows the "- 5/3 power law", the use of the TH implies that this feature is observed also in the wavenumber domain. To conclude our considerations, outside the

applicability limits of the TH, when a linear correlation between frequency and wavenumber is not acceptable, as often happens in fire related flows, and when it is not possible to directly produce with sufficient accuracy the PSD in the wavenumber domain, other approaches are needed.

Beside the TH, to analyse the spectra in the wavenumber domain as alternative to the direct method, different model-based approaches were proposed in literature:

- different corrections to TH,
- the random sweeping model,
- the elliptic approximation.

These approaches are based on the search for correlations between frequencies and wavenumbers.

TH has been an invaluable method of correlation since Taylor's proposal in 1938 (Taylor [13]). An example of this approach is the analysis of the PSD in the wavenumber domain in a tidal channel, performed by Grant et al. [49], using a velocity measuring probe towed by a ship moving at the mean flow velocity. TH was used, and it is still used, in many applications, significantly economizing the efforts in calculating the PSDs in the wavenumber domain. If a PSD in the frequency domain shows the "- 5/3 power law", the use of the TH ensures that this feature is observed also in the wavenumber domain. Lin [50] has shown that TH is applicable only if the turbulence level is low, viscous forces are negligible, and the mean shear is small. This research [50] suggests that a possible application of the TH to a fire plume can be difficult due to the highly turbulent flows generated by fires (Westenberg and Rice [51]). Lin also argued that there is no general justification of extending TH to the case of shear flow. This suggests that also the application of the TH to a ceiling jet, which is a typical shear flow, can be critical.

Although in only a few cases of turbulent plumes or ceiling jets the PSD of the fluctuating velocity in the wavenumber domain was investigated with the TH, it was widely used in other configurations, such as grid generated turbulence, turbulent jets or shear flows. One of the first applications of the TH can be associated with the grid generated 'isotropic' turbulence. Among these applications, we can mention Comte-Bellot and Corrsin [52] and Kistler and Vrebalovich [53] for grid generated turbulence in

ducts, and Favre et al. [54] for a grid placed upstream a boundary layer. For a turbulent jet, Champagne [55] analysed, experimentally, the PSDs of the fluctuating velocity components by applying the TH using the mean stream-wise velocity. For a nearly homogeneous turbulent shear flow, Champagne et al. [56] analysed experimentally the PSD of the velocity fluctuations in the wavenumber domain, by applying TH. Extensive studies that assess the reliability of the TH, are reported in the literature. Among these Zaman and Hussein [57] and Mi and Antonia [58] can be mentioned. For a turbulent shear flow in a duct, Zaman and Hussein [57] found experimentally that using the local time-averaged velocity produces unacceptable distortions in the spatial distributions of the vortical structures. For an experimental analysis on a turbulent circular jet, Mi and Antonia, concluded that the usual form of TH applies only near the jet axis [58].

The unpleasant effects of the TH suggested the introduction of corrections to the TH. In particular, for high turbulence intensity shear flows Lumley [59] proposed to correct the high wavenumber range of the one-dimensional spectra and subsequently Hill [60] and Gledzer [61] extended Lumley's correction ideas to other flows. Heskestad [62] proposed a correction to TH, doing an order of magnitude estimate of the terms in the streamwise momentum equation, for his case of high turbulent free shear flow. More recently Buchhave and Velte [63] proposed a correction to the TH for highly turbulent flows. Another correction to the TH was made by Wills [64]. The Author [64] introduced an effective velocity useful to correlate frequencies and wavenumbers. To the aim, he analysed the two points two times correlation function between the fluctuating velocity components in a point and in the surroundings points and between an instant and the other instants. The two points are separated by a "separating vector" and the instants are separated by a "time shift". He defined the "convection" velocity as the ratio between "separating vector" and "time shift" which maximises the covariance of the fluctuating velocity components between two points and two instants. This convection velocity allows to obtain the spectra in the wavenumber domain by correlating frequency and wavenumber similarly to the TH. This Wills' definition arised from the experience of Willmarth and Wooldridge [65] that presented a space-time correlation graph of the velocity components of a turbulent boundary layer produced on a smooth surface. When

the TH is invoked, it is implied that the iso-contours of a space-time correlation graph are straight lines. Wills noticed, instead, that the covariance contours in this graph behave differently from the TH assumptions. Furthermore Wills noted that when the turbulence intensity is high, the convection velocity may differ considerably from the mean velocity, while it is shown that different turbulent spectral components appear to travel at different speeds. Fisher and Davies [66] noted that large departures of the convection velocity from the local time-averaged velocity can be due to the skewness of the probability distribution of the velocity fluctuations. Furthermore, they noted that the turbulent structures at the lower wavenumbers move slower than at the higher wavenumbers.

Further definitions of the convection velocity have been provided by different researchers. Bradshaw et al. [67] defined the convection velocity as "the rate that minimizes the change of the maximum correlation with respect to time only". Davies et al. [68] defined the convection velocity as "the rates at which change of correlation in space and time are equal". Finally, Favre et al. [69] defined the convection velocity as the geometric mean of two convection velocities, the one defined by Wills [64] and the other defined by Davies et al. [68].

Goldschmidt et al. [70] experimentally analysed the convection velocity on a plane jet issued from a rectangular slit. The Authors state that quantitatively the convection velocity defined by Wills [64], Bradshaw [67] and Davies [68] are not very different. The Authors [70] refer to the convection velocity as the phase velocity and studied the relation with the local time-averaged velocity. These results of Goldschmidt et al. [67] confirmed the ones of Fisher and Davies [66]. Furthermore, their results indicate that the ratio of the convection velocity to the local time-averaged velocity is greater than unity, for high wavenumbers.

A literature review of the limitation of the TH and of the corrections proposed has been discussed by Geng et al. [71] and by Wallace [72].

To relate frequency and wavenumber domains, Kraichnan [73] and Tennekes [74] used the so-called "random sweeping hypothesis", which assumes that the small-scale fluctuations in a turbulent flow are swept by the large-scale eddies in a random manner. Wilczek and Narita [75] introduced a model to calculate the frequency-wavenumber

spectrum based on the random sweeping hypothesis [73]. This is the "random sweeping model" and is based on the concept that the statistical nature of the sweeping velocity is Gaussian and that it is assumed to be not a function of frequencies and wavenumbers. The resulting diagram that correlates frequencies and wavenumbers is a contour plot where the iso-correlation contour distribution shows the presence of a Doppler effect. As shown by Narita [76], the mean flow causes a Doppler shift, while the variation of the large-scale flow causes Doppler broadening around the Doppler shifted frequency. This method was applied by Narita [77] for the plasma turbulence and by Wilczek et al. [78] for atmospheric boundary layers.

Always following the concept of the random sweeping hypothesis [73-74], He and Zhang [79] and Zhao and He [80] developed the so-called elliptic model. Based on this approximation, in contrast to the TH, the elliptic model allows to relate frequencies and wavenumbers, using the elliptic curve obtained by combining the local mean and the random sweeping velocities, the latter is defined by Kraichnan [73] as the root mean square of the fluctuating velocity.

The identification of a correlation between frequencies and wavenumbers is a critical task also in other fields, in particular, in the structural modal analysis and in acoustics. Within this framework, different approaches were developed based on the behaviour of the wave propagation in the media. The oldest approach, developed in the 18th century, is Prony's method (Marple [81]), later modified and extended for structural vibrations by Grosh and Williams [82], that allows to identify the dispersion relation using an exponential model of the spatial response. McDaniel and Shepard [83] developed a method that allows to identify numerically and iteratively a correlation between frequencies and wavenumbers. One of the novelties of the method consists in avoiding any physical model. Berthaut et al. [84] generalized the method, named now Inhomogeneous Wave Correlation method (IWC method in the following) because it consists in the comparison of the signals of a wavefield with an inhomogeneous wave in the space domain. IWC method, starting from the spectra in the frequency domain, allows to obtain the so-called dispersion curve i.e., the correlation between frequencies and wavenumbers. With the IWC method a comparison between the PSDs in the frequency

domain and the inhomogeneous wave cannot be done, but instead the Fourier Transform of a signal should be used, as it will be explained in Par. 2.3. The IWC method is now consolidated and has been widely used in the structural and vibro-acoustic field by many Authors. For instance Van Damme and Zemp [85] and Santoni et al. [86] applied the IWC method along a unidimensional straight line, whereas Ichchou et al. [87],Cherif et al. [88], Tufano [89] Tufano et al. [90] applied the IWC method in bidimensional coordinates.

1.3   SCOPE OF THE THESIS

For a test case concerning a turbulent reacting plume and the following ceiling jet, the *tke* is analysed both in frequencies and wavenumbers with a correlation between these parameters identified by using the IWC method.

The aim is to gather and discuss all the information to gain an insight into the physics of the time and length scales of the two flows, with regard to the characteristics of the numerical code, its turbulence solver approach and the choice of the grid. To this aim, the spectral analysis of the *tke* is discussed in both the frequency and wavenumber domains. If the spectral analysis in the frequency domain simply involves the use of the Fourier Transform, in the wavenumber domain the methodology to obtain the spectra is more challenging due to some limitations in the use the direct method or in the TH for the fire related flows: inhomogeneous turbulence, high turbulence intensity and lack of a large number of points closely spaced. However the information provided by the *tke* spectrum in the wavenumber domain is fundamental for two main reasons:

- to elucidate of the nature and distribution of spatial scales in such turbulent flows,
- to have direct information about the filtering, which in FDS is implicitly imposed in space by the grid.

With *tke* spectrum in the wavenumber domain this information is achieved straightforwardly, whereas in the frequency domain the knowledge of the phase velocity

is needed.

We opted for the IWC method, which looks for the frequency/wavenumber correlation avoiding physical models.

To the best of our knowledge, an extension of the IWC method to turbulence has not yet been attempted.

For the fire plume and its ceiling jet, special care, in the spectral analyses of the frequency and wavenumber domain is given to assess:

- the influence of the implicit filtering used in FDS on the *tke* spectra,

- the study of practical rules to predict the influence of the implicit filtering on the *tke* spectra,

- the quality of the grid,

- the scaling law in the inertial subrange, verifying whether it follows the Kolmogorov theory,

- the quantity of time-averaged resolved *tke* and the modelled one,

- the difference about the turbulence dissipation behaviour between the fire plume and the following ceiling jet,

- the phase and group velocity of the *tke* along the centre-line plume and along the ceiling jet radius.

Chapter 2

NUMERICAL CALCULATION AND
THE IWC METHOD

2.1 CASE STUDY

A turbulent ceiling fire is investigated in the cubic domain (10 m x 10 m x 10 m) shown in Figure 2.1. A square burner (1.5 m x 1.5 m) is in the centre of the bottom plane on a support 0.5 m heigh. Coordinates are given in a cartesian reference system shown in Figure 2.1, with the origin in the centre of the bottom plane of the domain.

Propane, released with a flow rate such as to achieve an imposed heat release rate (HRR), is used for the fire. HRR reaches, with a linear growth, a maximum value of 5 MW after 10 s (Figure 2.2), and remains constant until 100 s, the end of the simulation.

The domain has a box shape with top and bottom solid surfaces. The lateral faces are free to communicate with the external ambient.

The problem is numerically studied with FDS (release 6.7.1). No slip condition is assigned to the bottom and the top walls. The remaining faces are modelled as open boundaries where the fluid is allowed to flow into or out. On these faces the boundary conditions on the total pressure are assumed. The far field wind velocity is null. A sensitivity analysis with respect to the domain dimensions is performed to ensure that moving away the open boundary, enlarging the domain, not appreciable results in our spectral analysis can be revealed.

Concerning the heat transfer, to the solid top and bottom wall a temperature of 20 °C is assigned. The same boundary condition is assigned for the lateral walls of the burner as well. The far field air temperature is 20 °C. For the thermal radiation, the open boundaries are treated as black walls, where the incoming radiation intensity is the

blackbody intensity of the far field air temperature.

The time step used is 10^{-3} s, which was chosen to be regular and fine enough that the time stability constraint is always satisfied (see Par. 2.2 for detail about the code).

2.1.1   Choice of the Mesh

FDS allows the use of only structured rectilinear grids. The analysis was started by choosing grids using the rule of thumb proposed in the FDS User Guide [91] and in the report NUREG 1284 [92], in which the ratio between the fire diameter, D*, and the cell size has to be chosen between 4 and 16. The fire diameter is calculated as:

$$D^* = \left(\frac{\dot{Q}}{\rho_\infty c_p T_\infty \sqrt{g}} \right)^{2/5} \qquad (2.1)$$

where $\dot{Q}$ is the maximum heat release rate, c_p is the specific heat at constant pressure, g is the modulus of the gravity acceleration, ρ_∞ and T_∞ are the far field air density and temperature, respectively. In this case study, D* is 1.83 m. Two ratios in the suggested range are chosen: 7 and 15 corresponding to the grid sizes: 0.25 m and 0.125 m, respectively. An additional grid size of 0.0625 m with a ratio of 30, outside the suggested range, is used. The total number of nodes for the three different grids are: $64 \cdot 10^3$ nodes, $512 \cdot 10^3$ nodes, $4096 \cdot 10^3$, respectively. In the following we refer to the grids 0.25 m, 0.125 m and 0.0625 m using the acronyms CG, MG, FG respectively, which stands for Coarse Grid, Medium Grid and Fine Grid.

Finally the dimensionless heat release rate (Q* in the following)

$$Q^* = \frac{\dot{Q}}{\rho_\infty c_p T_\infty \sqrt{gD} D^2} \qquad (2.2)$$

should be inside the range $0.3 \leq Q^* \leq 2.5$, suggested by Cox and Kumar [93] for natural fires in buildings. For our case study a value Q* = 1.2 arises, which is inside the range.
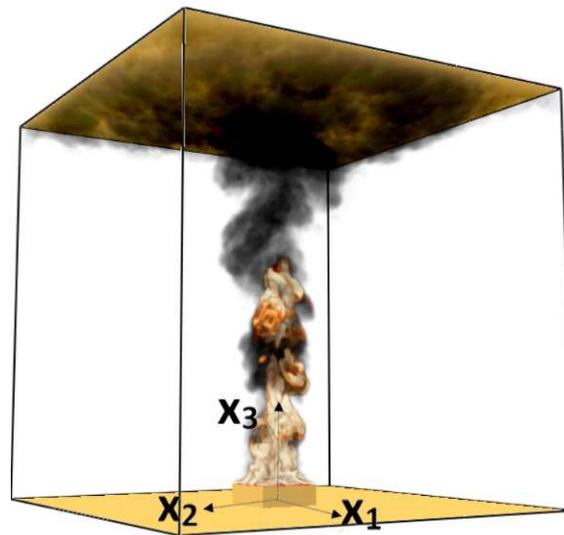
Figure 2.1: Computational domain.
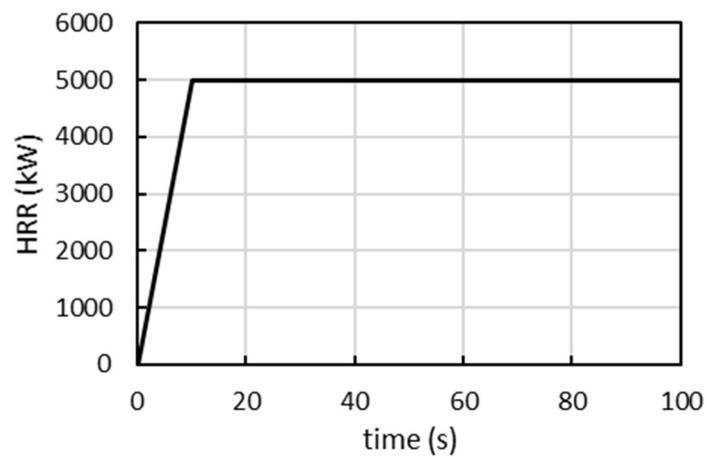
Figure 2.2: HRR curve imposed to the burner.

2.2 METHODOLOGY

2.2.1 Description of the Numerical Model

As stated in the FDS User Guide [94] the solver algorithm of FDS is second order accurate in space and time. A time stability constraint has to be always satisfied. The flow

solver is based on the finite difference method, whereas the scalars (combustion, soot, etc…) are managed with the finite volume method. Turbulence is resolved with a LES approach. Different sub-grid turbulent models are available. In these calculations we used "Deardorff" with a turbulent eddy viscosity given as function of the geometric mean of the cell dimensions, Δ, and the subgrid turbulent kinetic energy, tke_{sgs} [94]. In the implicit filtering approach used by FDS, the grid is the only filter. As a consequence of the Nyquist Theorem, no scales finer than 2Δ can be captured in the numerical calculation. The cutoff wavenumber associated to 2Δ is assumed as the Deardorff limit π/Δ. The subgrid kinetic energy is then approximated by integrating the Kolmogorov spectrum from the cutoff wavenumber, π/Δ, to infinity.

The details of the numerical methods adopted by the FDS code are fully described in the FDS Technical Guide [95] (discretization, pressure-velocity coupling, spatial interpolation of advection terms, time stepping algorithm, subgrid model).

FDS treats combustion chemistry using a simplified approach. Only fuel, air, and products are tracked and we refer to each one of them as "lumped species". A lumped species consists of a mixture of gas species (defined "primitive species" in the following) that transport together and react together. Concerning the numerical model, a lumped species can be treated as a single species. The mass transport equations make no distinction between single or lumped species. For example, air is a lumped species that consists of nitrogen, oxygen, and traces of water vapor and carbon dioxide. The lumped species mass fractions of air fuel and products, are linearly related to the primitive species mass fractions. Thus, the conversion from one to the other can be performed with a matrix multiplication. The products are defined stoichiometrically, usually including prescribed yields of soot (for smoke) and carbon monoxide that can be obtained from empirical relationships for each specific fuel.

Using the LES approach for the numerical calculations of fire related flows implies the issue that the "length and the timescales associated with the chemical reactions may be orders of magnitude below what can be spatially and temporally resolved by the simulation"[95]. It is thence important to consider the behaviour of a sub grid scale model as the LES filter width (cell size) varies. To this end, as explained by McDermott et al.[96],

FDS uses a simple mixing environment method that includes the Eddy Dissipation Concept (EDC) model of Magnussen and Hjertager [97-98]. In particular, depending on the filter width, the reaction time scale varies with different rates in their specific ranges (see McDermott et al.[96]).

Examples of past applications of FDS to fire simulations are provided by the FDS Validation Guide [95] where the results of a large number of numerical calculations are presented and compared with experimental data for validation purposes.

2.2.2 IWC Method

The spectral analysis performed in this thesis involves the discussion of the *tke* spectra in the frequency and wavenumber domains. As discussed in Par. 1.3, if the spectral analysis in the frequency domain simply involves the use of the Fourier Transform, in the wavenumber domain it is more challenging due to some limitations in the use the direct method or in the TH for the fire related flows: inhomogeneous turbulence, high turbulence intensity and lack of a large number of points closely spaced. For our test case, we want to produce the *tke* spectrum in the wavenumber domain, by avoiding using the spatial correlation or the TH. To this aim, we use the IWC method (Berthaut et al. [84]) that allows to correlate frequencies and wavenumbers with the 'correlation-law'. Unlike the methods described in Par. 1.2.2 [64-69] that look for the convection (phase) velocity by analysing the two-point two-time correlation function, the IWC method allows to produce directly a correlation law between frequencies and wavenumbers. Furthermore, unlike other phenomenological approaches that make ad hoc assumption, such as TH that treat the local mean as the convection velocity and the Kraichnan approach [73] or the elliptical model [79-80] that uses also the sweeping velocity to assess the dependence between frequencies and wavenumbers, the IWC method does not use any model.

A further characteristic feature of the IWC method, typically used in the structural and vibro-acoustic field, is the estimation of the damping in the structures. This feature will be applied to estimate the dissipation characteristics for the plume and its ceiling jet.

The application of the IWC method requires a signal variable in frequency and space, $W(f,\overline{x})$. When a signal variable in time and space, $w(t,\overline{x})$, is available, the

signal in the frequency domain, $W(f,\overline{x})$, is obtained with the Fourier transform:

$$W(f,\overline{x})=\int w(t,\overline{x})e^{i\,(2\pi\,f\,t)}dt \qquad (2.1)$$

The IWC method compares $W(f,\overline{x})$ to an inhomogeneous wave, travelling along a specified path. The inhomogeneous wave can decay in one or more directions because of damping components. It can be plane, cylindrical, or spherical:

$$\sigma(f,\ \overline{x})=\frac{e^{i(2\pi\,f\,t_0)}e^{i\,(-\overline{k}_p\cdot\overline{x})}\ e^{(\overline{k}_d\cdot\overline{x})}}{|\overline{r}|^n} \qquad (2.2)$$

where $\overline{k}_p$ is the propagative wavenumber vector, $\overline{k}_d$ is the dissipative wavenumber vector, t_0 is an instant, $\overline{r}$ is the pointing vector centred in the source of the signal, n is 0 for the plane wave, 1/2 for the cylindrical and 1 for the spherical one.
If we introduce:

$$\sigma_0(f)=e^{i(2\pi\,f\,t_0)} \qquad (2.3)$$

Equation (2.2) can be rewritten:

$$\sigma(f,\overline{x})=\frac{\sigma_0(f)\ e^{i\,(-\overline{k}_p\cdot\overline{x})}\ e^{(\overline{k}_d\cdot\overline{x})}}{|\overline{r}|^n} \qquad (2.4)$$

A detailed derivation of the inhomogeneous wave is addressed by the Appendix D.

The IWC method is based on the comparison of the signal wave-field with the inhomogeneous wave in the space domain. Therefore, the method considers the inhomogeneous wave as the theoretical model of propagation of the signal and quantifies the adherence of the original signals to the theoretical model. The comparison is performed by calculating an indicator able to assess the degree of consistency between the signal $W(f,\overline{x})$, at a specified frequency, and the inhomogeneous wave $\sigma(f,\ \overline{x})$. This indicator is the square root of the Modal Assurance Criterion (Ewins [100]), which is defined as the Hermitian inner product of signal and inhomogeneous wave (Vacher et al. [101]). The indicator is specified as:

$$IWC(f,\overline{k}_p,\overline{k}_d) = \frac{\left| \int_{\ell} \sigma^*(f,\overline{x})\,W(f,\overline{x})\,d\overline{x} \right|}{\sqrt{\int_{\ell} \left| \sigma(f,\overline{x}) \right|^2 d\overline{x} \int_{\ell} \left| W(f,\overline{x}) \right|^2 d\overline{x}}} \qquad (2.5)$$

where * denotes the complex conjugate and ι is here the line integral. For the application of the IWC method, the line where the signal is available is named "propagation line" and its origin, in terms of coordinate reference system, coincides with the lower extreme of the line integral. This Method is applied by assigning a specified frequency and performing the calculation of the IWC parameter for every combination of propagative and dissipative wavenumbers associated to the specified frequency f. Thus, the combination of $\overline{k}_p$ and $\overline{k}_d$ associated to the specified frequency f is the one that maximizes the parameter $IWC(f,\overline{k}_p,\overline{k}_d)$. This means that the signal of the wave-field at the specified frequency f and the inhomogeneous wave at the identified propagative and dissipative wavenumbers shows the highest adherence. This procedure allows us to identify the correspondence between a frequency and the combination of propagative and dissipative stream-wise wavenumbers, at which the IWC of Eq. (2.5) parameter is the maximum. Two datasets, one that relates $\overline{k}_p$ with f and the other relating $\overline{k}_d$ with f, allow us to obtain the propagative and dissipative dispersion graphs, respectively.

The theory of the IWC method described in this paragraph, involves continuous signals in space and time. Nevertheless, usually, for both the experimental and the numerical fields, the signals are distributed in a finite number of data points and time steps. Thus, the application of the method needs to follow a numerical approach.

In Par. 2.3 the IWC will be studied for our turbulence problem and specified for the plume and its ceiling jet.

2.3   APPLICATION OF THE IWC METHOD

As discussed in the Introduction, plumes and ceiling jets differ evidently in the flow

patterns. The plume is a typical boundary free shear flow, whereas the ceiling jet can be classified as a wall bounded shear flow. Furthermore, as it will be clear in the discussion of the results (Chapter 3), the two flows differ also in their turbulent behaviour. The plume shows a typical propagative behaviour due to the large production of momentum from the buoyancy forces. Differently, the ceiling jet, where the momentum is not produced but comes from the flow of the plume, shows a dissipative behaviour. For this reason, the plume and the ceiling jet deserved two different approaches.

Whereas, in Par. 2.2 the IWC method was exemplified for continuous signals, in this Paragraph it is applied to the results of our numerical calculations. The signals are, therefore, discrete in time and space. Thus, instead of the parameters $\overline{x}$, t and f, in the following $\overline{x}_m$, t_k and f_j will be used. The subscripts emphasize that the variables are discrete. The velocity components are then $\tilde{u}_i\left(\overline{x}_m, t_k\right)$.

We use the Reynolds' decomposition to separate the fluctuating component of velocity. We always verify that, in the considered time interval, the mean of the fluctuating velocity components is null. The time-averaged value of the velocity components is also analysed. In our cases, considering a time interval $20 \text{ s} \leq t_k \leq 100 \text{ s}$, starting 10 s after the end of the growth phase of the HRR (Fig 2.2), the turbulence was suitable for the application of the IWC method

2.3.1   The IWC method for the fire plume

For the plume, we used the IWC method to analyse the *tke* spectra in the wavenumber domain. It is applied to evaluate, along a straight propagation line, the degree of coherence between the *tke* spectra and the inhomogeneous waves. The fire plume has a truncated cone pattern, with an aperture angle of about 10° (Turner [102]). As shown in Fig. 2.3 this aperture is so small that the pattern tends to a cylinder. This suggests that the front of propagation of the fire plume is a plane, so the inhomogeneous wave to be considered is also plane. The IWC method is applied along the vertical centreline of the domain. The properties of this path are: it is rectilinear, it follows the direction of propagation, and, along this line of propagation the nodes of the computational domain are equally

separated. The results are used, starting from 1 m of height (0.5 m of height from the burner) up to 0.5 m from the upper limit of the domain. Unlike what is shown in Fig. 2.1, in the application of the IWC method for the fire plume, the origin of the coordinate of the reference system is in the vertical centreline of the domain at 1 m of height, at the starting point of the analysis.

The application of the method starts with the calculation of the values of $TKE(\overline{x}_m, f_j)$ with a discrete Fourier transform (DFT) using a FFT algorithm:

$$TKE(\overline{x}_m, f_j) = FFT(tke(\overline{x}_m, t_k))$$
(2.6)

where $tke(\overline{x}_m, t_k)$ was calculated in every node $\overline{x}_m$ as shown in Eq. (B.1).

Once the values of $TKE(\overline{x}_m, f_j)$ are calculated, the IWC method begins allowing us to explore the wavenumber domain. As shown in Eq. (2.2), the scalar product between wavenumber vectors ($\overline{k}_p$ and $\overline{k}_d$), and $\overline{x}$ is done. Along the centreline of the fire plume, the vector $\overline{x}$ reduces to $\overline{x}_m = (0,0, x_{3,m})$. Thus, the inhomogeneous wave of Eq. (2.2) reduces to:

$$\sigma(x_{3,m}, f_j) = \sigma_0(f_j)e^{i(-k_{3,p}\, x_{3,m})}e^{(k_{3,d}\, x_{3,m})}$$
(2.7)
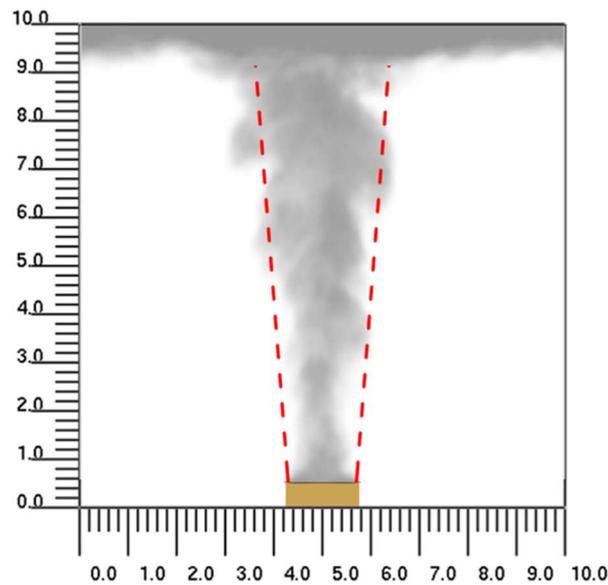
Figure 2.3: Plume and its truncated cone pattern propagation highlighted in red

The IWC method is implemented on Matlab using three nested cycles, calculating the IWC parameter:

$$IWC(f_j,k_{3,p},k_{3,d})=\frac{\left|\sum_{m=1}^{N}\sigma_0(f_j)e^{i(-k_{3,p}\ x_{3,m})}e^{(k_{3,d}\ x_{3,m})}\cdot TKE(f_j,x_m)\right|}{\sqrt{\sum_{m=1}^{N}\left|\sigma_0(f_j)e^{i(-k_{3,p}\ x_{3,m})}e^{(k_{3,d}\ x_{3,m})}\right|^2\sum_{m=1}^{N}\left|TKE(f_j,x_m)\right|^2}}$$ (2.8)

where N is the number of centroids along the centreline.

The external cycle allows us to select progressively, at each step, a frequency f_j, using the step size frequency of the array created for the FFT. The middle nested cycle allows us to select, for every loop of the external cycle, the propagative stream-wise wavenumber, using a step-size of 0.1 m^{-1} for $k_{3,p}$. The inner cycle allows us to select, for every loop of the external and medium cycle, the dissipative stream-wise wavenumber, using a step-size of 0.01 m^{-1} for $k_{3,d}$. The step-size of $k_{3,p}$ and $k_{3,d}$ was chosen by progressively refining them until appreciable differences could not be find. This procedure allows us to obtain every combination of f, $k_{3,p}$ and $k_{3,d}$. In every loop of the inner nested cycle, for every combination of frequency propagative and dissipative stream-wise wavenumbers, the IWC parameter is calculated with Eq. (2.8).

Now it is possible to identify the stream-wise wavenumber (both the dissipative and the propagative ones), corresponding to the maximum of the IWC parameter between the ones calculated in the outer nested cycle. Two datasets, one that relates $k_{3,p}$ with f and the other relating $k_{3,d}$ with f, allow us to obtain the propagative and dissipative dispersion graphs, respectively. The propagative dispersion graph has f in abscissa and $k_{3,p}$ in ordinate, while the dissipative dispersion graph has f in abscissa and $k_{3,d}$ in ordinate.

The equation that fits the frequency-streamwise propagative wavenumber datasets of the propagative dispersion graph is the correlation-law. Now, it is possible to switch from the frequency domain to the wavenumber domain, and to obtain the *tke* spectra in the wavenumber domain in every point along the propagation line.

Furthermore, important information about the attenuation caused by the medium can be obtained with the dissipative dispersion graph.

2.3.2 The IWC Method for the ceiling jet

The ceiling jet spreads radially from the turning zone. The propagation pattern of the stratified combustion products has the shape of a radially expanding hollow disk. The propagation line, where the IWC method is applied, should be chosen along a radius of this radially expanding hollow disk, the turning zone avoided. With reference to the geometry of the ceiling jet, the propagation line begins from 1 m of distance from the centre and stops at the external boundary. It is placed at a distance of 0.25 m from the ceiling, inside the smoke layer, with the origin of the coordinates of the reference system in the centre of the plane. For a more representative analysis four radii were considered, in two perpendicular directions, where the data points are aligned and equally spaced. The time histories of the fluctuating velocity component $u_i\left(\overline{x}_m, t_k\right)$ of the nodes that, for each radius, have the same distance from the centre, are placed in series to obtain a single radius that can be considered representative of the four radii. It is checked that the concatenated histories of the fluctuating velocity component $u_i\left(\overline{x}_m, t_k\right)$ are random by ensuring that the results of the IWC method remain the same by changing the order on which the histories of the velocity component are placed in series. Using these concatenated velocity components, the $TKE(\overline{x}_m, f_j)$ is calculated.

In applying the IWC method, the choice of the appropriate type of inhomogeneous wave is considered. Thus, the flows spreading radially from the centre of the domain can suggest that the appropriate inhomogeneous wave to be compared with the wave-field is the cylindrical one instead of the mainly used [86-90] plane inhomogeneous wave. Both the cylindrical and plane inhomogeneous waves have been used to assess whether this choice can bring appreciable differences.

The wavenumber vectors $\overline{k}_p$ and $\overline{k}_d$, as shown in Eq. (2.4), are projected on $\overline{x}_m = (x_{L,m}, 0, 0)$ (where the L subscript stands for longitudinal, which is in the direction along the radius). Thus, the inhomogeneous wave of Eq. (2.4) reduces to:

$$\sigma(x_{L,m}, f_j) = \frac{\sigma_0 \; e^{i\,(-k_{L,p}\,x_{L,m})} \; e^{(k_{L,d}\,x_{L,m})}}{|\overline{r}|^n} \tag{2.9}$$

where n is 0 when the plane wave is adopted, and ½, when the cylindrical wave is adopted.

The difference between the plane wave and the cylindrical wave can be clearly seen if we look at the homogeneous wave (the inhomogeneous wave where the dissipative wavenumber is zero, see Appendix D for detail). As shown in Figure D.2, the cylindrical wave has an attenuation derived by the geometry of its wave-front that is not present in the plane one of Fig. D.1.

The same algorithm explained for the plume is applied, but Eq. (2.5) is numerically calculated for every frequency f_j by using:

$$IWC(f_j,k_{L,p},k_{L,d})=\frac{\left|\sum_{m=1}^{N}\frac{\sigma_0 e^{i(-k_{L,p}x_{L,m})}e^{(k_{L,d}x_{L,m})}}{|\overline{r}^n|}\cdot TKE(f_j,x_{L,m})\right|}{\sqrt{\sum_{m=1}^{N}\left|\frac{\sigma_0 e^{i(-k_{L,p}x_{L,m})}e^{(k_{L,d}x_{L,m})}}{|\overline{r}^n|}\right|^2 \sum_{m=1}^{N}\left|TKE(f_j,x_{L,m})\right|^2}} \quad (2.10)$$

The algorithm already explained for the plume is used for the ceiling jet to calculate the dispersion graphs.

The correlation-law between the frequency and the stream-wise wavenumber domains is the fitting on the dispersion graph. The *tke* spectrum in the wavenumber domain is calculated by using the correlation-law. Furthermore, the identified correlation between the frequencies and the dissipative wavenumbers can suggest important information about the attenuation that is taking place in the flow.

Chapter 3

RESULTS

As mentioned in the Par. 1.3 "Scope of the thesis", we seek to gain an insight into the physics of the time and length scales of our plume and its ceiling jet with regard to the characteristics of the numerical code, its turbulence solver approach and the choice of the grid.

As the first step, in Par. 3.1 "Preliminary Analysis" we focus on the scales of the fire plume and its ceiling jet. This step involves not only the discussion of the most significant length scales, but also the comparison between the scales assessed through the use of the numerical calculations and the ones obtained with analytical solutions. A particular scale considered is the turbulence intensity that plays an important role in assessing the applicability of the TH.

Secondly, the attention is focused, for both the plume in Par. 3.2 and its ceiling jet in Par. 3.3, on the spectral analysis. In both Par. 3.2 and 3.3 we discuss the *tke* spectra in the frequency domain. In particular, we assess the features of the inertial sub-range: its power law, extension and attenuation. The analysis of the cutoffs allows to gain information not only about the flows but also about the numerical code. We use this information to develop practical rules and we verify whether they are able to predict these cutoffs. For the plume we use the spectral analysis also to assess the quality of the numerical calculation with the different grids. In particular the time-averaged resolved *tke* and the modelled one are discussed. Subsequently, the results of the IWC method are shown: the dissipative and the propagative dispersion graphs. A discussion about the fitting function applied to the propagative dispersion graph to obtain the correlation-law is done. Furthermore, through the correlation-law it is possible to obtain the group velocity and the phase velocities. Through the dissipative dispersion graph, differently from the propagative one, we can have an insight on the attenuation of the turbulence intensity due to the medium.

Finally, once the correlation-law is found, we apply it to the *tke* spectra in the frequency domain to obtain the *tke* spectra in the wavenumber domain along the propagation lines. As for the *tke* spectra in the frequency domain, also in the wavenumber domain special care has been given to the identification of the cut-off frequencies, evaluating whether they are predictable with practical rules.

3.1   PRELIMINARY ANALYSIS

The assessment of the scales of the fire plume and its ceiling jet is here presented and organized into several paragraphs, each one representing a preliminary analysis before doing any spectral analysis.

Firstly, in Par. 3.1.1 a preliminary estimation of the characteristic largest and finest scales of the plume and its ceiling jet is performed. This assessment gives us an insight of the 'true' spectrum extensions that could be obtained with a DNS. This can lead us to understand the limitation of our numerical calculations, which are performed with a LES approach.

A further step in the preliminary analysis, is the comparison of the results of our numerical calculations with the analytical models available in literature. This is not only to assess the reliability of our calculation, but also to check our capacity to do *a priori* predictions of the scale of interest in order to have additional data for the choice of the grid. One of the scales that is a best practice to compare with the analytical models is the flame height. In particular, in Par 3.1.2 our numerical results and the ones of Cetegen's analytical [103] model are compared. Furthermore to have an insight of the flow velocity of our problem we compared our results produced by the numerical calculations with those obtained with analytical models available in literature [104-105] for both the flows.

A further quantity assessed for our plume and its ceiling jet is the turbulence intensity. In Par. 1.2.2, we already discussed the use of this quantity to define the applicability of the TH.

3.1.1 Estimation of the Largest and Finest Scales

In a boundary free shear flow, such as the fire plume, the identification of the upper and lower length scales can be a critical task. In these flows it is not possible to assign as characteristic length (D in the following) the dimension of the field because it is not confined. This issue is reflected also on the estimation of the finest scale in the turbulent flow (Kolmogorov scale, ℓ, in the following), that is usually estimated using the so-called Kolmogorov scale relation, described for instance by Tennekes and Lumley [10]:

$$\frac{\ell}{D} \propto Re^{-3/4} \tag{3.1}$$

Despite the relationship of proportionality of Eq. (3.1) cannot lead to a precise calculation of the Kolmogorov scale, our scope is to use it to find an order of magnitude of this length scale. In this paragraph, we discuss the approaches to estimate the main parameters involved in Eq. (3.1): the characteristic length (D in the following), the characteristic velocity and the kinematic viscosity, (ν in the following). The characteristic length D was calculated with different methodologies by several Authors:

- D = $l_{U/2}$, twice the distance from the centre up to the point where the half of the maximum vertical component of the time-averaged velocity is reached (Shabbir and George [106]),

- D = $l_{T/2}$, twice the distance from the centre up to the point where the half of the maximum of the time-averaged temperature is reached (Antonia et al. [107]),

- D = D*, characteristic fire diameter (Drysdale [3]),

Together with these approaches found in literature to calculate the characteristic length D, we have also considered:

- D = D_h, the hydraulic diameter:

$$D_h = 4A/per \tag{3.2}$$

where per is the perimeter of the square burner,

- D=D_{CO2}, the distance between the points where the carbon dioxide concentration reaches the value of $\varphi_{CO2,D}$:

$$\varphi_{CO2,D} = \varphi_{CO2,min} + 0.1(\varphi_{CO2,max} - \varphi_{CO2,min}) \tag{3.3}$$

where $\varphi_{CO2,min}$ is the minimum carbon dioxide concentration and $\varphi_{CO2,max}$ is the maximum carbon dioxide concentration. Since the combustion products include carbon dioxide, we used its concentration to track the presence of the smoke. In Figure 3.1 for the finer grid we compare the carbon dioxide concentration time-averaged in the interval 80.000 s$\leq t_k \leq$80.001 s with that time-averaged in the interval 20 s$\leq t_k \leq$100 s. The carbon dioxide concentration time-averaged in the more extended interval is distributed in a wider spatial range than the one calculated in the interval 80.000 s$\leq t_k \leq$80.001 s. This is due to the horizontal fluctuations of the fire plume that can transport the gases increasing the values of the carbon dioxide concentration if time-averaged on extended time intervals. To avoid the overestimation of D_{CO2}, the carbon dioxide concentration is calculated in the interval 80.000 s$\leq t_k \leq$80.001 s.

In Tab. 3.1 the values of characteristic length D are summarized, for the different grids, at 5 m above ground. For the coarser grid $l_{U/2}$ is underpredicted while $l_{T/2}$ is overpredicted when compared with the values of the finer grid. D_{CO2} gives for the three grids comparable results. The velocity considered for the Reynolds number calculation is the bulk velocity (U_{bulk} in the following) that is calculated as:

$$U_{bulk} = \frac{\int_S \rho \cdot (\overline{u} \cdot \overline{n}) dS}{\int_S \rho dS} \tag{3.4}$$

where ρ is the time-averaged density, $\overline{u}$ is the velocity vector, $\overline{n}$ is the versor normal to the considered plane having surface S. Here, Eq. (3.4) can be rewritten as:

$$U_{bulk} = \frac{\int_S \rho u_3 dS}{\int_S \rho dS} \tag{3.5}$$

where u_3 is the vertical time-averaged velocity component. Since the smoke plume typically shows a truncated cone pattern starting from the source of the fire our plane, its horizontal section is disk. For this reason we divided the domain in annuli (see Figure 3.2), each one divided in four sectors of annulus, so the U_{bulk} is numerically calculated
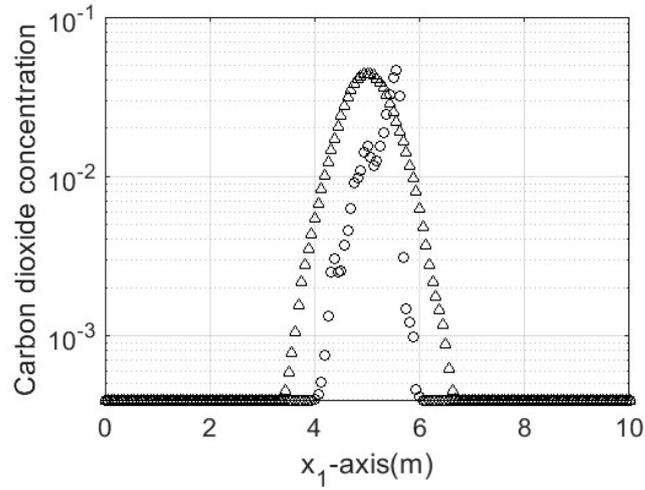
Figure 3.1: Carbon dioxide concentration: disk:($\circ$) calculated in 0.001s;triangle ($\triangle$):

time-averaged $20\,\text{s} \leq t_k \leq 100\,\text{s}$, FG.

Table 3.1: Summary of the characteristic length of the plume, D.

D (m)	CG	MG	FG
$l_{U/2}$	1.53	3.83	4.00
$l_{T/2}$	1.30	1.07	1.14
D*	1.83	1.83	1.83
D_h	1.50	1.50	1.50
D_{CO2}	1.92	1.93	1.94
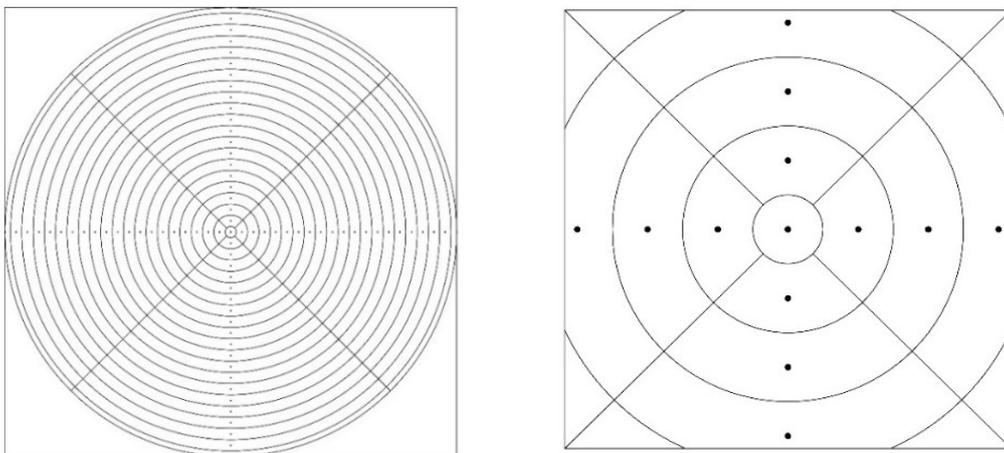
Figure 3.2: Division of the plane in sector of annuli (left) and its detail in the centre

(right).

along the radius, as:

$$U_{bulk} = \frac{\sum\limits_{n=1}^{N} \rho_n\, u_{3,n}\, S_n}{\sum\limits_{n=1}^{N} \rho_n\, S_n} \tag{3.6}$$

where ρ_n and $u_{3,n}$ are, respectively, the time-averaged density and the vertical velocity component in each sector of annulus having area S_n.

The kinematic viscosity, ν, is obtained by linearly interpolating the values from the table of White [108], using the bulk temperature at 5 m above the ground. The bulk temperature, T_{bulk} is calculated as:

$$T_{bulk} = \frac{\sum\limits_{n=1}^{N} \rho_n\, c_{p,n}\, T_n\, u_{3,n}\, S_n}{\sum\limits_{i=1}^{N} \rho_n\, c_{p,n}\, S_n} \tag{3.7}$$

where $c_{p,n}$, and T_n are, respectively, the time-averaged specific heat at constant pressure and the temperature in each sector of annulus having area S_n. Figure 3.3 and Figure 3.4 show the bulk velocity and bulk temperature graphs for the FG. In Tab. 3.2, the results of U_{bulk}, T_{bulk} and ν are shown, where the summations in the Eqs. (3.6-3.7) are limited to the annuli up to 2 m of distance from the centre.
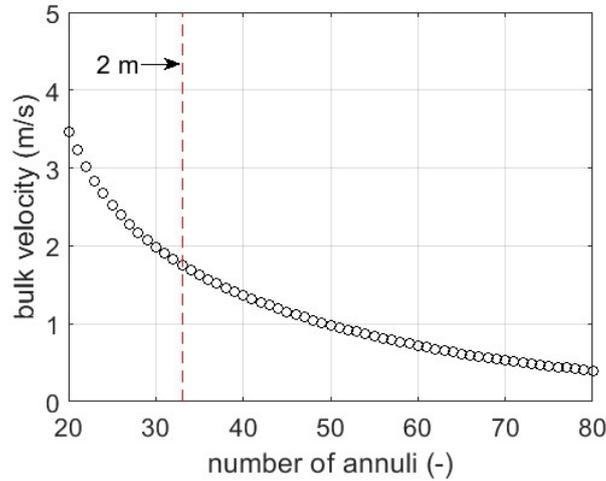
Figure 3.3: Bulk velocity graph at 5 m of height above ground, FG.
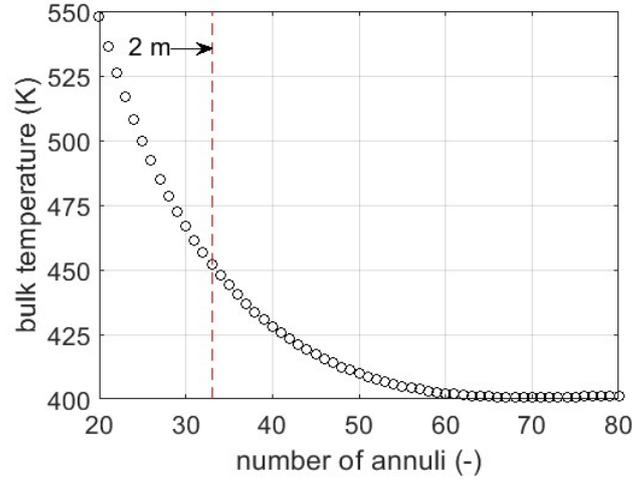
Figure 3.4: Bulk temperature graph at 5 m of height above ground, FG

The Reynolds number and the Kolmogorov lengths ℓ are summarized in Tab. 3.3 and Tab. 3.4, respectively. It can be noted that the Kolmogorov length, ℓ, lies within the same order of magnitude in a range of $2 \cdot 10^{-4}$ m $\leq \ell \leq 3 \cdot 10^{-4}$ m. Thus the calculations of ℓ are weakly affected by the choice of the characteristic length D. This range of value is far below the finest grid size ($62.5 \cdot 10^{-3}$ m). This has an immediate consequence on the wavenumbers because the wavenumber cut-off due to the grid size (proportional to $1/\Delta x$) is always far lower than the highest wavenumber (proportional to $1/\ell$). Thus, the highest possible frequency of the plume is far higher than the resolved ones.

For the ceiling jet, we also estimated the Kolmogorov scale using Eq. (3.1) to look for an insight of the extension of the *tke* spectrum before doing any spectral analysis. Since the Reynolds number varies along the ceiling jet, for an order of magnitude evaluation we calculate the Kolmogorov scale at 1.5 m, 3.0 m, 4.5 m from the axis. The ceiling jet Reynolds number is calculated with the velocity modulus and the thickness of

Table 3.2: Values of plume velocity, temperature and viscosity summarized.

	CG	MG	FG
U_{bulk} (m/s)	2.00	1.81	1.75
T_{bulk}(K)	148.3	174.2	179.0
ν (m²/s)	$2.17 \cdot 10^{-05}$	$2.28 \cdot 10^{-05}$	$2.30\ 10^{-05}$

Table 3.3: Plume Reynolds number for the different grids, largest scale and velocities considered.

	Re (-)		
	CG	MG	FG
$l_{U/2}$	$14.1 \cdot 10^4$	$30.2 \cdot 10^4$	$30.4 \cdot 10^4$
$l_{T/2}$	$12.0 \cdot 10^4$	$8.4 \cdot 10^4$	$8.7.4 \cdot 10^4$
D^*	$17.0 \cdot 10^4$	$14.4 \cdot 10^4$	$13.9 \cdot 10^4$
D_h	$13.8 \cdot 10^4$	$11.9 \cdot 10^4$	$11.4 \cdot 10^4$
D_{CO2}	$17.7 \cdot 10^4$	$12.3 \cdot 10^4$	$14.8 \cdot 10^4$

Table 3.4: Finest scale of the plume for the different grids, largest scale and velocities considered.

	ℓ (m)		
	CG	MG	FG
$l_{U/2}$	$2 \cdot 10^{-4}$	$3 \cdot 10^{-4}$	$3 \cdot 10^{-4}$
$l_{T/2}$	$2 \cdot 10^{-4}$	$2 \cdot 10^{-4}$	$2 \cdot 10^{-4}$
D^*	$2 \cdot 10^{-4}$	$3 \cdot 10^{-4}$	$3 \cdot 10^{-4}$
D_h	$2 \cdot 10^{-4}$	$2 \cdot 10^{-4}$	$2 \cdot 10^{-4}$
D_{CO2}	$2 \cdot 10^{-4}$	$2 \cdot 10^{-4}$	$3 \cdot 10^{-4}$

the ceiling jet as the characteristic parameters. In Figure 3.5 the soot density for the three grids is shown. The ceiling jet thickness is roughly graphically estimated using the ruler included in the FDS view of the soot density. The value of thickness is 0.6 m $\pm$ 0.2 m (0.2 m is the resolution of the ruler) for the three grids. The modulus of the velocity (U_{CJ} in the following) for the three different grids, at different distances from the centre-line is reported in Tab. 3.5. The Reynolds numbers are reported in Tab. 3.6, whereas the Kolmogorov scales are reported in Tab. 3.7. The Kolmogorov scales of the ceiling jet are then in the range $7 \ 10^{-5}$ m$\leq \ell \leq 13 \ 10^{-5}$ m, then below the range of the Kolmogorov scale in the plume and far below the finest grid size ($62.5 \cdot 10^{-3}$ m). We have to expect the highest wavenumber far higher than the wavenumber cut-off due to the grid size. Thus, the highest possible frequency of the ceiling jet is far higher than the resolved ones.

Table 3.5: Modulus of velocity in the ceiling jet for the three different grid, at the three different position.

x_1	U_{CJ} (m/s)		
	CG	MG	FG
1.5 m	3.8	4.1	4.3
3.0 m	2.6	3.4	3.6
4.5 m	2.0	2.7	3.0

Table 3.6: Ceiling Jet Reynolds number for the different grids, at the three different positions.

x_1	Re (-)		
	CG	MG	FG
1.5 m	$1.5 \ 10^5$	$1.6 \ 10^5$	$1.7 \ 10^5$
3.0 m	$1.0 \ 10^5$	$1.3 \ 10^5$	$1.4 \ 10^5$
4.5 m	$0.8 \ 10^5$	$1.0 \ 10^5$	$1.2 \ 10^5$

Table 3.7: Ceiling jet Kolmogorov scale for the different grids, at the three different positions.

| x_1	ℓ (m)		
	CG	MG	FG
1.5 m	$8 \ 10^{-5}$	$7 \ 10^{-5}$	$7 \cdot 10^{-5}$
3.0 m	$10 \ 10^{-5}$	$9 \ 10^{-5}$	$8 \ 10^{-5}$
4.5 m	$13 \ 10^{-5}$	$10 \ 10^{-5}$	$9 \ 10^{-5}$
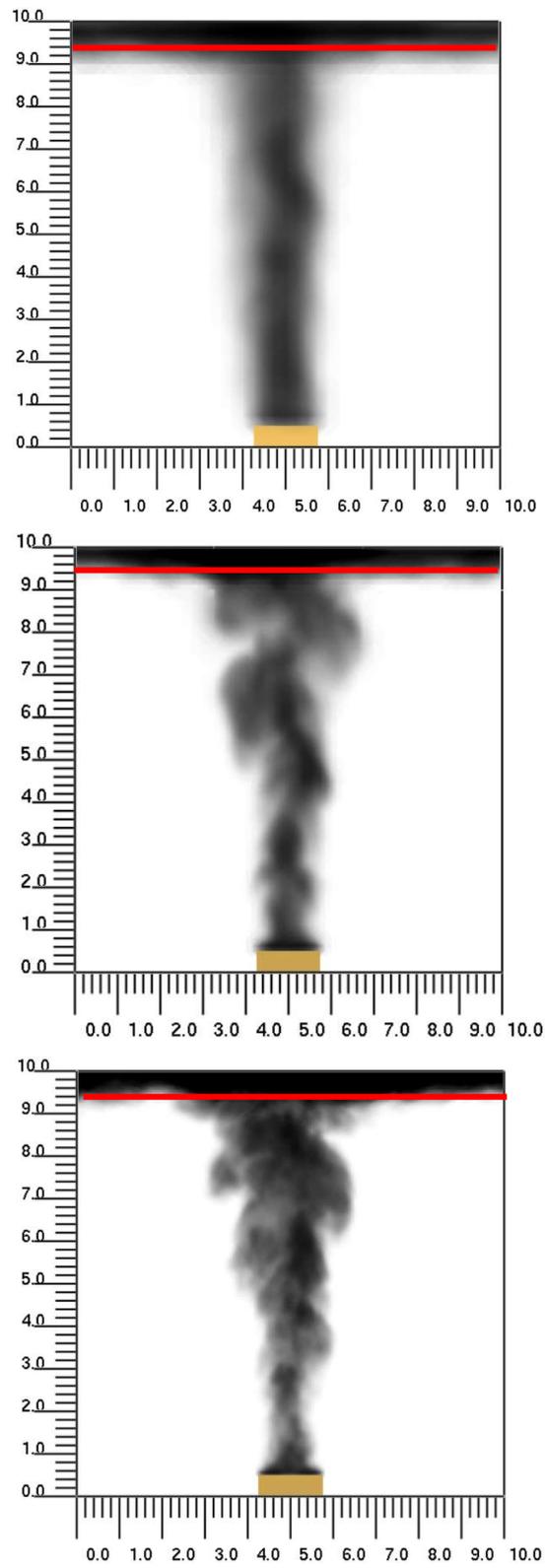
Figure 3.5: Soot Density, CG (top), MG (middle) and FG (bottom)

3.1.2 Estimation of the flame height and comparison with the results of Cetegen analytical model

A characteristic length analysed for fire safety engineering purposes is the height of the flame above a burning fuel bed (flame height, LH, in the following), as this will determine how the flame will interact with its surroundings. Because of this importance, the estimation of the flame height has been the object of many studies by different Authors [103, 109-112]. Among the researches, we used, for comparison purposes with our numerical results, the analytical method proposed by Cetegen et al. [103] (Cetegen's model in the following) that considers the two different equations:

$$Q^* < 1 \qquad LH = 3.3\ Q^{*2/3} D_{S\text{-}C} \qquad\qquad (3.8)$$

$$Q^* \geq 1 \qquad LH = 3.3\ Q^{*2/5} D_{S\text{-}C} \qquad\qquad (3.9)$$

where $D_{S\text{-}C}$ is $\sqrt{4A/\pi}$ and the value of Q^* is defined in Eq. (2.2). As from Par. 2.1, our Q^* is 1.2, then Eq. (3.9) should be used. The flame height calculated with Cetegen's model is 6.02 m. It is reported in Tab. 3.8 labelled as "Cetegen".

Due to the intermittent nature of the flame, the flame height has always been a discussed concept. The flame height was defined by McDermott et al. [113] and in the FDS documentation [94, 99] as the distance above the burner, on time-average, at which 99% of the fuel has been consumed. This is obtained numerically calculating the heat release rate per unit length (HRR') in a horizontal plane for each increment in x_3:

$$HRR'(x_{3,s}) = \sum_{h=1}^{H}\sum_{q=1}^{Q} q'''(x_{1,h}, x_{2,q}, x_{3,s})\Delta x_{1,h}\,\Delta x_{2,q} \qquad\qquad (3.10)$$

where $x_{1,h}$, $x_{2,q}$ and $x_{3,s}$ are the discrete coordinates, $\Delta x_{1,h}$ and $\Delta x_{2,q}$ are the step size for the coordinate $x_{1,h}$ and $x_{2,q}$ and q''' is the specific heat release rate in each cell centroid. Thus, the flame height is the distance from the burner up to the point where the cumulative of HRR'$(x_{3,s})\cdot\Delta x_{3,s}$ (CHRR in the following), reaches the 99% of the time-averaged HRR over the time interval 20 s$\leq t_k \leq$100 s (HRR$_{PL}$ in the following). For our case study, as expected from the input HRR, the HRR$_{PL}$ is 5000 kW (see Figure 3.6), so the 99% of the

Table 3.8: Comparison of LH calculated with FDS and with Cetegen's model.

Δx	Flame Height (LH)		
	95% (m)	Cetegen (m)	99% (m)
CG	3.89	6.02	5.48
MG	5.35	6.02	7.09
FG	5.82	6.02	7.09

HRR_{PL} is reached at 4950 kW. In Figure 3.7 the CHRR for the different grids are shown with an indication of the flame height and a polynomial interpolation (see Tab. 3.9). The value of flame height calculated as the height at which 99% of the fuel has been consumed are reported in Tab. 3.8 labelled as "99%". It can be noted that the CG leads to a flame height of 23% lower than the FG. In Figure 3.8 the isosurface of heat release rate per unit of volume (HRRPUV in the following) at 80 kW/m^3, are shown respectively for CG, MG, FG. This value of HRRPUV is used as default to graphically estimate the flame height. The tip of the flames of Figure 3.8 are in accordance with the one calculated, considering that the burner is placed on a support of 0.5 m of height.

For a comparison, the value of flame height calculated as the height at which 95% of the fuel has been consumed are also reported in Tab. 3.8 labelled as "95%". For the MG and FG the flame height lies in the range between the 95% and a 99% of the HRR_{PL} as shown in the Validation guide [95], whereas in the CG the flame height seems under-predicted.

Table 3.9: Polynomial fitting of the CHRR.

Δx	5th degree polynomial fitting function
CG	CHRR=$-0.2386z^5+5.652z^4-37.4z^3-48.57z^2+1294z+1566$
MG	CHRR=$-0.0669z^5+3.795z^4-55.222z^3+222.39z^2+613.65z+732.12$
FG	CHRR=$0.1927z^5-2.5638z^4-3.1967z^3+73.044z^2+714.383z+409.82$
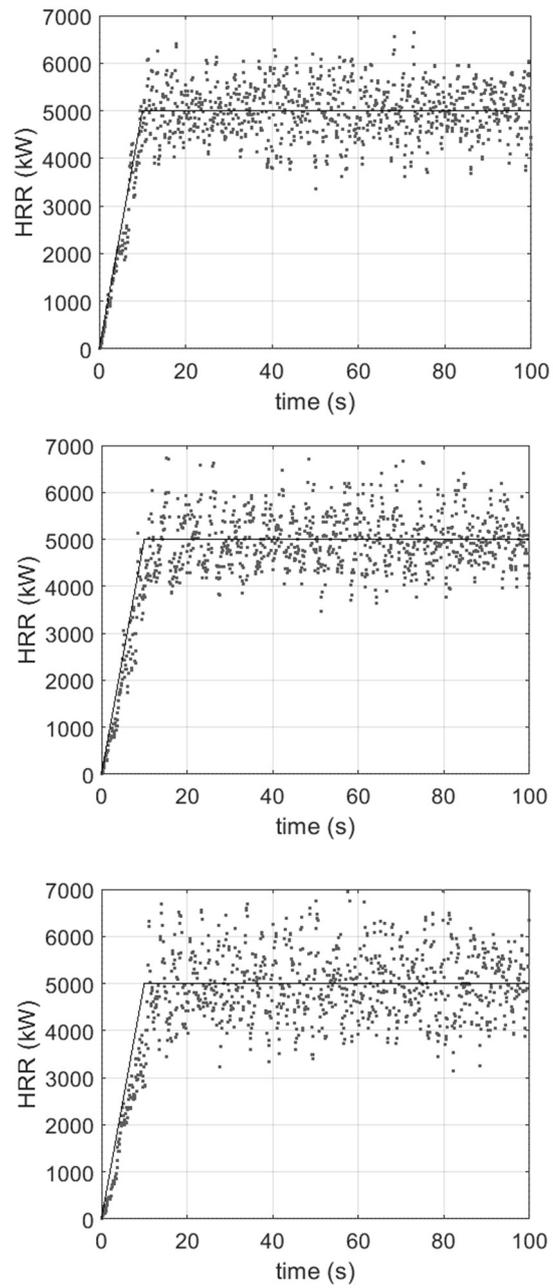
Figure 3.6: HRR curve, input (black line) and output (grey dot), CG (top), MG (middle) and FG(bottom).
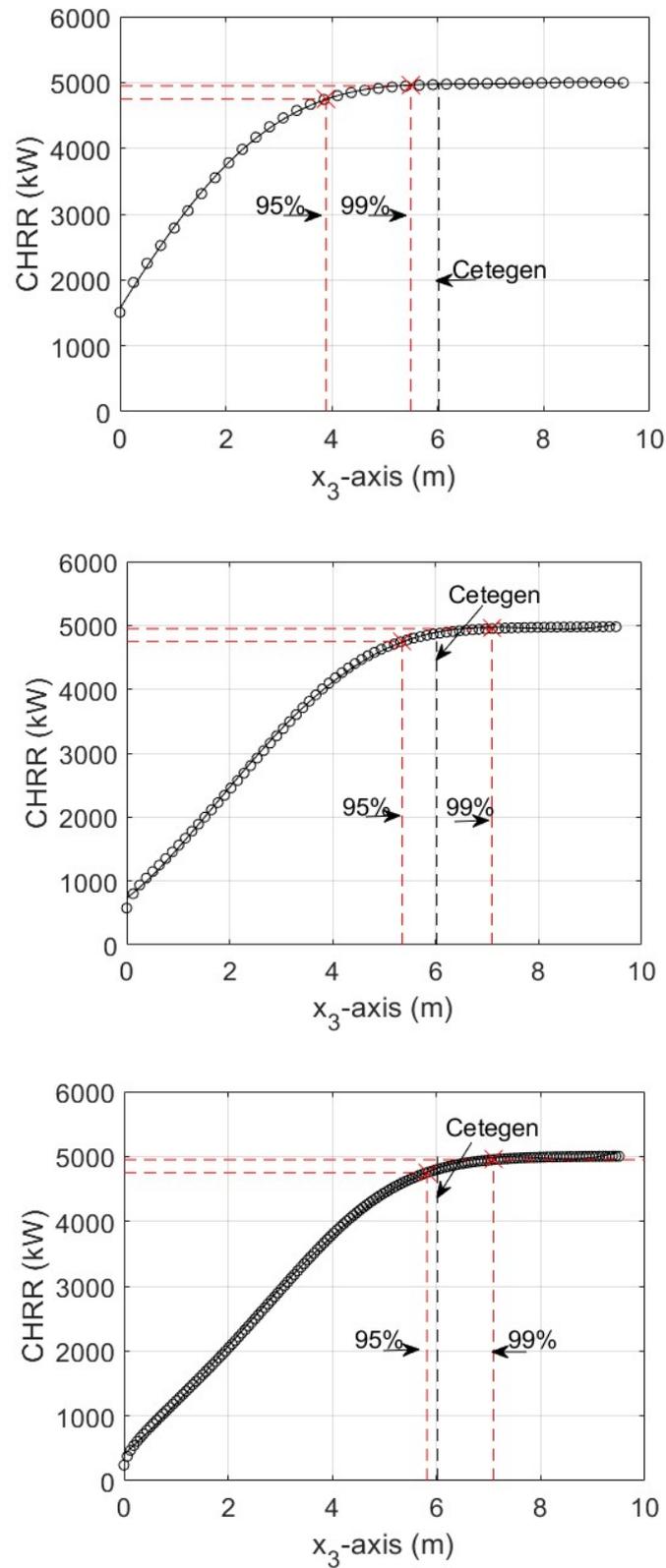
Figure 3.7: CHRR for the different grids, CG (top), MG(middle) and FG (bottom).
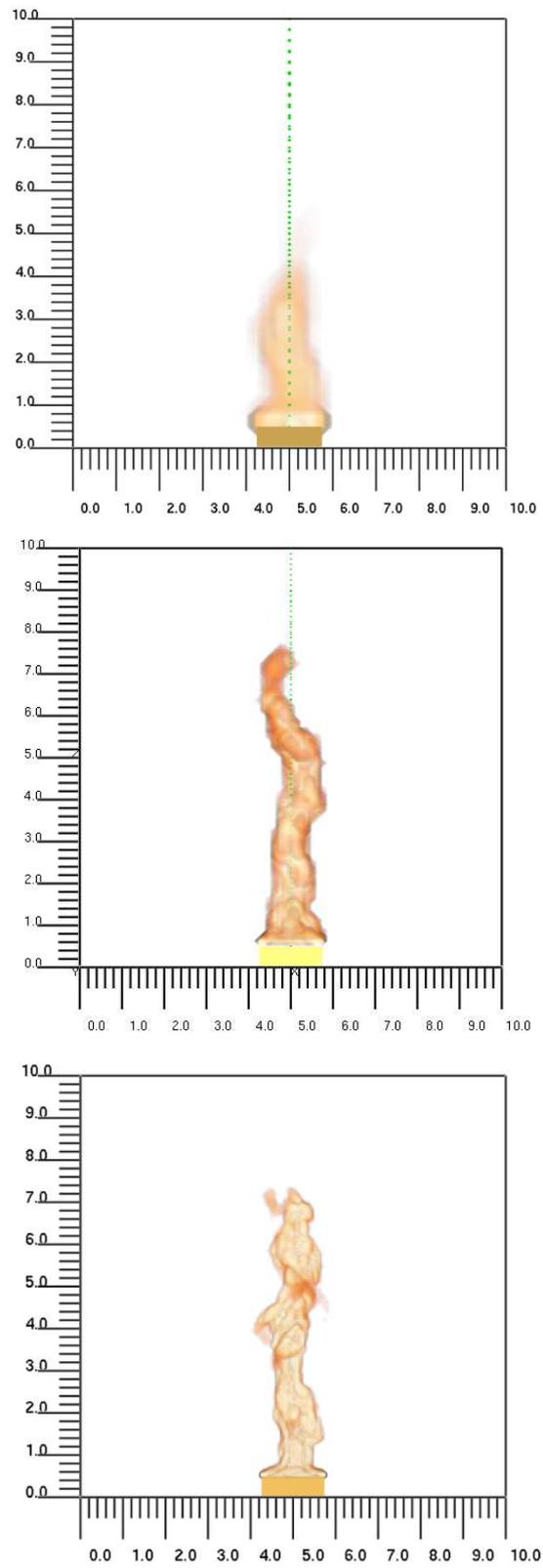
Figure 3.8: Isosurface: HRRPUV=80 kW/m^3, CG (top), MG(middle) and FG (bottom).

3.1.3   Numerical/Analytical comparison

The comparison of the velocity profile calculated by FDS with the one calculated with an analytical model allows us to assess the reliability of our numerical calculation. Furthermore the analytical model can give us important information that we can use during the choice of the grid, as we will see in Par. 3.2 and Par. 3.3.

McCaffrey [104] proposes an analytical model that allows to obtain the time-averaged vertical velocity, $U_{McCaffrey}$, along the centre-line of the plume as:

$$U_{McCaffrey} = \chi \left(\frac{x_3}{\dot{Q}^{2/5}} \right)^{\eta} \dot{Q}^{1/5} \tag{3.11}$$

where x_3 is the height from the burner at which the vertical velocity is calculated, the parameter χ and η depend on the characteristics of the region where we calculate $U_{McCaffrey}$. McCaffrey [104] classifies three regions based on the value assumed by $x_3/\dot{Q}^{2/5}$:

$$\frac{x_3}{\dot{Q}^{2/5}} < 0.08 \qquad\qquad \text{Flame}$$

$$0.08 \le \frac{x_3}{\dot{Q}^{2/5}} \le 0.2 \qquad\qquad \text{Intermittent}$$

$$\frac{x_3}{\dot{Q}^{2/5}} > 0.2 \qquad\qquad \text{Plume}$$

Based on the region, the values of χ and η are:

$$\chi = 6.8 \; \frac{m^{1/2}}{s} \qquad\qquad \eta = 1/2 \qquad\qquad \text{Flame}$$

$$\chi = 1.9 \; \frac{m}{s \, kW^{1/5}} \qquad\qquad \eta = 0 \qquad\qquad \text{Intermittent}$$

$$\chi = 1.1 \; \frac{m}{s \, kW^{1/5}} \qquad\qquad \eta = -1/3 \qquad\qquad \text{Plume}$$

Thus, if we want to analyse the $U_{McCaffrey}$ at 4.5 m from the burner (5 m from the base of

the domain) as we do in Par. 3.2, $x_3/\dot{Q}^{2/5}$ is 0.15. So Eq. (3.11) become:

$$U_{McCaffrey} = 1.9\,\dot{Q}^{1/5} \qquad (3.12)$$

$U_{McCaffrey}$ at 4.5 from the burner is then 10.4 m/s, 2% higher than the value calculated by FDS with $\Delta x = 0.0625$ m of 10.2 m/s. The vertical velocity profile obtained with FDS (using the FG) is compared with McCaffrey's analytical model in Figure 3.9. The two velocity profiles shows a good agreement up to about 7 m. This discrepancy downstream this height is due to the McCaffrey model that does not take into account the presence of an impingement above the plume.

A similar comparison can be done between the results of our LES calculations and the analytical model developed by Alpert [105] able to predict the modulus of the velocity along the surface of a ceiling jet (we refer to this velocity as U_{ALPERT} in the following). Alpert [105] defines two zones depending on the ratio between the radial distance from the centre of the ceiling jet (d in the following) and the height of the compartment above the burner (ht in the following). Thus the time-averaged velocity modulus in the ceiling
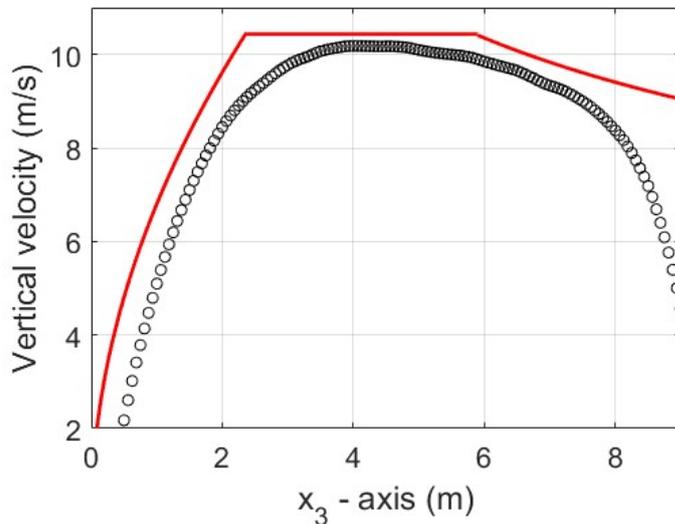
Figure 3.9: Vertical velocity along the centre-line of the plume: white disk (O) with FDS and Cetegen's model (red line).

jet is:

$$U_{Alpert} = \frac{0.195 \dot{Q}^{1/3} ht^{1/2}}{d^{5/6}} \tag{3.13}$$

for d/ht greater than 0.15 and

$$U_{Alpert} = 0.96 \left(\frac{\dot{Q}}{ht} \right)^{1/3} \tag{3.14}$$

for d/ht finer than 0.15.

In Figure 3.10 the time average modulus of the velocity profile calculated by FDS with FG is compared with U_{ALPERT}. In the turning zone the analytical model is not in agreement with the velocity profile. On the contrary, the agreement increases advancing away from the vertical centre-line.
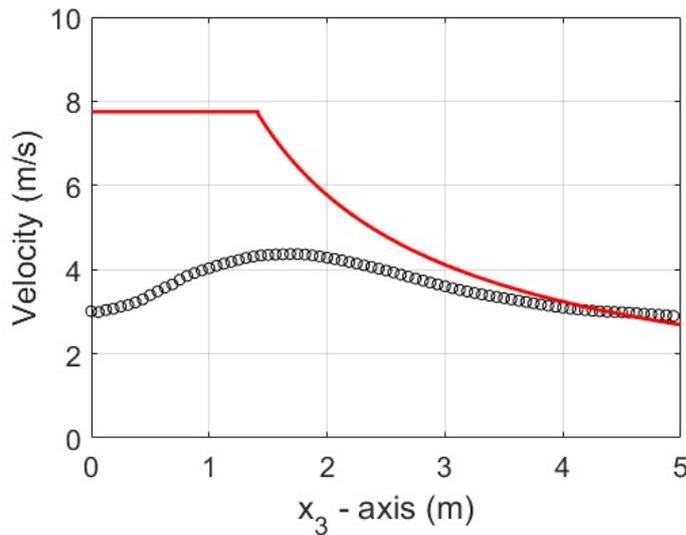
Figure 3.10: Modulus of the velocity profile along the radius of the ceiling jet: white disk (O) with FDS and Alpert's analytical model in red line.

3.1.4 Discussion on the Turbulence Intensity

As discussed in the Introduction, an important condition for the applicability of the TH is that the turbulent fluctuations are small compared to the mean velocity, in other words that the turbulence intensity must be low. The turbulence intensity is defined as:

$$I(\overline{x})= \frac{\sqrt{\frac{1}{3}\left(\langle u_1^2\rangle+\langle u_2^2\rangle+\langle u_3^2\rangle\right)}}{\sqrt{U_1^2+U_2^2+U_3^2}} \tag{3.15}$$

where the angle bracket, $\langle\ \rangle$, stands for the time-averaging.

An accepted criterion is to apply the TH to cases in which the turbulence intensity is less than 0.1 [114-115] .

In Figure 3.11 the turbulence intensity is shown, for the different grids, along the vertical centre-line of the plume. The results of the three grids show comparable turbulence intensity, with a minimum value about 0.15 near the burner support and with a maximum of about 1 near the ceiling. These values suggest high-turbulence. This evaluation is in line with the experimental results of a fire plume carried out by Westenberg and Rice [51].

As indicated in the Introduction, downstream the turning zone, where the free shear flow of the plume impinges the ceiling, the free shear flow becomes the ceiling jet, which
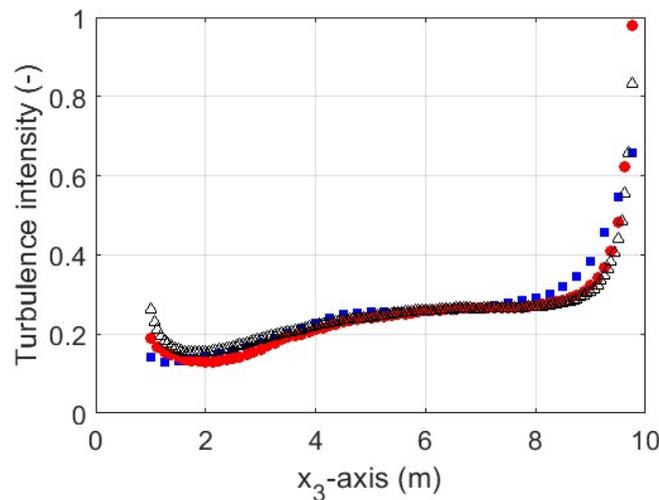
Figure 3.11: Turbulence intensity along the vertical centre-line of the plume. Blue square: (■) CG, red disk: (●) MG, white triangle: (△) FG.

is a wall bounded shear flow. In free shear flows many experiments (e.g., Tong and Warhaft [116]) have shown TH to fail, but no experiments including the measure of the turbulence intensity of the ceiling jet have been found.

In Figure 3.12 the turbulence intensity is shown, for the different grids, along the radius of the ceiling jet. As we go further away from the plume centre-line, the differences between the CG and the cases with finer grids become higher.

The turbulence intensity has a minimum about 0.35 far from the centre-line, with a maximum about 0.6 in the centre-line of the plume. All these values exceed the reference 0.1, then can be classified as highly turbulent.
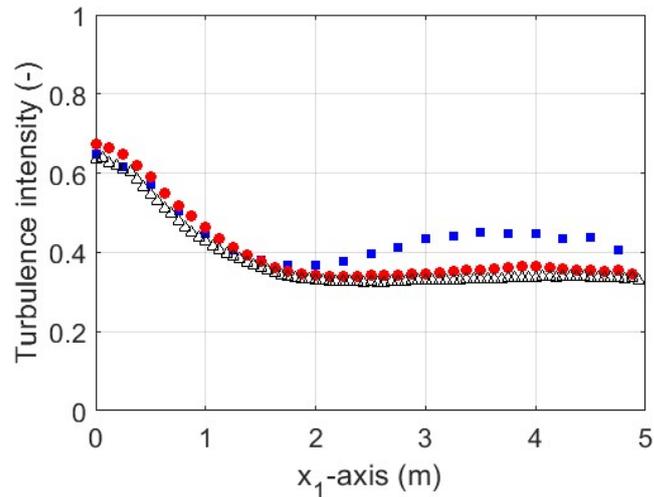
Figure 3.12: Turbulence intensity in the ceiling jet along a radius, Blue square: (■) CG, red disk: (●) MG, white triangle: (△) FG.

3.2   PLUME

In this paragraph, the results concerning the spectral analysis of the turbulent reacting plume are presented [117]. The dimensional analysis of the scale of the Par. 3.1.1 is used to provide a basis for the presentation of this spectral analysis. Furthermore, the results are interpreted taking in account also the information of the Par. 1.1.2 concerning the LES approach used in FDS that adopts implicit filtering.

In Figure 3.13 the results of the *tke* spectra of the plume in terms of frequency for the three grids are presented. These results are obtained calculating the *tke* spectra, in a centre-line cell at 5 m of height above the ground (d/L = 3, where L is the hydraulic diameter of the burner and d is the distance from the burner). Since the *tke* spectra are characterized by annoying fluctuations, which make them difficult to read, the signal has been Tukey windowed using intervals of 8 s with 2 s of overlapping (see for details Appendix B.2).

In these spectra of *tke*, the $-2/3$ power law feature, which can be derived from the Kolmogorov "-5/3 power law" for a PSD, is evident. For the coarser grid, obtained with the rule of thumb proposed by the FDS User Guide [91], (see Par. 2.1.1 for the discussion about the choice of the grid), the frequency range including the inertial sub-range is extremely restricted. As expected, the inertial sub-range widens for finer grids.

As described in the Par. 3.1 , the Kolmogorov scale, at 5 m of height above the ground, is in the range of $2 \cdot 10^{-4}$ m $\leq \ell \leq 3 \cdot 10^{-4}$ m, far below the finest grid size ($62.5 \cdot 10^{-3}$ m). This has an immediate consequence on the wavenumbers because the wavenumber cut-off due to the grid size (proportional to $1/\Delta x$) is far lower than the highest wavenumber (proportional to $1/\ell$). Thus, the highest possible frequency of the plume is far higher than the resolved ones.

In FDS an implicit grid filtering is used, so the filter size depends on the mesh spacing, uniform in this case study. In Figure 3.13, a region of the *tke* spectrum where the influence of this implicit filtering occurs, can be identified (Jameson and Bull [33]). This region is characterized by a strong attenuation, for this reason indicated as "attenuated region". It is bounded by two characteristic frequencies: the frequency where the trend of
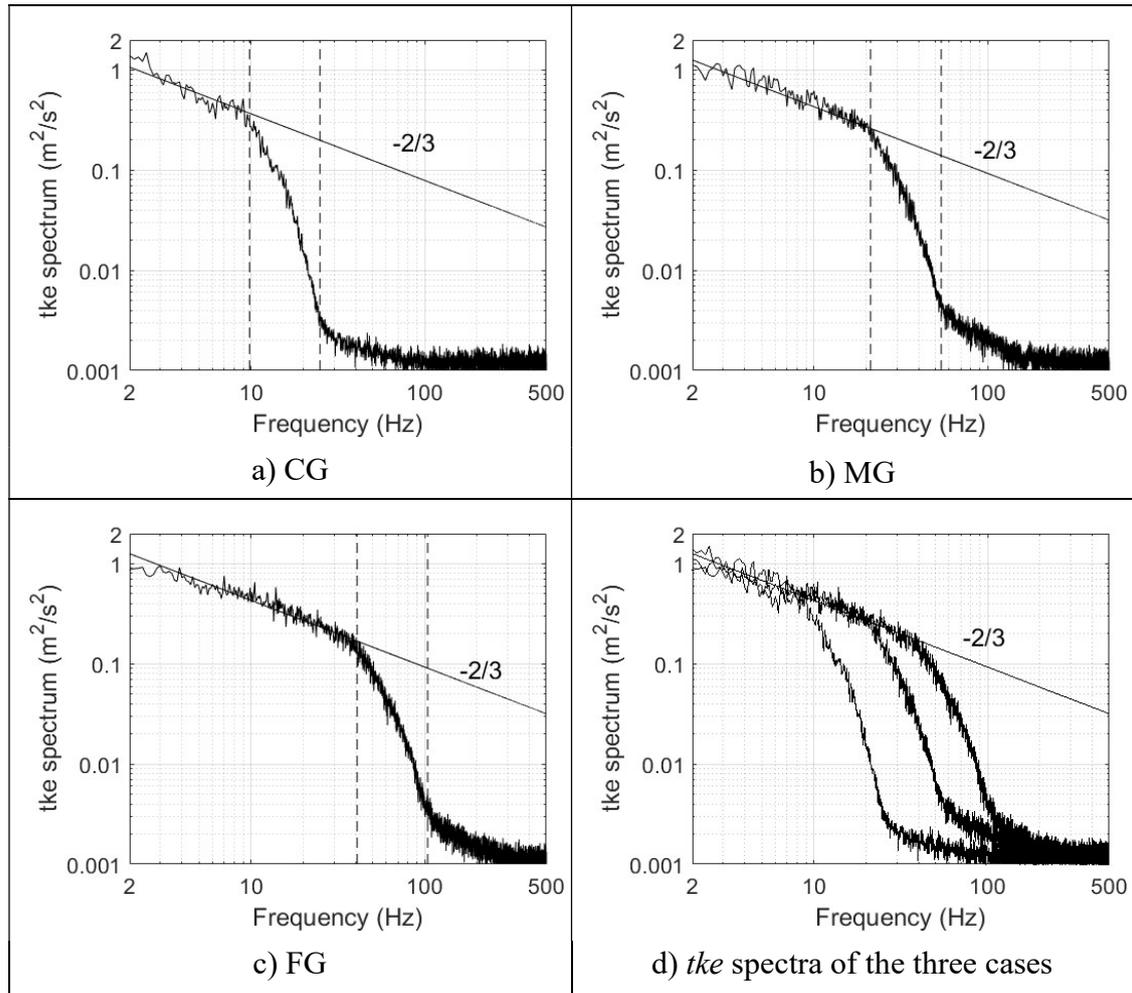
Figure 3.13: *tke* spectra in the frequency domain at 5 m of height. The dashed lines are f_{fc} and f_c.

the *tke* spectrum deviates from the -2/3 power law (f_{fc} in the following) and the frequency where the filter completes its action on the *tke* spectrum (f_c in the following). In Figure 3.13 both these frequencies, f_{fc} and f_c, are shown with dashed lines. With a direct graphical estimation of f_{fc} and f_c, we obtained the values reported in Table 3.10. It can be noted that these bounding frequencies increase the finer the grid.

In the *tke* spectrum the extension of the region characterized by the $-2/3$ power law feature can be a qualitative indicator to assess the quantity of resolved scales. Nevertheless, in the literature quality indicators able to give *a posteriori* quality metrics

Table 3.10: Values of frequency bounding the "attenuated region" in the plume.

	f_{fc} (Hz)			f_c (Hz)		
	CG	MG	FG	CG	MG	FG
From data	9.8	21.0	39.0	24.1	51.0	101.0
FDS	-	-	-	20.0	42.4	81.6
FDS/2	10.0	21.2	40.8	-	-	-
$\pi/2$	-	-	-	25.5	54.0	102.9

are usually preferred. They have been objects of study in the years by several Authors [118-119] and are still an active field of research. Among the most widely used, the one defined by Pope [120] is the fraction of the time-averaged modelled *tke* on the total one. Pope established that for homogeneous isotropic turbulence this parameter should not exceed the 20%, to ensure that the grid Nyquist limit is within the inertial sub-range.

The complementary to 1 of the quality indicator defined by Pope is

$$\mu = \frac{\langle tke \rangle}{\langle tke \rangle + \langle tke \rangle_{SGS}} \tag{3.16}$$

where the angle brackets denote the time-averaging, $\langle tke \rangle$ is the resolved time-averaged *tke* and $\langle tke \rangle_{SGS}$ is the sub-grid modelled time-averaged *tke*. The indicator μ is here calculated for the different grids and reported in Tab. 3.11. We also report in Tab. 3.11 the time-averaged sub-grid scale *tke* calculated directly with FDS and the resolved *tke*, both made dimensionless with the square of U for a comparison between the different grids. We also assess the dimensionless time-averaged *tke* related to the attenuated region. For the assessment of this parameter, differently from the analyses already presented involving the study of the *tke* spectrum, we use the PSDs of the fluctuating velocity components. The content of time-averaged resolved *tke* up to the frequency f is:

$$\langle tke \rangle (f) = \int_0^f psd(f')df' \tag{3.17}$$

where psd(f) is the sum of the PSDs of the fluctuating velocity components expressed as one-sided. Since we work in a numerical framework, Eq. (3.17) is used as:

$$\langle tke \rangle (f_{\text{lim}}) = \sum_{j=1}^{N} psd(f_j)(f_{j+1} - f_j) \qquad (3.18)$$

In Tab 3.11 the dimensionless time-averaged resolved tke up to the lower and upper frequency cut-off are also reported. The dimensionless time-averaged tke calculated by extending the "- 5/3 power law" of the psd(f) of each grid in the attenuated region between f_{fc} and f_{c} is indicated as $\langle tke \rangle_{-5/3}$ in Tab. 3.11. Finally, the ratio between [$\langle tke \rangle$ (f$_{\text{c}}$) - $\langle tke \rangle$ (f$_{\text{fc}}$)] and $\langle tke \rangle_{-5/3}$ is reported in Tab. 3.11.

As expected, μ increases the finer the grid. If we extend the Pope criterion to our case, the results pertaining to the coarser grid (78%) should be considered of poor quality. This could have been infered also from the restricted extension of the inertial sub-range in Fig. 3.13-a. The values of $\langle tke \rangle$ / U^2 for the different grids are highly comparable, whereas $\langle tke \rangle_{\text{SGS}}$ / U^2 decreases the finer the grid. In this point, $\langle tke \rangle_{\text{SGS}}$ / U^2 becomes a good quality indicator by itself, because it is highly grid dependent. As $\langle tke \rangle_{\text{SGS}}$ / U^2, the dimensionless $\langle tke \rangle_{-5/3}$ decreases the finer the grid. Finally, the dimensionless $\langle tke \rangle$ attributable to the attenuated region is by an order of magnitude lower than the other values reported in Tab. 3.11. It can be noted that time-averaged resolved tke in the attenuated region from f$_{\text{fc}}$ up to f$_{\text{c}}$ is always lower than $\langle tke \rangle_{-5/3}$. The ratio between [$\langle tke \rangle$ (f$_{\text{c}}$) - $\langle tke \rangle$ (f$_{\text{fc}}$)] and $\langle tke \rangle_{-5/3}$ is always small and decreases the coarser the grid. A significant fraction of resolved time-averaged tke is hence underestimated in the attenuated region. This issue is not addressed in the indicator defined by Pope, where the attenuated region is not accounted for.

In the application of the IWC method to our plume moving in the direction of x$_3$, the propagative and the dissipative dispersion graphs that relate the frequencies with the stream-wise wavenumbers k$_{3,p}$ and k$_{3,d}$ are obtained. As discussed in Par. 2.3.1, the propagative dispersion graph allows us to get the correlation-law, whereas the dissipative dispersion graph allows us to get information about the decay of the signal associated with the dissipation along the medium.

Table 3.11: Time-averaged *tke* fractions.

	CG	MG	FG
$\mu(\%)$	78	87	92
$\langle tke \rangle / U^2$	$8.68 \cdot 10^{-2}$	$8.67 \cdot 10^{-2}$	$8.72 \cdot 10^{-2}$
$\langle tke \rangle (f_c) / U^2$	$8.67 \cdot 10^{-2}$	$8.67 \cdot 10^{-2}$	$8.66 \cdot 10^{-2}$
$\langle tke \rangle (f_{fc}) / U^2$	$8.59 \cdot 10^{-2}$	$8.44 \cdot 10^{-2}$	$8.41 \cdot 10^{-2}$
$\langle tke \rangle_{SGS} / U^2$	$2.45 \cdot 10^{-2}$	$1.29 \cdot 10^{-2}$	$0.77 \cdot 10^{-2}$
$[\langle tke \rangle (f_c) - \langle tke \rangle (f_{fc})] / U^2$	$8.18 \cdot 10^{-4}$	$23.0 \cdot 10^{-4}$	$25.6 \cdot 10^{-4}$
$\langle tke \rangle_{-5/3} / U^2$	$7.99 \cdot 10^{-3}$	$7.44 \cdot 10^{-3}$	$5.54 \cdot 10^{-3}$
$[\langle tke \rangle (f_c) - \langle tke \rangle (f_{fc})] / \langle tke \rangle_{-5/3}$	0.102	0.309	0.471

In Figure 3.14 for the three different grids, the results of the data reduction regarding only the propagative behaviour are presented. The dispersion graphs of Figure 3.14 show an area characterized by a high correlation, the "propagation area", and an area with a low correlation, the "non propagation area". In Figure 3.15 for the three grids the propagative and dissipative dispersion graph area is shown. The application of the IWC method to our plume flow, gives for each grid always zero dissipation wavenumbers. This suggests that, in the analyzed range of wavenumber, there is a prevalent propagative behaviour due to the large production of momentum by the buoyancy forces. No attenuation due to the dissipation can be revealed. In Figure 3.16 the propagation areas of the three dispersion graphs are shown together and the correlation-law is graphically highlighted. As expected, the propagation area widens as the grid resolution increases.

In Figure 3.17 the IWC parameter in frequency along with the dispersion graph for the different grids is shown. It can be seen that where the propagative areas of the dispersion graph ends, the IWC parameter in frequency drops sharply.
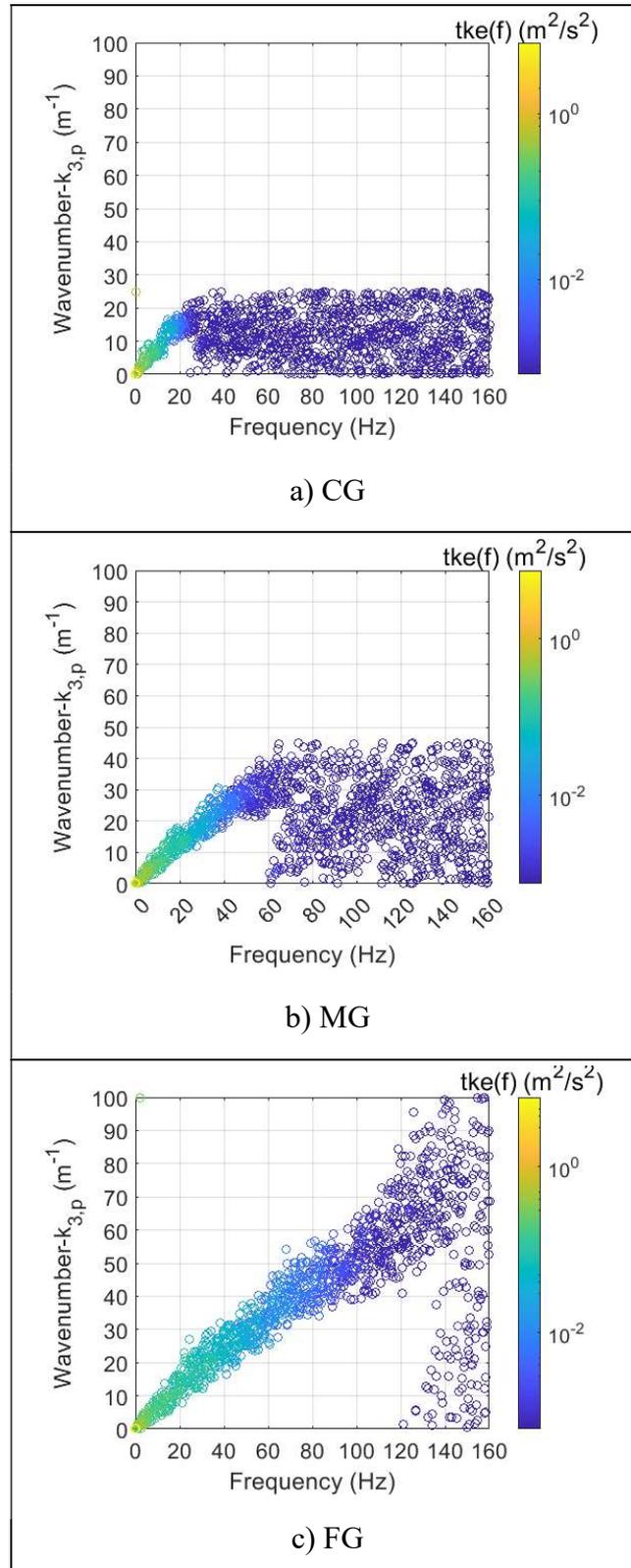
Figure 3.14**:** Propagative dispersion graphs
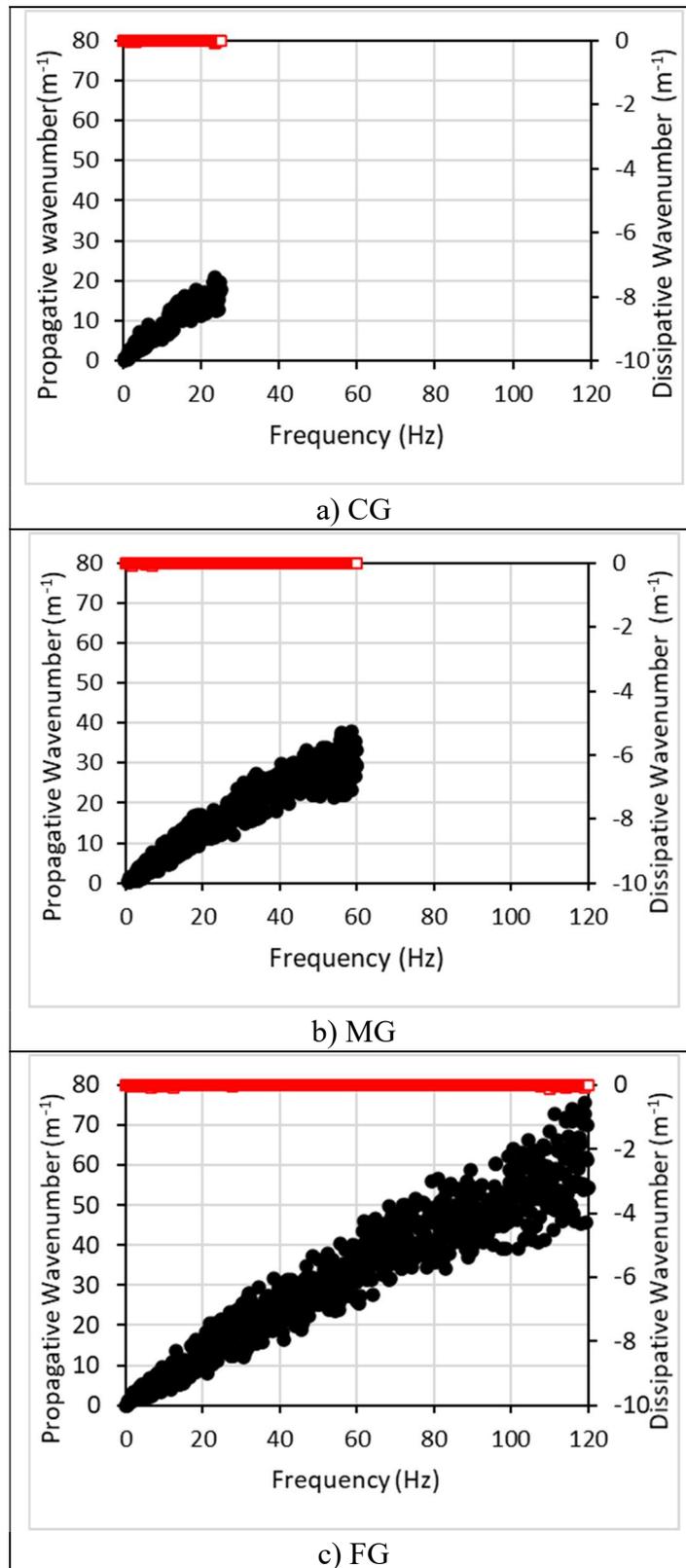
Figure 3.15: Dispersion graphs: black disk: (●) propagative component, red square: (□) dissipative component..
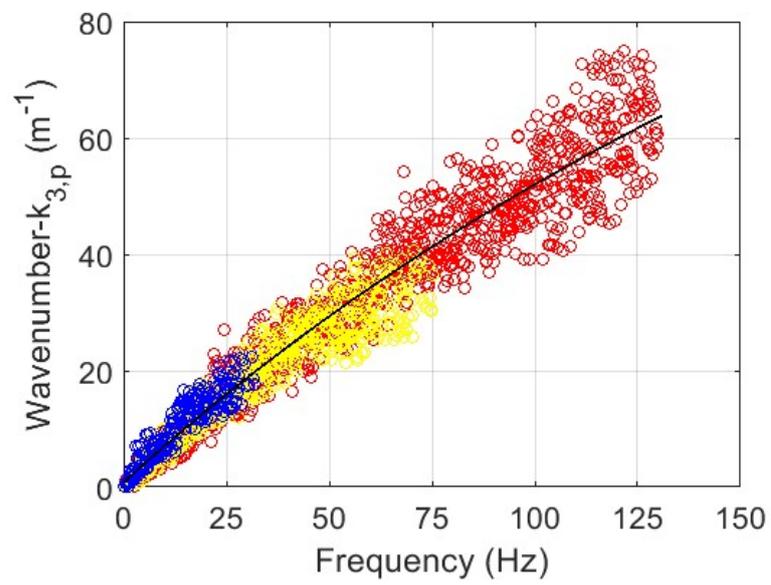
Figure 3.16: Propagation areas of the dispersion graphs of the three different grids.
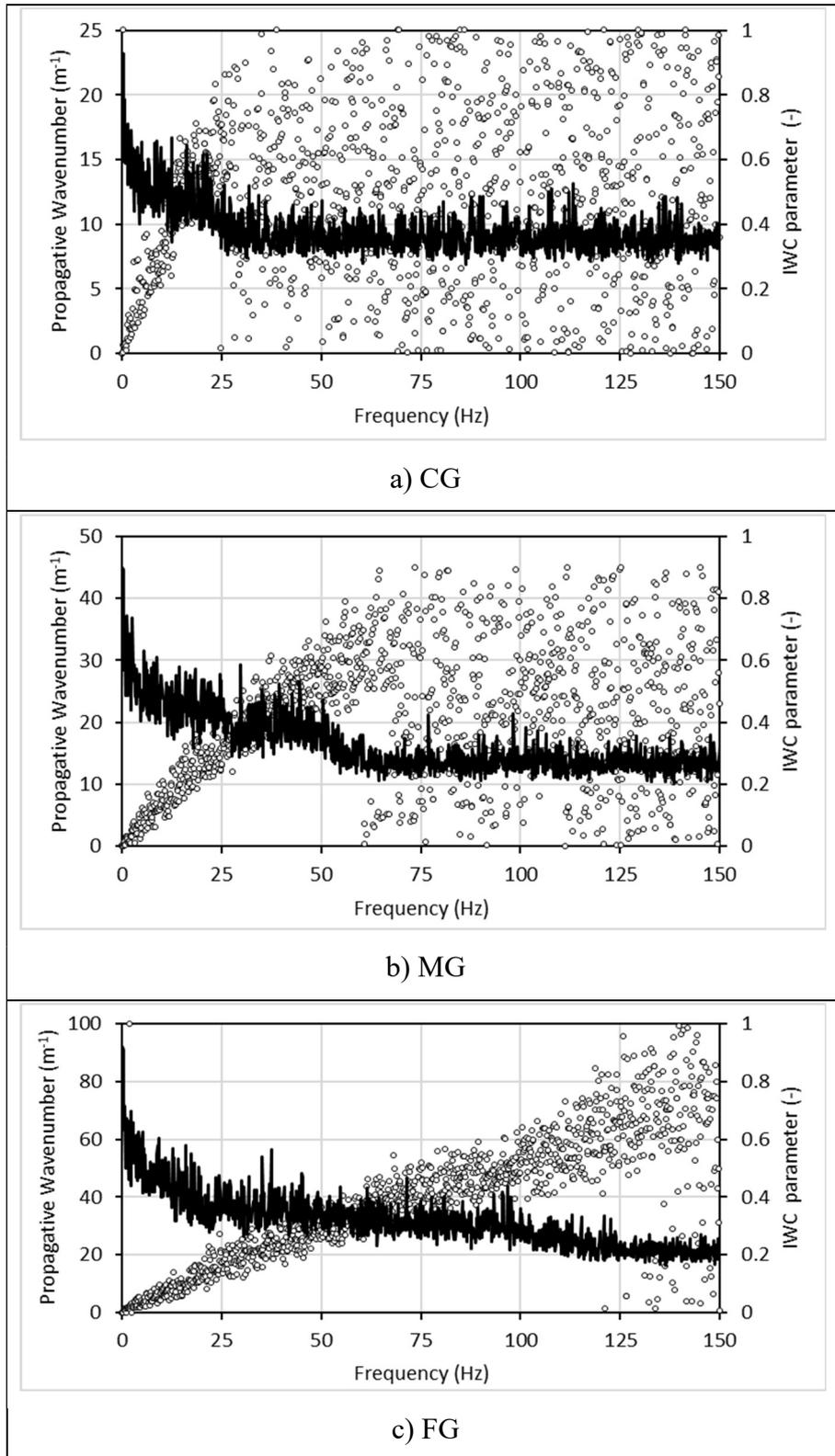
Figure 3.17: IWC parameter in frequency and the dispersion graph; white disk: (○) propagative component, black line: IWC parameter.

A further insight about the IWC method can be gathered also by analysing the steps of the IWC method. In Figure 3.18, the IWC parameter in the wavenumber domain is analysed and shown for the coarser grid, for different frequencies. The frequencies considered are 10 Hz, 15 Hz and 20 Hz, which are inside the propagative area of the dispersion graph, and the frequency 25 Hz which is in the non propagative area. The graphs of the IWC parameter in the wavenumber of the frequencies inside the propagative
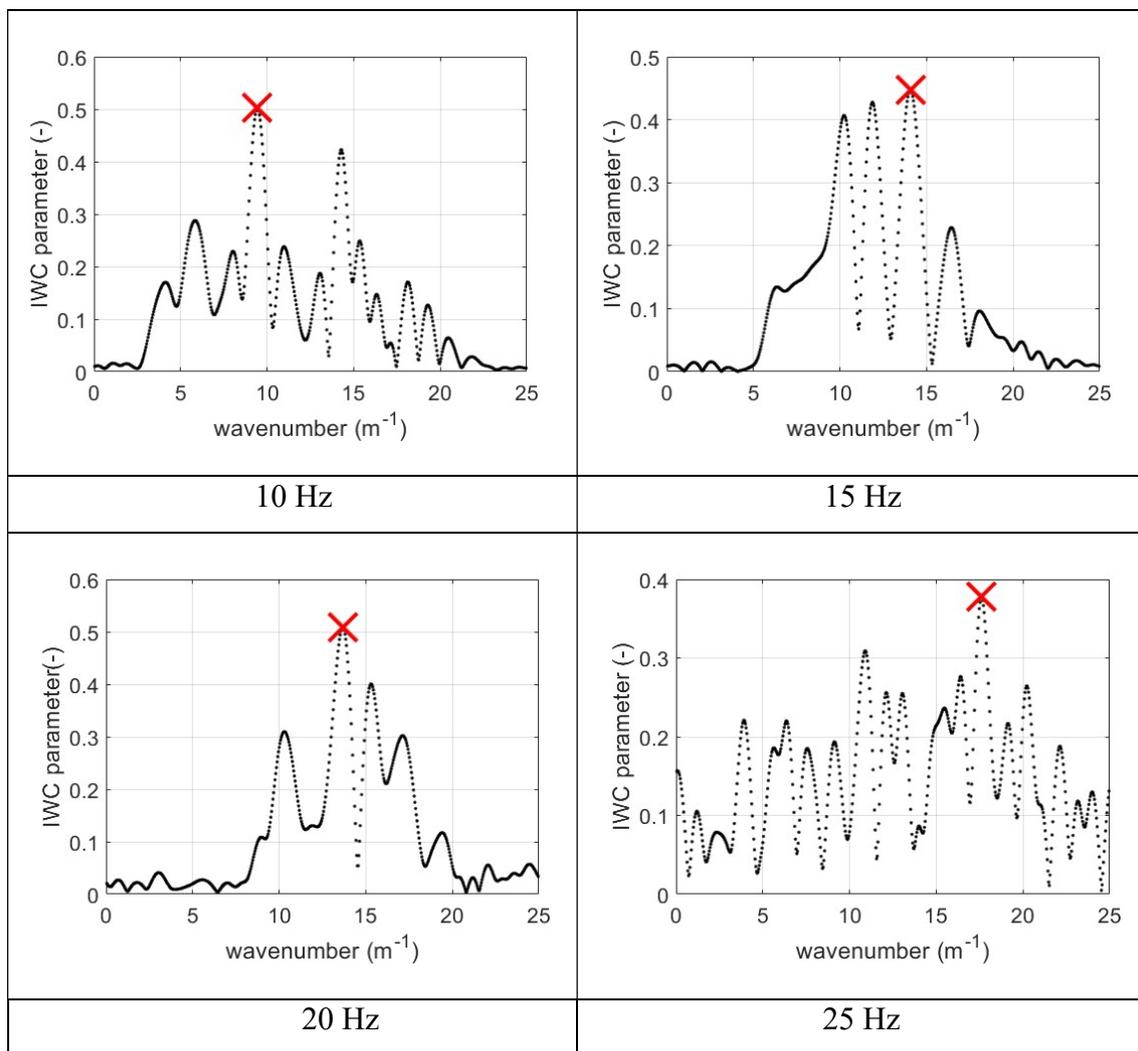
Figure 3.18: IWC parameter in wavenumber for CG, for different frequencies: 10 Hz, 15 Hz, 20 Hz, 25 Hz. The x represent the IWC that maximise the correlation between frequency and wavenumber.

area have a shape similar to a probability function, with only few peaks, whereas the graph in the non propagative area shows a large number of peaks with a regular occurence and a similar height.

A linear fit of the data reported in the propagative dispersion graphs does not match the distribution of the data of the dispersion graphs. As a consequence, TH cannot be applied in this case of reactive turbulent plume. Conversely, a function given by a ratio of polynomials fits well our data in the propagation area:

$$k_{3,p} = \frac{af+b}{f+c} \qquad (3.19)$$

In the following we assume the interpolating function for the finest grid as the correlation-law. The terms a, b and c, for the finest grid are: $a = 250.2 \text{ m}^{-1}$, $b = 307.2 \text{ m}^{-1}\text{s}^{-1}$ and $c = 387.0 \text{ s}^{-1}$. A horizontal asymptote is placed at 250.2 m^{-1}(the 99% of this asymptote is reached for a frequency of 38 kHz). When used to extrapolate, the interpolation for the grid spacing 0.25 m highly under-predicts the wavenumbers at high frequencies, while the remaining two give comparable results.

With reference to the wave propagation theory [121], in Figure 3.19 the phase velocity, it means the rate at which a wave propagates, and the group velocity, it means the rate of the wave-packet that carries the information of the signal, here the *tke,* are shown (solid lines) in the stream-wise wavenumber domain ($k_{3,p}$). In particular the group and phase velocity obtained with the fitting Eq. (3.19) are shown in Figure 3.19 with solid lines. If the dispersion curve is linear, the group velocity and the phase velocity coincide. Since the validity of TH means a linear correlation-law, if the TH can be applied, the group velocity and the phase velocity should coincide. Here, instead, the two velocities are different, as evident from Figure 3.19. Different Authors, such as Goldschmidt et al. [70], Del Àlamo and Jimenez [122] and Moin [123], state that the convection velocity is the phase velocity. For our plume, the phase velocity is:

$$V_{ph}(k_{3,p}) = 2\pi \frac{f}{k_{3,p}} \qquad (3.20)$$

and the group velocity:

$$V_g(k_{3,p})=2\pi \frac{d\,f}{d\,k_{3,p}} \qquad (3.21)$$

With reference to the correlation-law in Eq. (3.19), the group velocity here is always higher than the phase velocity. Both the velocities have an increasing trend. For the phase velocity this is confirmed by the consideration of Fisher and Davies [66] and Goldschmidt et al. [70] that the turbulent structures at the lower wavenumbers move slower than at the higher wavenumbers. The trend of the convection (phase) velocity in the wavenumber $k_{3,p}$ domain is analogous to the one shown by Goldschmidt et al.[70].

The ratio of polynomials of Eq. (3.19) was not the only fitting function used, but also a 2nd degree polynomial was applied:

$$k_{3,p} = a\,f^2+b\,f+c \qquad (3.22)$$

Here the terms *a, b* and *c,* for the finest grid are: $a = -1.17 \cdot 10^{-3}$ m^{-1}, $b = 0.63$ m^{-1}s^{-1} $c = 0.67$ s^{-1}. In Figure 3.19 the group and phase velocities obtained by applying Eqs. (3.20-3.21) to Eq. (3.22) are shown in dashed lines compared with the ones obtained with Eq. (3.19) represented with solid lines. The fitting Eqs. (3.19-3.22) produces velocities with similar trends. Thus, we can suppose that also the use of a 2nd degree polynomial as
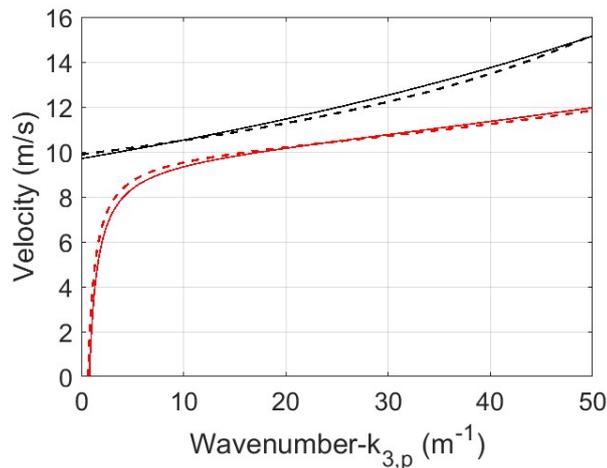
Figure 3.19: V_g and V_{ph} obtained with the ratio of polynomial fitting (black and red solid lines) and with the 2nd degree polynomial (dashed lines) in the wavenumber domain.

interpolating function would give similar results.

In Figure 3.20 the values of the time-averaged vertical velocity component along the centre-line from 1 m above the ground to 9.5 m, are reported. The velocity profile is variable, and its maximum 10.2 m/s. If we compare the spatial distribution of the mean velocity in the region where the correlation is found with the group and phase velocities in the wavenumber domain, we can see that the higher the wavenumber the more the phase velocity exceeds the maximum velocity along the region of interest. Goldschmidt et al. [70] obtained the same results but having a constant spatial distribution of time-averaged velocity.

The group velocity, which gives the propagation of the envelope of the signal, here the *tke*, for $k_{3,p} = 0$, is 9.7 m/s, which is not far to 10.2 m/s that is the value of the maximum velocity along the centre-line. This value (10.2 m/s) is reached by the phase velocity at about 21 m^{-1}. Furthermore, $V_g(k_{3,p} = 0)$ (9.7 m/s) is reached by the phase velocity at about 14 m^{-1}.

The *tke* spectra in the wavenumber domain are obtained by reducing the *tke* spectra in the frequency domain with the IWC method. In Figure 3.21 for the different grids, the *tke* spectra in the wavenumber domain are shown. These spectra are calculated using the
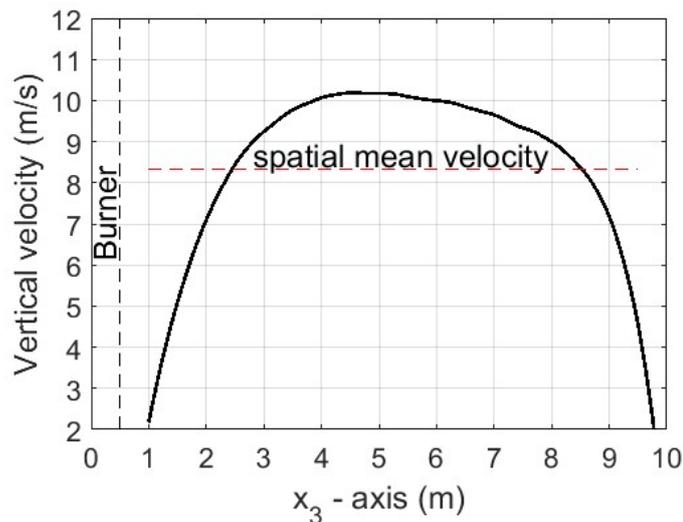
Figure 3.20: Vertical time-averaged velocity along the vertical centre-line of the domain

correlation-law, Eq. (3.19). Qualitatively these spectra are similar to those presented in Figure 3.13. As for the frequencies (Figure 3.13), the inertial subrange, characterized by the -2/3 power law feature, is captured in all the three grids. As for the frequencies, the "attenuated region" is bounded by the wavenumbers k_{fc} (lower limit) and k_c (upper limit). We observed different behaviours for the two coarser grids and for the finer one.

For the two coarser grids after the region characterized by the -2/3 power law feature, as for the frequencies, a sharp decrease (attenuated region) begins. For the finest grid (0.0625 m), in the *tke* spectrum there is a slight departure from the -2/3 power law at 14 m^{-1}, followed by a sharp decrease at 23.8 m$^{-1}$ (both are indicated with dashed line in Figure 3.21c together with k_c). If on one side k_c increases evidently the finer the grids, this cannot be seen for k_{fc} that for the finer grid is close to the one found for $\Delta x=0.125$ m. This suggests that for the finest grid, the lower bound of the attenuated region, k_{fc}, is not where the slight departure from the - 2/3 power law begins, but it is where we appreciate a sharp decrease from the slowly decreasing trend due to the non-linearity of the correlation-law. As already discussed, in Figure 3.13 the *tke* spectra in the frequency domain shows the -2/3 power law feature followed by a sharp decrease (attenuated region). The preservation of the -2/3 power law feature from the frequency to the wavenumber domain implies a linear transformation, then the applicability of TH. This applies for the whole inertial subrange to the two coarser grids. For the finest grid, instead, the departure from the -2/3 power law implies a deviation from the TH that occurs inside the inertial sub-range.

In Figure 3.22 the *tke* spectra for the three grids are shown together. With the dashed lines we indicate the wavenumber at which $V_g(k_{3,p} = 0)$ is reached by the phase velocity (14 m^{-1}) and the wavenumber at which for the finest grid, the sharp decrease begins (23.8 m^{-1}). It can be noted that, only for the finer grid, the sharp decrease exceeds 14 m^{-1}. At this wavenumber begins the slight departure from the - 2/3 power law, hence, the deviation from the TH. The true attenuation due to the implicit filtering appears then at $k_{fc} = 23.8$ m^{-1}, as reported in Tab. 3.12. It seems that, for our plume, the wavenumber at which begins the deviation from the TH could be the one at which $V_g(k_{3,p} = 0)$ is reached
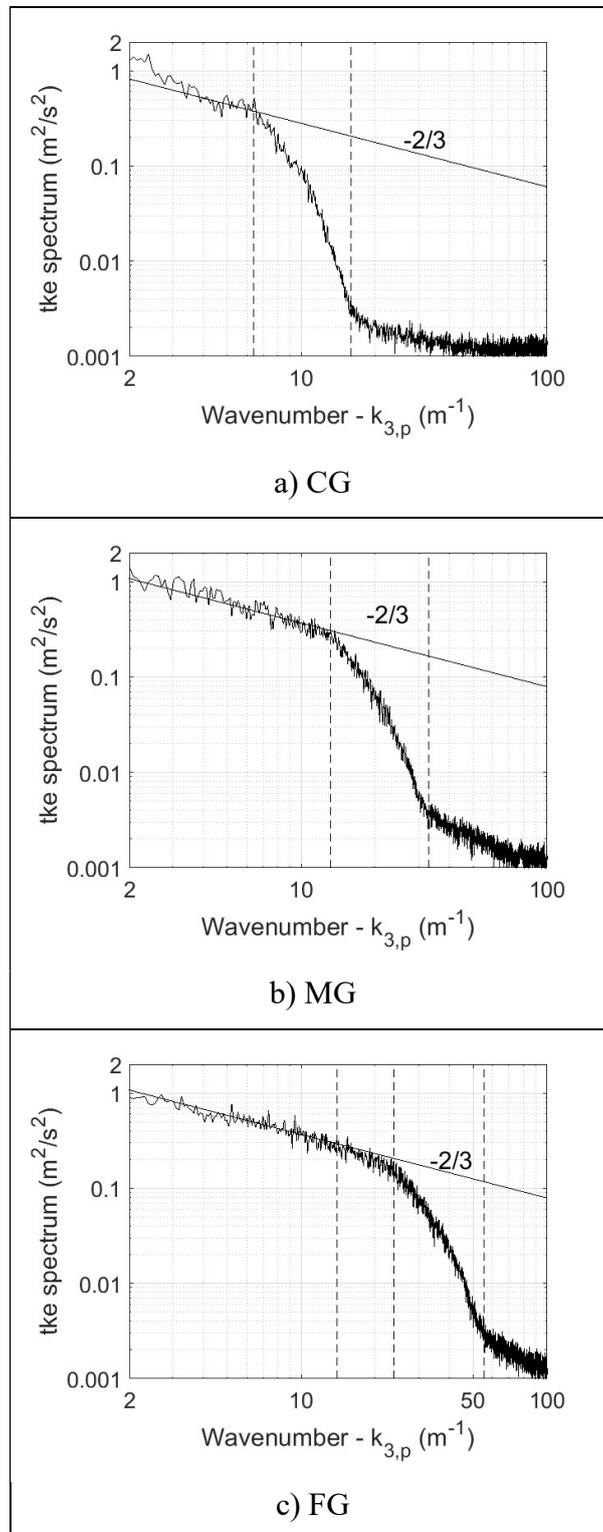
Figure 3.21: *tke* spectra in the propagative wavenumber domain at 5 m of height. The dashed lines are k_{fc} and k_c.
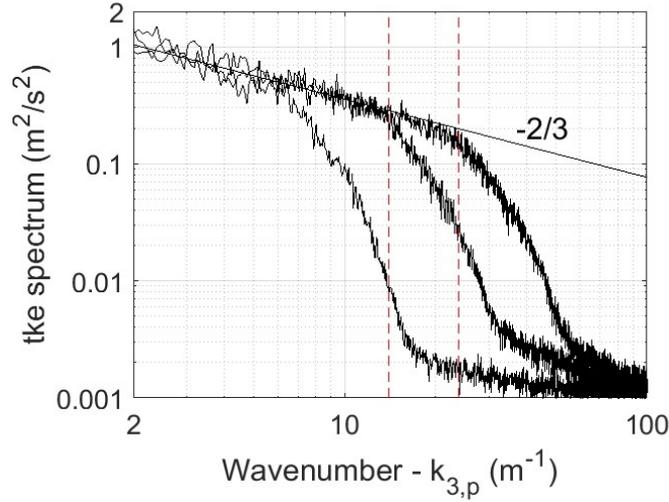
Figure 3.22**:** *tke* spectra in the wavenumber domain at 5 m of height. The dashed red
line highlights the wavenumber 14 m^{-1} and 23.8 m^{-1}.

Table 3.12: Values of wavenumber bounding the "attenuated region" in the plume.

	k_{fc} (m^{-1})			k_c (m^{-1})		
	CG	MG	FG	CG	MG	FG
From data	6.4	13.1	23.8	16.0	33.0	55.5
IWC	6.9	13.6	23.6	16.2	31.3	53.6
FDS	-	-	-	12.6	25.1	50.3
FDS/2	6.4	12.6	25.1	-	-	-
π/2	-	-	-	16.0	32.0	64.0

by the phase velocity.

Since the *tke* spectra and their bounding frequencies are only available at the end of
time expensive numerical calculations, we decided to look for practical rules to predict
f_{fc} and f_c (reported in Tab. 3.10) to have an *a priori* idea of the significant resolved scales
of the problem.

At first, we considered the frequency corresponding to the spectral cut-off
wavenumber given by FDS [91] as:

$$k_{c,FDS} = \frac{\pi}{\Delta x} \tag{3.23}$$

where Δx is the grid spacing. The corresponding frequency, indicated as $f_{c,FDS}$ and reported in Tab. 3.10, is:

$$f_{c,FDS} = \frac{U}{2\,\Delta x} \tag{3.24}$$

where U is here the time-averaged axial velocity in the node given by FDS. Since we are interested in an *a priori* analysis, an estimation of this value can be also obtained with analytical models like the McCaffrey one [104], already described in Par. 3.1.3, which showed a good agreement up to the intermittent zones. When comparing f_{fc} and f_c with $f_{c,FDS}$, no matching is obtained. The frequency $f_{c,FDS}$ is always lower than f_c, and higher than f_{fc}. The disagreement is certainly due to the choice of the local mean velocity as U in Eq. (3.24). The choice of a proper convection velocity for U would certainly improve the accordance. However, here we are interested in a fast analysis and for this we move between the values available through the analytical models.

Secondly, as practical rule, we decided to adopt for f_{fc}, the half of $f_{c,FDS}$:

$$f_{fc,FDS/2} = \frac{U}{4\,\Delta x} \tag{3.25}$$

These values, also reported in Tab. 3.10, are in a good agreement with those of the lower bounding frequency f_{fc}.

Since the frequencies f_c, for the different grids, is higher than $f_{c,FDS}$, it was developed a further practical rule to obtain values closer to f_c. This practical rule differs from Eqs. (3.24-3.26) in the denominator where a $\pi/2$ is used as multiplicative coefficient of the grid spacing. This predicting bounding frequency is:

$$f_{c,\pi/2} = \frac{U}{\pi/2\,\Delta x} \tag{3.26}$$

In our plume this practical rule, also included in Tab.3.10, gives values in good agreement with f_c.

Since the *tke* spectra in the wavenumber domain are obtained by applying the correlation-law to those in the frequency domain, k_{fc} and k_c (reported in Tab. 3.12) can be identified by applying the correlation-law to f_{fc} and f_c, obtaining $k_{fc,IWC}$ and $k_{c,IWC}$. The latters identify quite accurately k_{fc} and k_c. It can be noted that for the finer grid, the parameter $k_{fc,IWC}$ seems to predict where the spectra sharply decrease at 23.8 m^{-1}, and not

the slight departure from the -2/3 power law at 14 m^{-1}. This is due to the correlation-law that deviates from the TH inside inertial sub-range, so the f_{fc} has a corresponding wavenumber k_{fc} value not aligned with the other values of the -2/3 power law range.

However, the application of the correlation-law is disadvantageous for this purpose because it implies the performance of the numerical calculations and the use of the IWC method. Thus, we decided to use practical rules, as for the frequencies, to have an *a priori* rule of thumb to have an estimation of the resolved scales. At first, we considered and reported in Tab. 3.12 , the Nyquist wavenumber $k_{c,FDS}$, defined in Eq. (3.23) and highlighted also in the User Guide [91]. This practical rule can give only a rough estimation of k_c.

Secondly, as done for the frequencies, we considered the half of $k_{fc,FDS}$ (reported in Table 3.12 as $k_{fc,FDS/2}$). A comparison shows a good agreement with the lower limit k_{fc}. It can be noted that for the finer grid, as for $k_{fc,IWC}$, the practical rule $k_{fc,FDS/2}$ predicts where the spectra sharply decrease, and not the slight departure from the -2/3 power law at 14 m^{-1}.

Finally, the wavenumber corresponding to $f_{c,\pi/2}$, which is four times the inverse of the grid spacing, is taken into account to predict k_c. This $k_{c,\pi/2}$ seems to give a good estimation of the upper limit of the "attenuated region", better than $k_{c,FDS}$. Although $k_{c,\pi/2}$ is less accurate for the finest grid than $k_{c,IWC}$, it has the advantage to give an acceptable estimation of k_c before performing the LES calculations.

3.3   CEILING JET

In our cubic domain, the ceiling jet radially spreads. Its propagation pattern has the shape of a radially expanding hollow disk. We analyse our data in the diameter along the axis x_1, where the data points are aligned and equally spaced. In Figure 3.23 for the layer below the ceiling surface, the time-averaged longitudinal, transversal, and vertical components of velocity along a diameter at 0.25 m from the ceiling surface are shown. This wall bounded shear flow is characterised by a variable distribution of time-averaged longitudinal and vertical components of velocity. Due to these variations, the *tke* is

analysed in different positions along the axis.

In Figure 3.24 the time-averaged longitudinal component of velocity for the different grids is shown. The differences between the 0.25 m grid and the cases with finer grids suggest that the results of the coarser grid are unacceptable. Due to this consideration the spectral analysis in the ceiling jet is restricted to the MG and FG.

In Figure 3.25 the *tke* spectra in the frequency domain at 1.5, 3.0 and 4.5 m from the axis are shown. Since the *tke* spectra are characterized by annoying fluctuations, which make the *tke* spectra difficult to read, the signal has been Tukey windowed using intervals of 8 s with 2 s of overlapping (see for details Appendix B.2). This analysis shows that a *tke* frequency spectrum follows the typical trend obtained with the codes adopting a LES approach with implicit filtering. After a region following the - 2/3 power law, the *tke* spectrum deviates gradually in the "attenuated region" up to a final cut-off. The region following the -2/3 power law increases by refining the grid.

As calculated in Par. 3.1.1, the smallest scales in a Kolmogorov scale analysis lie in a range ($7 \cdot 10^{-5}$ m $\leq \ell \leq 13 \cdot 10^{-5}$ m) lower than that of the Kolmogorov scale in the plume
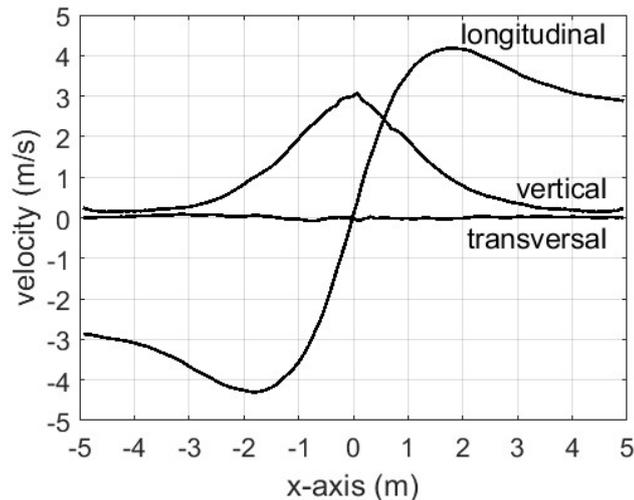
Figure 3.23: Time-averaged velocity components along the x-axis, at 0.25 m from the ceiling.
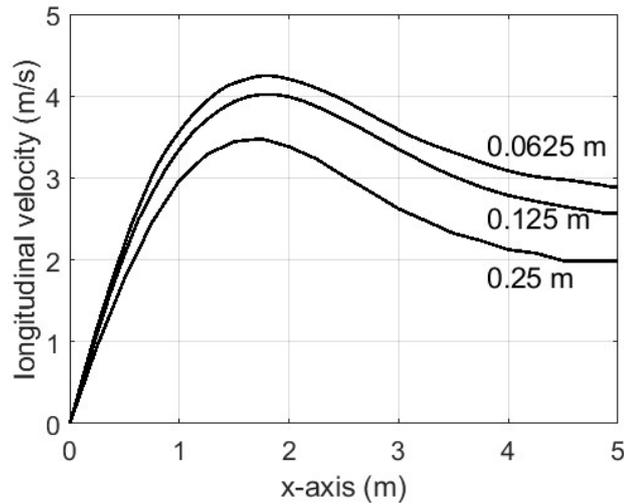
Figure 3.24: Time-averaged longitudinal velocity component along the x-axis at
different resolutions.

and far lower than the smallest grid size ($62.5 \cdot 10^{-3}$ m). We have then to expect the highest
wavenumber (connected to the Kolmogorov analysis) far higher than the wavenumber
cut-off due to the grid size. Thus, the highest possible frequency of the plume is far higher
than the resolved ones.

In the attenuated region of the *tke* spectra (see Figure 3.25), in Table 3.13 the values
of f_{fc} and f_c directly graphically estimated in Figure 3.25 are shown and labelled as "from
data". Considerable attention was paid in the graphical estimation of the bounding
frequencies. In particular, for a more precise reading, we used graphs in a linear scale
where the significant deviation from the –2/3 power law was noticed in points otherwise
not noticeable in logarithmic scale. The analysis in linear scale of the *tke* spectra in the
attenuated region shows a sharp decrease preceding a final horizontal trend. The upper
limit of the attenuated region is estimated where the prolongations of these trends
intercept.

The upper limit of the attenuated region has a tendency, more pronounced in the
finer grid, to slightly move backward when advancing away from the centre of the ceiling
jet.

MG. x_1 = 1.5 m

FG. x_1 = 1.5 m

MG. x_1 = 3.0 m

FG. x_1 = 3.0 m

MG. x_1 = 4.5 m

FG. x_1 = 4.5 m
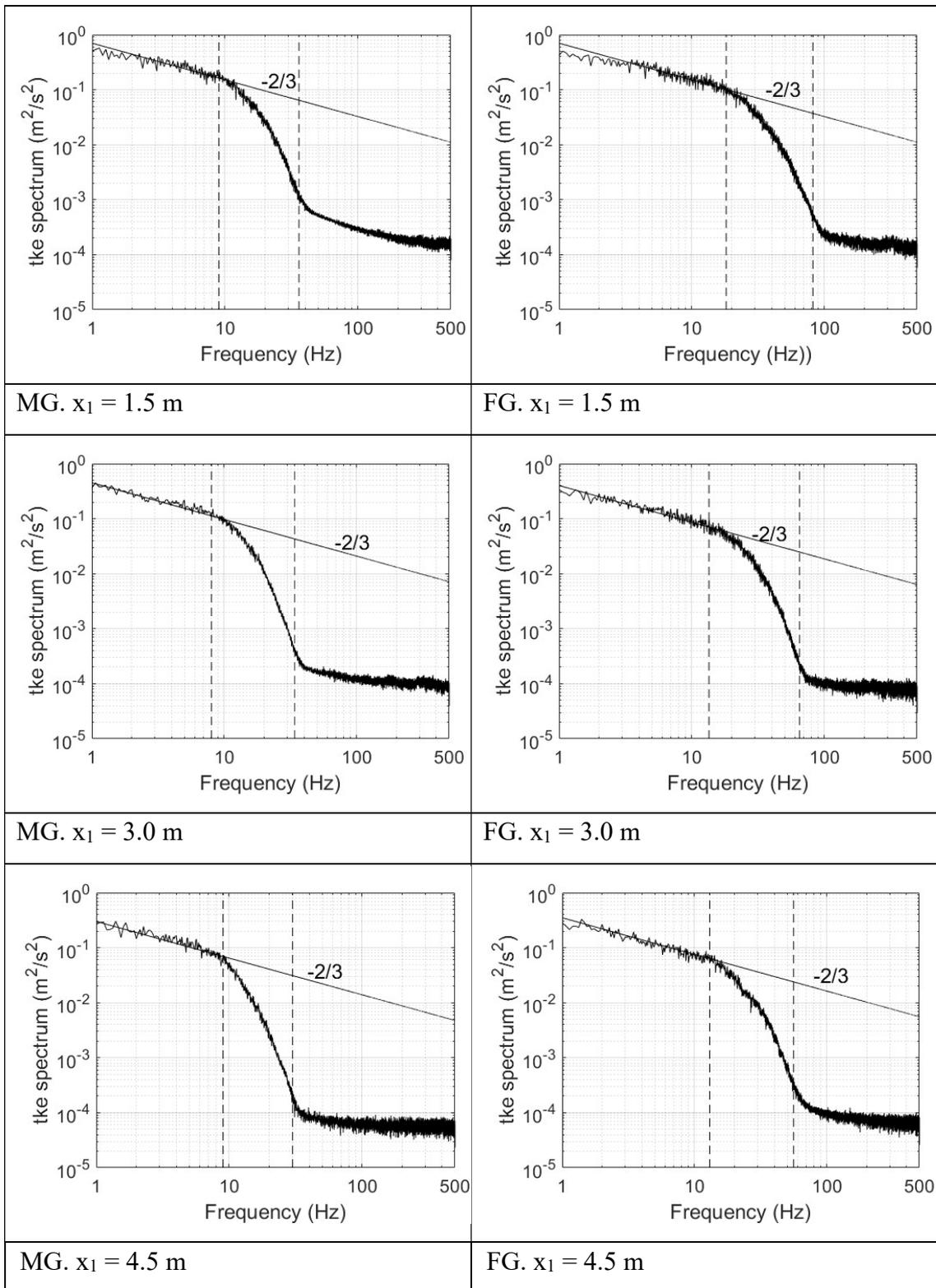
Figure 3.25: *tke* spectra in the frequency domain. x_1 = 1.5 m, x_1 = 3.0 m, x_1 = 4.5 m. The dashed lines are f_{fc} and f_c

Table 3.13: Values of frequency bounding the "attenuated region in the ceiling jet.

	x_1	f_{fc} (Hz)		f_c (Hz)	
		MG	FG	MG	FG
From data		9.0	18.2	34.0	82.0
FDS	1.5 m	-	-	16.6	34.8
FDS/2		8.3	17.4	-	-
From data		8.0	13.5	34.0	65.0
FDS	3 m	-	-	13.4	28.8
FDS/2		6.7	14.4	-	-
From data		9.0	13.0	30.0	56.0
FDS	4.5 m	-	-	10.6	23.8
FDS/2		5.3	11.9	-	-

In Figure 3.26 for the finer grid the three *tke* spectra adimensionalised with the square of the local velocity modulus are shown together. As noticeable in Figure 3.26, the attenuated regions of the spectra are shifted backward moving away from the centre of the ceiling jet. Buchhave and Velte [63] provide comparable information to the one we are interested in regarding the behaviour of the PSDs along the radius of a free round jet in air. In their experimental investigation the spectra did not show the attenuated region. The Authors show for different PSDs at different distances from the centre of a jet a backward shift similar to the one shown in Figure 3.26. As stated in [63] "the temporal energy spectra are shifted towards higher frequencies as the mean velocity increases" due to the progressively decrease of the Kolmogorov length scales. In our LES calculation the final cut-off frequency is far lower than the frequency associated to the Kolmogorov scale, then we cannot be sure that the backward shift of f_c in Figure 3.26 is the same noticed for the cut-off frequencies in the spectra shown by Buchhave and Velte [63]. If on one side one can expect that the backward shift due to the different Kolmogorov scales of the whole spectra has a direct effect on f_c, on the other, as it will be shown in the application of the IWC method, the presence of dissipation has a further significant
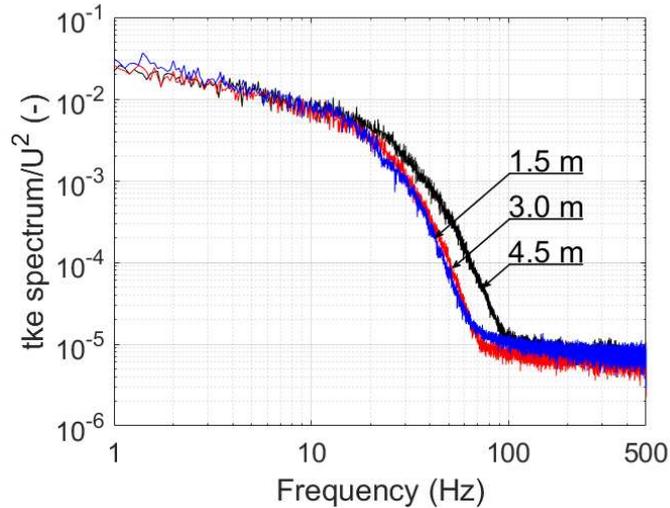
Figure 3.26: Adimensionalised *tke* spectra in the frequency domain at 1.5 m, 3.0 m and 4.5 m from the centre, FG.

indirect effect to be taken into account.

The frequency spectra are then reduced with the IWC method to obtain the correlation between frequencies and wavenumbers. The propagation pattern of the stratified combustion products, in a ceiling jet, has the shape of a radially expanding hollow disk. This trend suggests a cylindrical propagation, even though, after a certain distance from the centre, the radius of curvature of the cylindrical wave is sufficiently large that the cylindrical wave could be approximated by a plane wave. Due to these considerations, we performed for the MG the IWC method using the cylindrical wave and the plane wave, obtaining two sets of propagative and dissipative dispersion graph. In Figure 3.27 we compared, for every frequency of the dispersion graph, the wavenumber pertaining to the cylindrical wave with the one of the plane wave with the scatter plot, whereas in Figure 3.28 the same comparison is done for the dissipative wavenumbers. From these comparisons we can argue some considerations. For the propagative dispersion graphs the two data-sets are coincident. On the contrary, for the dissipative dispersion graphs the dissipative wavenumbers are lower for the IWC method that adopts the inhomogeneous cylindrical wave when compared to the plane one. This is due to the
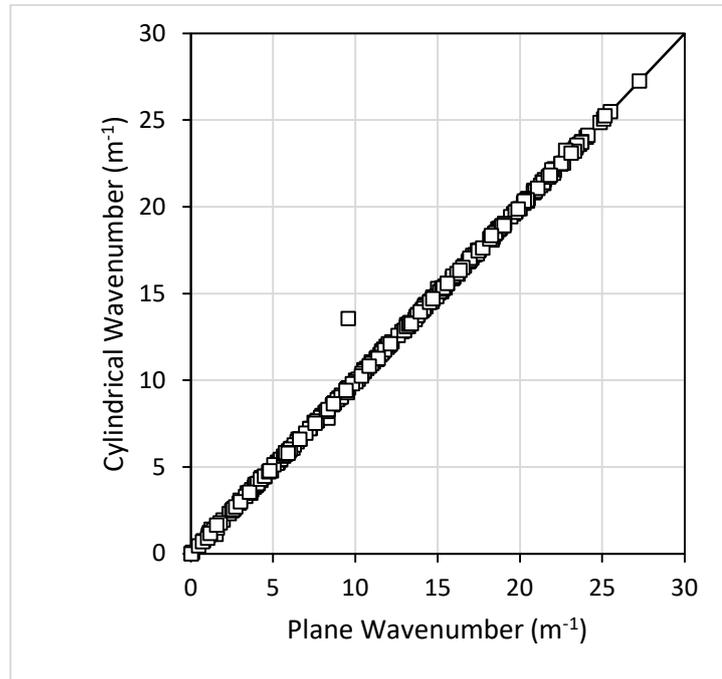
Figure 3.27: Scatter plots of the k_p obtained by the IWC method using the Cylindical wave against the ones obtained using the Plane wave.

Figure 3.28: Scatter plots of the k_d wavenumbers obtained by the IWC method using the Cylindical wave against the ones obtained using the Plane wave.

geometrical spread of a cylindrical wave (see Appendix D for details) that is not taken into account by the model of the plane inhomogeneous wave. For our ceiling jet, we used then the cylindrical inhomogeneous wave.

For the ceiling jet, the propagative and dissipative wavenumbers of the dispersion graph for the FG are shown in Figure 3.29. For the finest grid, the propagative wavenumbers are in a range from 0 m^{-1} to 76 m^{-1}, whereas the dissipative ones are in a range from 0 m^{-1} to -5 m^{-1}. For the plume case (Par. 3.1), the dissipative wavenumbers were always null. For the ceiling jet, from Figure 3.29 it is evident that the dissipative wavenumber cannot be neglected. Thus, it is possible to put in evidence an important feature of the IWC method: it allows us to assess the presence of dissipation in a wave-field.

As for the plume, a linear fit of the propagative data in the dispersion graph does not match the distribution (Figure 3.29). As a consequence, we assume again, as correlation-law, the function given by a ratio of polynomials:

$$k_{L,p} = \frac{a\,f + b}{f + c} \tag{3.27}$$
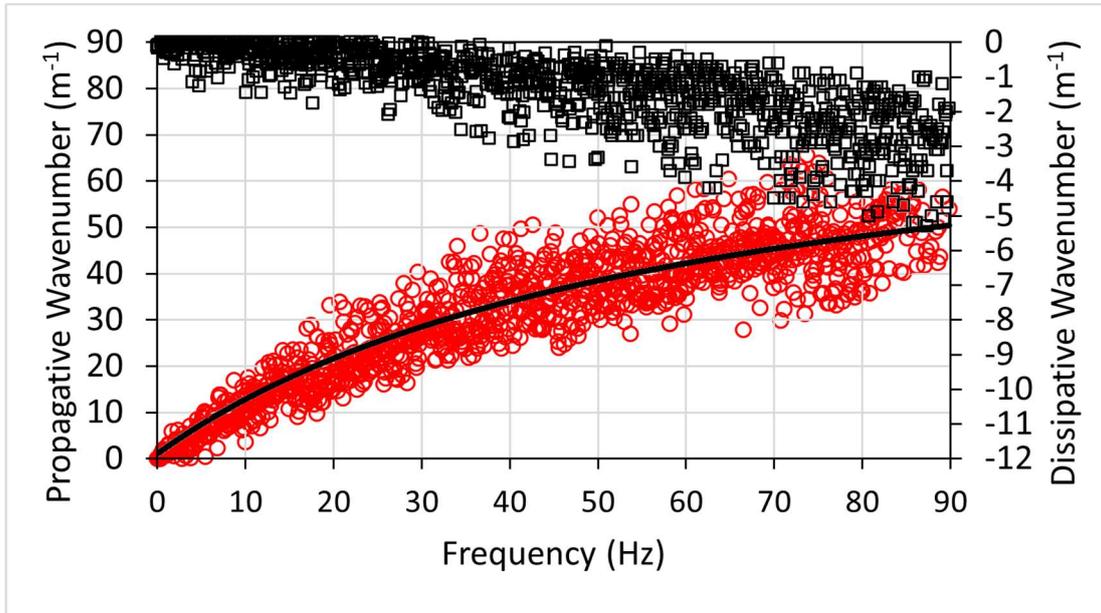
Figure 3.29: Dispersion graphs for the FG grid spacing; red disk: (O) propagative component, white square: (□) dissipative component.

The terms *a, b* and *c,* for the FG, are: $a = 83.2 \text{ m}^{-1}$, $b = 64.3 \text{ m}^{-1}\text{s}^{-1}$ and $c = 59.7 \text{ s}^{-1}$. A horizontal asymptote is placed at 83.2 m^{-1} (the 99% of this asymptote is reached for a frequency of 6 kHz) and this asymptote is far finer than the one found for the correlation-law of the plume of 250.2 m^{-1}.

With reference to the fitting function, Eq. (3.27), in Figure 3.30 the phase velocity

$$V_{ph}(k_{L,p})=2\pi\frac{f}{k_{L,p}} \tag{3.28}$$

and the group velocity

$$V_g(k_{L,p})=2\pi\frac{df}{dk_{L,p}} \tag{3.29}$$

are shown.

Qualitatively the group and phase velocities have similar features when compared to the ones of the plume. The group velocity values are always higher than the ones of the phase velocity. The higher the wavenumber the higher the velocities became. Furthermore, the trend of the phase velocity in the wavenumber $k_{L,p}$ domain is analogous to the one shown by Goldschmidt et al. [70]. The group velocity for $k_{L,p} = 0$, is 4.4 m/s then comparable to the maximum time-averaged longitudinal velocity of 4.3 m/s.
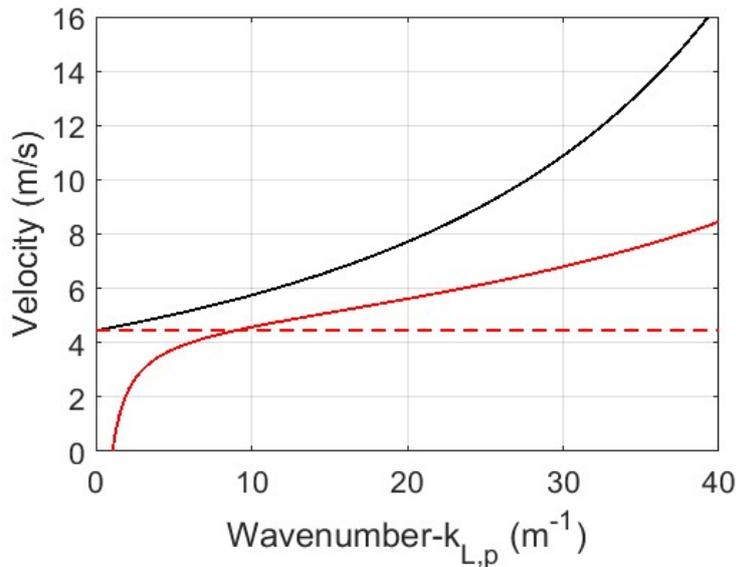
Figure 3.30: Group velocity (black line) and phase velocity (red line) in $k_{L,p.}$

There are also important differences between the group and phase velocity of the two flows. For the ceiling jet both the velocities increase more rapidly in the streamwise wavenumber domain than for the plume. The TH would imply a linear transformation between frequency and wavenumber. As a consequence, the phase velocity and the group velocity, which in the application of TH would coincide, would be independent of wavenumbers. Thus, a more rapid increase for the ceiling jet than for the plume of both the velocities in the streamwise wavenumber means a more pronounced deviation from the TH. This more pronounced departure from the TH in the shear flows, such as this ceiling jet, has been already found by Lin [50], where this Author concludes that "there is no general justification of extending Taylor's hypothesis to the case of shear flow".

The *tke* spectra in the wavenumber domain are obtained by reducing the spectra in the frequency domain with the IWC method. In Figure 3.31 for the two different grids the *tke* spectra in the wavenumber domain at 1.5, 3.0 and 4.5 m are shown. These spectra are calculated using the correlation-law, Eq. (3.27). Qualitatively these spectra are similar to those presented in Figure 3.25. The inertial subrange, characterized by the -2/3 power law feature, is captured by the two grids. In Figure 3.31 we directly graphically estimated the wavenumbers k_{fc} (lower limit) and k_c (upper limit) that bound the "attenuated region" (highlighted in Fig. 3.31 with black dashed lines). These data are reported in Table 3.14. For both the grids, in the *tke* spectra at the three different locations there is a slight departure from the -2/3 power law at 9 m^{-1} followed by a sharp decrease. The wavenumber at which the sharp decrease begins increases evidently the finer the grid (black dashed lines in Figure 3.31). As for the plume, this suggests that the lower bound of the attenuated region , k_{fc}, is not where the slight departure from the -2/3 power law begins. In Figure 3.25 the *tke* spectra in the frequency domain shows the -2/3 power law feature followed by a sharp deviation (attenuated region). The preservation of the -2/3 power law feature from the frequency to the wavenumber domain implies a linear transformation, then the TH applicability up to the frequency where the slight departure from the -2/3 power law occurs. In Figure 3.31 the red dashed line indicates the wavenumber at which $V_g(k_{L,p} = 0)$ is equal to the phase velocity (9 m^{-1}). For the MG the range between the wavenumber at which the departure from the -2/3 power law (9 m^{-1}) can be noticed and the beginning of

MG. x_1 = 1.5 m	FG. x_1 = 1.5 m
MG. x_1 = 3.0 m	FG. x_1 = 3.0 m
MG. x_1 = 4.5 m	FG. x_1 = 4.5 m
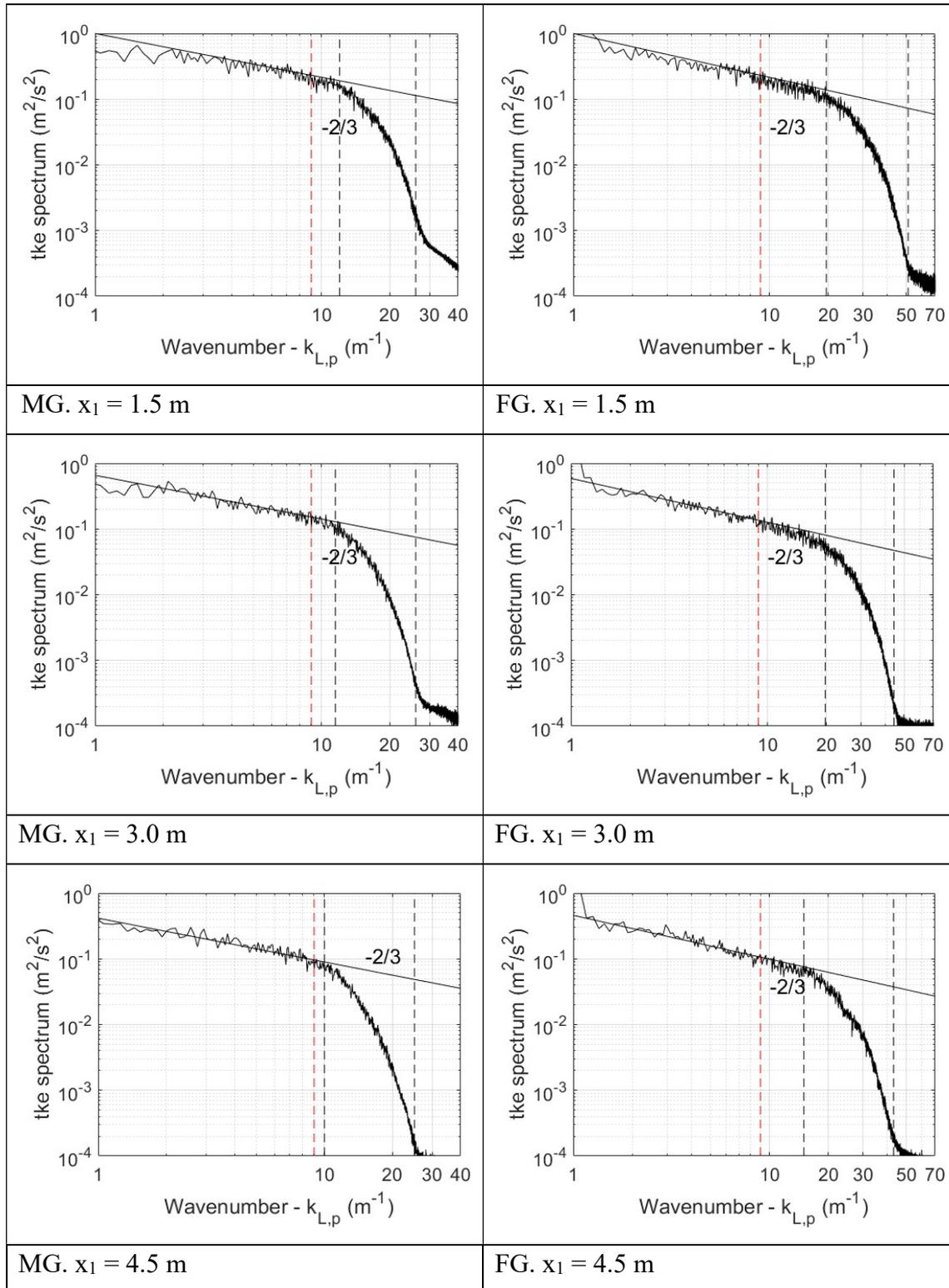
Figure 3.31: *tke* spectra in the propagative wavenumber. x_1 = 1.5 m, x_1 = 3.0 m, x_1 = 4.5 m. The dashed lines are k_{fc} and k_c.

the sharp decrease is more restricted than for FG. Thus, for the finer grid the slight departure from the -2/3 power law, and hence the deviation from the TH, is more evident than for the MG. The true attenuation due to the implicit filtering appears then where the sharp decrease begins, as reported in Table 3.14. As for our plume, it seems that, also for the ceiling jet, the wavenumber at which begins the deviation from the TH could be the one at which $V_g(k_{L,p} = 0)$ is equal to the phase velocity. Finally the backward shift of the *tke* spectra moving away from the centre of the ceiling jet already noted in the frequency domain is preserved also in the wavenumber domain.

In the following, a study of the frequencies bounding the "attenuated region" is presented (the definitions already provided in Par. 3.1 are used). With reference to the bounding frequencies f_c and f_{fc}, as for the plume, we decided to look for practical rules to predict f_{fc} and f_c to have an *a priori* idea of the significant resolved scales of the problem.

Table 3.14: Values of wavenumber bounding the "attenuated region in the ceiling jet.

	x_1	k_{fc} (m^{-1})		k_c (m^{-1})	
		MG	FG	MG	FG
From data		12.0	21.5	26.0	51.0
IWC	1.5 m	11.8	20.3	26.2	48.6
FDS		-	-	25.1	50.3
FDS/2		12.6	25.1	-	-
From data		11.5	19.7	26.0	44.0
IWC	3 m	10.8	16.3	26.1	43.9
FDS		-	-	25.1	50.3
FDS/2		12.6	25.1	-	-
From data		10.0	15.0	24.0	43.0
IWC	4.5 m	11.8	15.8	24.5	40.8
FDS		-	-	25.1	50.3
FDS/2		12.6	25.1	-	-

Using the practical rules already adopted in the plume (Par. 3.2) in Tab. 3.13 the values of bounding frequencies are shown. In more details, in Tab. 3.13, the frequencies $f_{fc,FDS/2}$, $f_{c,FDS}$ are reported for the different grids. Here, as for the plume, these practical rules imply the use of the local time-averaged U calculated with FDS because these are values of bounding wavenumbers to be transformed in frequencies. For a preliminary analysis, the Alpert analytical model [105] or a RANS can be used for an estimation of U. As can be noted in Table 3.13 for the frequency domain, the practical rule $f_{fc,FDS/2}$ can predict f_{fc} with a decreasing accuracy moving from the centre of the plume out. The practical rule $f_{c,FDS}$ seems to underpredicts f_c, in contrast to what we noticed in the plume. This issue can be due to different possible reasons: the grid that seems to not act as a filter, the choice of a wrong velocity for the transformation from the wavenumber domain to the frequency domain, the presence of dissipation (Figure 3.29) in the ceiling jet that increases the higher the frequencies. The transformation from the wavenumber to the frequency domain of the cut-offs due to the spatial implicit filtering (grid) usually involves the use of the local time-averaged velocity. The use of this velocity seems to be inappropriate, as suggested also by many Authors [58-62] for instance when the TH was not applicable. Furthermore, the analysis has shown that the dissipation revealed by the IWC method plays an important role in modifying the spectra tending to shift them backward the far is from the centre-line, where the plume develops without the dissipation. Thus, an analysis involving predictive practical rules should be done also for the cut-off wavenumbers before drawing a conclusion.

Regarding the aforementioned needs, the study of the cutoff wavenumbers k_{fc} (lower limit) and k_c (upper limit) reported in Tab. 3.14 is presented. The first available data are those graphically estimated and labelled as 'from data'. These values are immediately followed by $k_{fc,IWC}$ and $k_{c,IWC}$ obtained by applying the correlation-law, Eq. (3.27). These are able to predict rather good k_c and k_{fc}. However, these theoretical rules imply the application of the IWC method in addition to the LES calculation. For this reason, we checked the predictability of the practical rules already used for the plume: $k_{fc,FDS/2}$, $k_{c,FDS}$. This comparison allows us to draw up some considerations. Both the bounding wavenumbers $k_{fc,FDS/2}$, $k_{c,FDS}$ do not depend on the position along the flow,

where the spectra show a backward shift more pronounced the far from the centre-line. The estimation of the lower bounding wavenumber given by $k_{fc,FDS/2}$ seems to give a prediction progressively rough advancing away from the centre-line. The practical rule, $k_{c,FDS}$ also predicts k_c with a decreasing accuracy moving along the ceiling jet from the centre of the plume out. Thus, the increasing discrepancy between practical rule and values labelled "from data" moving from the centre of the plume out can be addressed by the dissipation noticed in the ceiling jet.

In the wavenumber domain a prediction of the wavenumber bounding the attenuated region with the practical rule is then possible only where the ceiling jet begins. Downstream the dissipation tends to progressively shift backwards this wavenumber. This does not apply also to the frequency domain. We can suppose then that a velocity different from the local time-averaged should be chosen. Thus, for our ceiling jet, local time-averaged velocity is not significant for the transformation from wavenumber to the frequency domain, as in the TH.

Chapter 4

CONCLUDING REMARKS

The spectral analysis of the plume and its ceiling jet is performed to obtain a deeper insight about the properties of the flows, the characteristics of the numerical code, its turbulence solver approach and the choice of the grid. A detailed review of the state of the art of the spectral analysis of the fire plumes and the ceiling jets is presented. If the spectral analysis in the frequency domain simply involves the use of the Fourier Transform, in the wavenumber domain the methodology to obtain the spectra is more challenging due to some limitations in the use of the direct method or in Taylor's hypothesis for the fire related flows: inhomogeneous turbulence, high turbulence intensity and lack of a large number of points closely spaced. A further detailed review of the methods to obtain the spectra in the wavenumber domains is presented. For the difficulties cited above, we adopt the application of the Inhomogeneous Wave Correlation (IWC) method to the turbulence, which to our knowledge was never attempted before.

Some preliminary analyses are presented drawing up some considerations about our plume and the ceiling jet.

Firstly, an estimation of the length scales is performed for both the plume and its ceiling jet. In particular, we are interested in the Kolmogorov length scale to assess whether the finest scale can be resolved by our grid. For our plume and its ceiling jet the Kolmogorov scales are far below the finest grid size ($62.5 \cdot 10^{-3}$ m). Thus, the highest wavenumber is far higher than the wavenumber cut-off due to the grid size and the highest possible frequency far higher than the resolved ones.

Secondly, a comparison between the results obtained with LES calculations and the ones obtained with the analytical models available [102-103] is performed. For the plume, the time-averaged vertical velocity along its centre-line obtained with the LES calculations is in accordance with the results of the analytical solution proposed by McCaffrey [104] up to the intermittent zone. As expected, downstream this zone the

interaction between the plume and the ceiling, which is not accounted for in the McCaffrey model [104], causes a discrepancy between the analytical model and the results of the LES calculations. For the ceiling jet the analytical solution proposed by Alpert [105] to predict the time-averaged velocity along the plume matches the results of the numerical calculation only outside the turning zone. An analysis of the flame height is done for the three grids. The results of the LES calculation are compared with Cetegen's analytical solution [103]. For the MG and the FG the accordance between the analytical model and the calculations is satisfactory, whereas for the CG the flame height is lower than the ones obtained with the finer grids and Cetegen's analytical solution [103].

Finally the turbulence intensity along the plume and along a diameter of the ceiling jet is calculated. An accepted criterion is to apply the TH to cases in which the turbulence intensity is less than 0.1. For both the flows, the values always exceed this limit. Thus it can be supposed that the TH is not applicable for our plume and its ceiling jet because they have high turbulence intensity.

Returning to the spectral analysis of our plume and ceiling jet, their discussion is articulated as:

- analysis of the *tke* spectra in the frequency domain,
- application of the IWC method,
- analysis of the *tke* spectra in the wavenumber domain.

For the ceiling jet the differences between the longitudinal component of the time-averaged velocity of the coarser grid and the ones of the finer grids bring to consider the results of the coarser grid unacceptable. As a consequence, for the ceiling jet the spectral analysis is restricted to the two finer grids, whereas for the results of the plume all the three grids are included.

The original contribution of this research is the application of the IWC method to turbulence. Here, the IWC method is used to numerically calculate the propagative and the dissipative dispersion graphs. With a fitting function the propagative dispersion graphs are interpolated, finding the functions named correlation-law. The use of a linear correlation-law, which can be derived from the TH, is not representative for both the flows. We use then as fitting function a ratio of polynomials, which is more effective.

The correlation-law is hence applied to the *tke* spectra in the frequency domain to obtain the *tke* spectra in the wavenumber domain.

We also draw up practical rules to predict the frequencies and the wavenumbers bounding the attenuated region. Regarding the frequency domain, for the plume, the bounding frequencies are in good agreement with the corresponding values of the practical rules, whereas for the ceiling jet there is a discrepancy. This can be addressed by the use of the local time-averaged velocity in the practical rule, which for the ceiling jet is not significant for the transformation from wavenumber to the frequency domain, as in the TH. Regarding the wavenumber domain, for the plume, the wavenumber bounding the attenuated region are in good agreement with the corresponding values of the practical rules, whereas for the ceiling jet the predictions are progressively rough advancing away from the centre-line.

A further result of the IWC method regards the dissipative dispersion graphs. Thus, for the plume, null dissipative wavenumbers are shown, whereas for the ceiling jet the dissipation dispersion graph shows the presence of a dissipative behaviour.

Finally, *a posteriori* assessment is conducted for the plume to evaluate the quality of our grids. In particular, we assessed the ratio between the resolved time-averaged *tke* and the total *tke*. Extending the Pope criterion [120] to our case of inhomogeneous and anisotropic turbulence, the results pertinent to the coarser grid (78%) should be considered of poor quality.

In conclusion the IWC method can be listed between the methods already used to relate frequencies and wavenumbers in the turbulence framework: the TH, the methods that apply correction to the TH, the elliptic approximation and the random sweeping model. Compared to the TH, it has the advantage that it can be applied to flows with inhomogeneous turbulence and high turbulence intensity such as the fire plume and the ceiling jet. A further advantage of the use of the IWC method is its feature of avoiding any physical model, differently from the other model mentioned above.

In our LES analyses, the IWC method allowed us to obtain accurate *tke* spectra in the wavenumber domain despite the lack of a large number of points closely spaced.

A further advantage of the IWC method is the ease of application comparable or lower than the above mentioned models that relate frequencies/wavenumbers in the turbulence framework. Thus, the IWC method can be performed without any knowledge of the characteristics of the flow such as the local time-averaged velocity or its

turbulence intensity.

Our work has also led us to conclude that the IWC method is also able to provide important information about the dissipation that is undergoing in the flow of interest. For the plume a typical propagative behaviour due to the large production of momentum from the buoyancy forces is shown, whereas for the ceiling jet, where the momentum is not produced but came from the flow of the plume, a dissipative behaviour is revealed.

A possible limitation in our analysis can be the use, as interpolating function, of a ratio of polynomials to obtain the correlation-law. Thus, this interpolating function does not derive from a physical model. However, we have used, alternatively as interpolating function a 2nd degree polynomial obtaining comparable results.

A further conclusion can be done about the use of the rule of thumb of the FDS User Guide [94] for the choice of the grid of our case study. For the coarsest grid it yields:

- unacceptable results for the longitudinal time-averaged velocity for the ceiling jet,

- a restricted inertial subrange of the *tke spectra*,

- a ratio between the resolved time-averaged *tke* and the total *tke* that does not satisfy the Pope criterion [120]*,

- a lower flame height compared to Cetegen's analytical model and to the finer grids.

Since the assessment of the fire structural resistance and of occupants' life safety involves the study of the fire plume and its ceiling jet, also for practical applications the rule of thumb should be always supported by a grid assessment analysis and by a comparison with the results of the analytical models. Furthermore, the study of the ratio between the resolved time-averaged *tke* and the total *tke* and the analysis of the *tke* spectrum are also shown to be good indicators of the quality of the grid.

Future work will concentrate on the implications of our spectral analysis on the heat transfer. In particular, the interaction between the fire plume and the ceiling JETwill be an object of study. The study of the flame height has already shown that for the coarser grid the restricted inertial subrange in the *tke* spectrum has a severe implication on the flame height that is lower than the one obtained with the finer grid and with the Cetegen's analytical model, consequently there will be an effect on how the flame will interact with its surroundings. To further our research we plan to study the implications of our spectral

analysis on the parameters of interest such as temperature and heat flux and concentration of the fire products.

During the iterations of the IWC method, the maximum of the IWC parameter in the space of the wavenumber (for example $k_{3,p}$ and $k_{3,d}$ in the plume) is obtained by an approach in which both parameters are made to vary over a range of values causing a large number of iterations. A future research perspective can consist in using an optimization algorithm based e.g. on a gradient ascent method that would allow a quicker and more accurate identification of a maximum correlation.

Finally, a future improvement in this research also regards the IWC method, that is here applied to the results of a numerical calculation of a plume and a ceiling jet. In particular, we applied the IWC method as described by Berthaut et al. [84], and no modifications were made. A fascinating future prospect is to partially revise the statistics of the method during the research of correlation between frequency and wavenumber, making it more efficient for turbulence.

Chapter 5

REFERENCES

[1] Zukoski, E.E.,(1986). Fluid Dynamic Aspects of Room Fires. *Fire Safety Science* 1: 1-30.

[2] Heskestad, G., (1998). Dynamics of the fire plume. *Philosophical Transactions of the Royal Society A: Mathematical, Physical and Engineering Sciences,* 356(1748), 2815–2833.

[3] Drysdale, D., *An Introduction to Fire Dynamics*, 2nd Edition, 2011 John Wiley & Sons, Ltd, pp. 121-179.

[4] McCaffrey, J. (1979). Purely buoyant diffusion flames: Some experimental results. *Center for Fire Research, National Engineering Laboratory, National Bureau of Standards, NBSIR*, 79-1910.

[5] Cetegen, B. M., Ahmed, T. A. (1993). Experiments on the periodic instability of buoyant plumes and pool fires. *Combustion and Flame*, 93(1-2), 157–184.

[6] Morton, B. R. (1965). Modeling fire plumes. *Symposium (International) on Combustion*, 10(1), 973–982.

[7] Alpert, R.L. (1975). Turbulent ceiling-jet induced by large scale fires. *Combustion Science and Technology*, 11, 197-213.

[8] Weng, W. G., and Hasemi, Y. (2005). Heat transfer to an unconfined ceiling from an impinging buoyant diffusion flame. *Heat and Mass Transfer*, 42(7), 652–659.

[9] Sagaut, P., *Large Eddy Simulation for Incompressible Flows*, pp. 283-303 Scientific Computation, 2006.

[10] Tennekes, H., Lumley, J. L., A First Course in Turbulence, pp. 149-196 MIT Press, Cambridge, Mass, 1972.

[11] Richardson, L.F. *Weather Prediction by Numerical Process*. Cambridge University Press, Cambridge. 1922.

[12] Davidson, P., *Turbulence: An Introduction for Scientists and Engineers*, pp. 71-

104 Oxford U. Press, New York, 2004.

[13]   Taylor, G. I. (1938). The Spectrum of Turbulence. *Proceedings of the Royal Society A: Mathematical, Physical and Engineering Sciences*, 164(919), 476–490.

[14]   Kolmogorov, A.N. (1941). The local structure of turbulence in incompressible viscous fluids at very large Reynolds numbers, *Doklady Akademii Nauk. SSSR 30*, 299-303.

[15]   Kolmogorov, A.N. (1941). On the degeneration of isotropic turbulence in an incompressible viscous fluids, *Doklady Akademii Nauk. SSSR 31*, 538-541.

[16]   Kolmogorov, A.N. (1941). Dissipation of energy in isotropic turbulence. *Doklady Akademii Nauk. SSSR*, 32, 19-21.

[17]   Reynolds, A. J., *Turbulent Flows in Engineering*, pp 80-112, Wiley, 1974.

[18]   Mandelbrot, B. B. *Multifractals and 1/f Noise*. pp 249-416. Springer,1999.

[19]   Obukhov, A. M., (1941). On the distribution of energy in the spectrum of turbulent flow, *Doklady Akademii Nauk SSSR 32(1)*, 22-24.

[20]   Heisenberg, W., (1948). Zur statistischen Theroie de Turbulenz, *Zeitschrift für Physik,* 124, 628-657.

[21]   Weizsacker, C.F. von, (1948). Das Spektrum der Turbulenz bei grossen Reynoldschen Zahlen, *Zeitschrift für Physik*124, 614-627.

[22]   Onsager, L. (1949). Statistcal Hydrodynamics, *Nuovo Cimento*, VI, IX, pp.279-287.

[23]   Battimelli, G., Vulpiani, A. (1982). Kolmogorov, Heisenberg, von Weizsacker, Onsager: un caso di scoperta simultanea, *Atti del III Congresso Nazionale di Storia della Fisica*, Palermo, pp. 169-175.

[24]   Frisch, U., *Turbulence: The Legacy of AN Kolmogorov,* pp. 57-118 Cambridge University Press, 1995.

[25]   Smagorinsky, J. (1963). General Circulation Experiments with The Primitive Equations, *Monthly Weather Review*, 91(3), 99-164.

[26]   Piomelli, U. (2014). Large eddy simulations in 2030 and beyond. *Philosophical Transactions of the Royal Society A: Mathematical, Physical and Engineering Sciences*, 372(2022), 20130320–20130320.

[27]   Ciofalo M., *La turbolenza e i suoi modelli, Fondamenti di Termofluidodinamica Computazionale*, a cura di Comini, G, Croce, G., Nobile, E., SGEditoriali,   IV

edizione.

[28]   Leonard, A. (1975). Energy Cascade in Large-Eddy Simulations of Turbulent Fluid Flows. *Advances in Geophysics*, 237–248.

[29]   Germano, M., Piomelli, U., Moin, P., and Cabot, W. H. (1991).A dynamic subgrid-scale eddy viscosity model. *Physics of Fluids A: Fluid Dynamics*, 3(7), 1760–1765.

[30]   Moin, P., Squires, K., Cabot, W., and Lee, S. (1991). A dynamic subgrid-scale model for compressible turbulence and scalar transport. *Physics of Fluids A: Fluid Dynamics*, 3(11), 2746–2757.

[31]   Deardorff, J. W. (1970). A numerical study of three-dimensional turbulent channel flow at large Reynolds numbers. *Journal of Fluid Mechanics*, 41(02), 453.

[32]   Vreman, A. W. (2004). An eddy-viscosity subgrid-scale model for turbulent shear flow: Algebraic theory and applications. *Physics of Fluids*, 16(10), 3670–3681.

[33]   Bull, J. R., Jameson, A. (2016). Explicit filtering and exact reconstruction of the sub-filter stresses in large eddy simulation. *Journal of Computational Physics*, 306, 117–136.

[34]   Ting, C.L., Hay, D.R., (1977). Thermal plumes and turbulence spectra in the atmospheric boundary layer. *Boundary-Layer Meteorology* 11, 243–263.

[35]   Papanicolaou, P. N., List, E. J. (1988). Investigations of round vertical turbulent buoyant jets. *Journal of Fluid Mechanics*, 195(-1), 341.

[36]   Dai, Z., Tseng, L.-K., Faeth, G. M. (1994). Structure of Round, Fully Developed, Buoyant Turbulent Plumes. *Journal of Heat Transfer*, 116(2), 409.

[37]   Zhou X., Luo, K. H, Williams, J.R., (2001). Large-eddy simulation of a turbulent forced plume, *European Journal of Mechanics-B-Fluids* 20, 233–254.

[38]   Chung, W., Devaud, C. B, (2008). Buoyancy-corrected k–e models and large eddy simulation applied to a large axisymmetric helium plume, *International Journal for Numerical Methods in Fluids* 58:57–8.

[39]   McGrattan, K., McDermott, R., Floyd, J., Hostikka, S., Forney, G., and Baum, H. (2012). *Computational fluid dynamics modelling of fire. International Journal of Computational Fluid Dynamics*, 26(6-8), 349–361.

[40]   Rankin, B. A., Ihme, M. and Gore, J. P. (2015). Quantitative model-based

imaging of mid-infrared radiation from a turbulent non premixed jet flame and plume. *Combustion and Flame,* 162(4), 1275–1283.

[41]   Fabregat Tomàs, A., Poje, A. C., Özgökmen, T. M., and Dewar, W. K. (2016). Dynamics of multiphase turbulent plumes with hybrid buoyancy sources in stratified environments. *Physics of Fluids*, 28(9), 095109.

[42]   Cerminara, M., Esposti Ongaro, T., and Berselli, L. C. (2016). ASHEE-1.0: a compressible, equilibrium and ash; Eulerian model for volcanic ash plumes. *Geoscientific Model Development,* 9(2), 697–730.

[43]   Kumar, A., Verma, M. K. (2018). Applicability of Taylor's hypothesis in thermally driven turbulence. *Royal Society Open Science*, 5(4), 172152.

[44]   Husted, B., (2017). Turbulent mixing in the lower part of the smoke layer using the fire dynamic simulator, Novi Sad, 1st *International Symposium Knowledge FOr Resilient soCiety K-FORCE.*

[45]   Shukla, A. K., Dewan, A. (2019). Flow and thermal characteristics of jet impingement on a flat plate for small nozzle to plate spacing using LES. International *Journal of Thermal Sciences*, 145, 106005.

[46]   Grenson, P.; Deniau, H. (2017). Large-Eddy simulation of an impinging heated jet for a small nozzle-to-plate distance and high Reynolds number. *International Journal of Heat and Fluid Flow*, 348-363.

[47]   Xu, L.; Zhao, X.; Xi, L.; Ma, Y.; Gao, J.; Li, Y. Large-Eddy Simulation Study of Flow and Heat Transfer in Swirling and Non-Swirling Impinging Jets on a Semi-Cylinder Concave Target. *Applied Science* 2021, 11, 7167.

[48]   MacMahan, J., Reniers, A., Ashley, W., and Thornton, E. (2012). Frequency-wavenumber velocity spectra, Taylor's hypothesis, and length scales in a natural gravel bed river. *Water Resources Research*, 48(9).

[49]   Grant, H. L., Stewart, R. W., and Moilliet, A. (1962). Turbulence spectra from a tidal channel. *Journal of Fluid Mechanics*, 12(02), 241.

[50]   Lin, C. C. (1953). On Taylor's hypothesis and the acceleration terms in the Navier-Stokes equations, *Journal of Applied Mathematics* 10, 295.

[51]   Westenberg, A. A., Rice, J. L. (1959). Further measurements of turbulence intensity in flame zones. *Combustion and Flame,* 3, 459–465.

[52]   Comte-Bellot, G.; Corrsin, S. (1971). Simple Eulerian time correlation of full-

and narrow-band velocity signals in grid-generated, 'isotropic' turbulence. *Journal of Fluid Mechanic*s, 48(2), 273–337.

[53]   Kistler, A. L., Vrebalovich, T. (1966). Grid turbulence at large Reynolds numbers. *Journal of Fluid Mechanics*, 26(1), 37–47.

[54]   Favre, A. J., Gaviglio, J. J. and Dumas, R. (1957). Space-time double correlations and spectra in a turbulent boundary layer. *Journal of Fluid Mechanics*, 2(4), 313–342.

[55]   Champagne, F. H. (1978). The fine-scale structure of the turbulent velocity field. *Journal of Fluid Mechanics*, 86(01), 67-108.

[56]   Champagne, F. H.; Harris, V. G.; Corrsin, S. (1970). Experiments on nearly homogeneous turbulent shear flow. *Journal of Fluid Mechanics*, 41(1), 81–139.

[57]   Zaman, K. B. M. Q. and Hussain, A. K. M. F. (1981). Taylor hypothesis and large-scale coherent structures. *Journal of Fluid Mechanics*, 112(-1), 379.

[58]   Mi, J.; Antonia, R. A. (1994). Corrections to Taylor's hypothesis in a turbulent circular jet. *Physics of Fluids*, 6(4), 1548.

[59]   Lumley, J. L. (1965). Interpretation of Time Spectra Measured in High-Intensity Shear Flows. *Physics of Fluids*, 8(6), 1056.

[60]   Hill, R. J. (1996). Corrections to Taylor's frozen turbulence approximation. *Atmospheric Research*, 40(2-4), 153–175.

[61]   Gledzer, E. (1997). On the Taylor hypothesis corrections for measured energy spectra of turbulence. *Physica D: Nonlinear Phenomena*, 104(2), 163–183.

[62]   Heskestad, G. (1965). A Generalized Taylor Hypothesis With Application for High Reynolds Number Turbulent Shear Flows. *Journal of Applied Mechanics*, 32(4), 735–739.

[63]   Buchhave, P., Velte, C. M, (2017). Measurement of turbulent spatial structure and kinetic energy spectrum by exact temporal-to-spatial mapping. *Physics of Fluids*, 29(8), 085109.

[64]   Wills, J. A. B. (1964). On convection velocities in turbulent shear flows. *Journal of Fluid Mechanics*, 20(03), 417.

[65]   Willmarth, W. W., and Wooldridge, C. E. (1962). Measurements of the fluctuating pressure at the wall beneath a thick turbulent boundary layer. *Journal of Fluid*

Mechanics, 14(02), 187.

[66] Fisher, M. J., and Davies, P. O. A. L. (1964). Correlation measurements in a non-frozen pattern of turbulence. *Journal of Fluid Mechanics*, 18(01), 97.

[67] Bradshaw, P., Ferriss., D. H. And Atwell N. P., (1967) Calculation of boundary-layer development using the turbulent energy equation. *Journal of Fluid Mechanics* 28, 593-616.

[68] Davies, A. L., Fisher, J. and Barratt, J. (1963) The Characteristic Of The Turbulence In The Mixing Region Of A Round Jet. *Journal of Fluid Mechanics* 5, 337-367.

[69] Favre, A. J., Gaviglio, J. and Dumas, R. (1967). Structure of velocity space-time correlations in a boundary. *Physics of Fluids Supplement* 10, 5138-5145.

[70] Goldschmidt, V. W., Young, M. F. and Ott, E. S. (1981) Turbulent convective velocities (broadband and wavenumber dependent) in a plane jet. . *Journal of Fluid Mechanics* 105, 327–345.

[71] Geng, C., He, G., Wang, Y., Xu, C., Lozano-Durán, A., and Wallace, J. M. (2015). Taylor's hypothesis in turbulent channel flow considered using a transport equation analysis. *Physics of Fluids*, 27(2), 025111.

[72] Wallace, J. M. (2014). Space-time correlations in turbulent flow: A review. *Theoretical and Applied Mechanics Letters*, 4(2), 022003.

[73] Kraichnan, R. H. (1964). Kolmogorov's Hypotheses and Eulerian Turbulence Theory. *Physics of Fluids*, 7(11), 1723.

[74] Tennekes, H. (1975). Eulerian and Lagrangian time microscales in isotropic turbulence. *Journal of Fluid Mechanics*, 67(03), 561.

[75] Wilczek, M. and Narita, Y. (2012). Wave-number–frequency spectrum for turbulence from a random sweeping hypothesis with mean flow. *Physical Review E*, 86(6).

[76] Narita, Y. (2018). Space–time structure and wavevector anisotropy in space plasma turbulence. *Living Reviews in Solar Physics*, 15(1).

[77] Narita, Y. (2014). Four-dimensional energy spectrum for space-time structure of plasma turbulence. *Nonlinear Processes in Geophysics*, 21(1), 41–47.

[78] Wilczek, M., Stevens, R.; Narita, Y., Meneveau, C. (2014). A wavenumber-frequency spectral model for atmospheric boundary layers. *Journal of Physics:*

Conference Series, 524(), 012104.

[79] He, G.-W. and Zhang, J.-B. (2006). Elliptic model for space-time correlations in turbulent shear flows. *Physical Review E*, 73(5).

[80] Zhao, X. and He, G.W. (2009). Space-time correlations of fluctuating velocities in turbulent shear flows. *Physical Review E*, 79(4).

[81] Marple, S. L. (1987). *Digital Spectral Analysis with Applications*. Prentice-Hall, Englewood Cliffs, NJ.

[82]   Grosh, Karl; Williams, Earl G. (1993). Complex wave-number decomposition of structural vibrations. *The Journal of the Acoustical Society of America*, 93(2), 836–.

[83] McDaniel, J. G., Shepard, W. S., (2000). Estimation of structural wave numbers from spatially sparse response measurements. *The Journal of the Acoustical Society of America*, 108(4).

[84] Berthaut, J., Ichchou, M.N., Jezequel, L., (2005). K-space identification of apparent structural behavior. *Journal of Sound and Vibration*. 280, 1125–1131.

[85] Van Damme, B., Zemp, A. (2018). Measuring Dispersion Curves for Bending Waves in Beams: A Comparison of Spatial Fourier Transform and Inhomogeneous Wave Correlation. *Acta Acustica United with Acustica*, 104(2), 228–234.

[86] Santoni, A., Bonfiglio, P, Fausti, P. and Pompoli F. (2018) Alternative method to the Oberts technique to measure the complex elastic modulus of viscoelastic materials, *Noise Control Engineering Journal*, 67 (1).

[87] Ichchou, M.N. Bareille and O. Berthaut J. (2008). Identification of effective sandwich structural properties via an inverse wave approach. *Engineering Structures* , 30(10), 2591–2604.

[88] Cherif, R., Chazot, J. D. and Atalla, N. (2015). Damping loss factor estimation of two-dimensional orthotropic structures from a displacement field measurement. *Journal of Sound and Vibration*, 356, 61–71.

[89] Tufano, G., (2020). *k-space analysis of complex large-scale periodic structures*, Phd. Thesis Advisor: Ichchou, M. Desmet, W. and Bareille O.

[90] Tufano, G., Errico, F., Robin, O., Droz, C., Ichchou, M., Pluymers, B., Atalla, N. (2020). K-space analysis of complex large-scale meta-structures using the

Inhomogeneous Wave Correlation method. *Mechanical Systems and Signal Processing*, 135, 106407.

[91]   National Institute of Standards and Technology (NIST), *Special Publication 1019-5, Fire Dynamics Simulator User's Guide, 5th Ed., FDS Ver. 5, 2007.*

[92]   NUREG-1824, *Verification and Validation of Selected Fire Models for Nuclear Power Plant Applications Volume 7: Fire*

[93]   Cox G., Kumar S., *The SFPE Handbook of Fire Protection Engineering*, chapter Modeling enclosure Fires Using CFD, 3rd edition, Society of Fire Protection Engineers, pp. 3-205 till 3-207, 2002.

[94]   National Institute of Standards and Technology (NIST), *Special Publication 1019, Fire Dynamics Simulator User's Guide, 6th Ed., FDS Ver. 6.7.1, 2018.*

[95]   National Institute of Standards and Technology (NIST), *Special Publication 1018-1, Fire Dynamics Simulator Technical Reference Guide: Mathematical Model, 6th Ed., FDS Ver. 6.7.1,* 2018.

[96]   McDermott R., Mcgrattan, K.B. and Floyd, J., (2011). A Simple Reaction Time Scale for Under-Resolved Fire Dynamics. *Fire Safety Science* 10: 809-820.

[97]   Magnussen, B. F. and Hjertager, B. H. (1976). On mathematical modeling of turbulent combustion with special emphasis on soot formation and combustion. *In 16th Symp. (Int.) on Combustion*, Pittsburgh.

[98]   Ertesvag, I. S. and Magnussen, B. F. (2001) The eddy dissipation turbulent energy cascade model. *Combustion Science and Technology*.

[99]   National Institute of Standards and Technology (NIST), *Special Publication 1018-3, Fire Dynamics Simulator Validation's Guide, 6th Ed., FDS Ver. 6.71,* 2018.

[100] Ewins, D.J. (2000) Model validation: Correlation for updating. *Sadhana* 25, 221–234. doi.org/10.1007/BF02703541.

[101] Vacher, P., Jacquier, B., Bucharles A. (2010), Extensions of the MAC criterion to complex modes. *Proceeding of ISMA 2010 including USD* 2713-2726.

[102] Turner, J S (1969). Buoyant Plumes and Thermals. *Annual Review of Fluid Mechanics*, 1(1), 29–44.

[103] Cetegen, B. M.; Zukoski, E. E.; Kubota, T. (1984). Entrainment in the Near and Far Field of Fire Plumes. *Combustion Science and Technology*, 39(1-6), 305–331.

[104] McCaffrey, B. *SFPE Handbook of Fire Protection Engineering,* chapter *Flame Height,* 2nd ed., Society of Fire Protection Engineers and National Fire Protection Association, Quincy, MA, pp. 2-1–2-8 (1995).

[105] Alpert, R.L. (1972). Calculation of response time of ceiling-mounted fire detectors. *Fire Technol*ogy 8, 181–195.

[106] Shabbir, A., and George, W. (1994). Experiments on a round turbulent buoyant plume. *Journal of Fluid Mechanics,* 275, 1-32.

[107] Antonia, R., Prabhu, A., and Stephenson, S. (1975). Conditionally sampled measurements in a heated turbulent jet. *Journal of Fluid Mechanics*, 72(3), 455-480.

[108] White, F.M., *Heat and Mass Transfer*, Addison-Wesley, Reading (MA), 1988, pp 677-88

[109] Heskestad, G. *SFPE Handbook of Fire Protection Engineering, chapter Fire Plumes, Flame Height and Air Entrainment.* Springer, New York, 5th edition, 2016.

[110] Delichatsios M.A.(1984) Flame heights in turbulent wall fires with significant flame radiation. *Combustion Science and Technology*, 39:195–214.

[111] Steward, F.R., Prediction of the height of buoyant diffusion flames. *Combustion Science and Technology*,2(4):203–212, 1970.

[112] Heskestad, G., (1983) "Luminous Heights of Turbulent Diffusion Flames," *Fire Safety Journal*, 5, pp. 103–108.

[113] McDermott, R. Mcgrattan, K. abd Floyd, J. (2011). A Simple Reaction Time Scale for Under-Resolved Fire Dynamics. *Fire Safety Science*. 10. 809-820.

[114] Romano, G. P. (1991). Analysis of two-point velocity measurements in near-wall flows, *Experiments in Fluids* 20, 68.

[115] Reynolds, A. J., *Turbulent Flows in Engineering*, p 91, Wiley, 1974.

[116] Tong, Chenning; Warhaft, Z. (1995). Passive scalar dispersion and mixing in a turbulent jet. *Journal of Fluid Mechanics*, 292(-1), 1–.

[117] Ciani, F.S., Bonfiglio, P., Piva, S. (2021). IWC analysis of turbulent plume fires. *TECNICA ITALIANA-Italian Journal of Engineering Science*, Vol. 65, No. 2-4, pp. 196-200.

[118] Celik, I.B., Cehreli, Z.N., Yavuz, I. (2005). Index of resolution quality for large eddy simulations. Journal of Fluids Engineering 127, 949–958.

[119] Schneider K. and Vasilyev O. (2010). Wavelet methods in computational fluid dynamics. *Annu. Rev. Fluid Mech.*, 42:473–503,. 322.

[120] Pope, S. B. (2004). Ten questions concerning the large-eddy simulation of turbulent flows. *New Journal of Physics*, 6, 35–35.

[121] Brillouin L., (1960) *Wave propagation and Group Velocity*, pp. 1-23, Accademic Press.

[122] Del Álamo, J. C., and Jiménez, J. (2009). Estimation of turbulent convection velocities and corrections to Taylor's approximation. *Journal of Fluid Mechanics*, 640, 5.

[123] Moin, P. (2009). Revisiting Taylor's hypothesis. *Journal of Fluid Mechanics,* 640, 1.

[124] Harris, F. J. ,(1978). On the use of windows for harmonic analysis with the discrete Fourier transform," in *Proceedings of the IEEE*, vol. 66, no. 1, pp. 51-83.

Appendix A

FOURIER TRANSFORMS AND POWER SPECTRAL DENSITIES

The "two point correlation function" is:

$$R(\bar{r}) = \int\limits_{-\infty}^{+\infty} u_i(\bar{x},t)u_i(\bar{x}+\bar{r},t)dt \qquad (A.1)$$

where $\bar{r}$ is the pointing vector centred in the source of the signal and u is the fluctuating velocity component. The Fourier Transform of the "two point correlation function" is the Power Spectral Density (PSD) in the wavenumber domain and is expressed as:

$$PSD(\bar{k}) = \int\limits_{-\infty}^{+\infty} R(\bar{r})e^{2\pi i \bar{r}\cdot\bar{k}}d\bar{r} \qquad (A.2)$$

The "two times correlation function" can be calculated in a point, between the fluctuating velocity components in an instant and in the others:

$$R(\tau) = \int\limits_{-\infty}^{+\infty} u_i(t)u_i(t+\tau)dt \qquad (A.3)$$

where τ is the time shift. The Fourier Transform of the "two times correlation function" is the Power Spectral Density (PSD) in the frequency domain and is expressed as:

$$PSD(f) = \int\limits_{-\infty}^{+\infty} R(\tau)e^{2\pi i f \tau}d\tau \qquad (A.4)$$

The spectral analysis in the turbulence framework can be applied to many different variable, such as pressure, velocity, temperature or directly the specific turbulent kinetic energy (*tke* in the following), which is defined as:

$$tke(t) = \frac{1}{2}(u_1^2(t)+u_2^2(t)+u_3^2(t)) \qquad (A.5)$$

One of the main application of the spectral analysis consists of the direct application of the Fourier Transform to the time history of the tke

$$TKE(f) = \int_{-\infty}^{+\infty} tke(t) e^{2\pi i f t} dt \tag{A.6}$$

Eq. (A.6) allows us to obtain a complex-valued function of frequency, whose magnitude represents the amount of that frequency present in the original *tke* time history, and whose argument is the phase offset of the basic sinusoid in that frequency.

Given the fluctuations of the velocity components $u_1(t)$, $u_2(t)$ e $u_3(t)$, the Fourier Transform of each velocity component fluctuation are defined as:

$$Fu_1(f) = \int_{-\infty}^{+\infty} u_1(t) e^{-i2\pi f t} dt \tag{A.7}$$

$$Fu_2(f) = \int_{-\infty}^{+\infty} u_2(t) e^{-i2\pi f t} dt \tag{A.8}$$

$$Fu_3(f) = \int_{-\infty}^{+\infty} u_3(t) e^{-i2\pi f t} dt \tag{A.9}$$

For every fluctuation of the velocity components, it is possible to calculate the Power Spectral Density, using the Autocorrelation Theorem enunciated in Par. A.1. The *psd*(f) spectra is:

$$psd(f) = 0.5 \cdot (| Fu_1(f) |^2 + | Fu_2(f) |^2 + | Fu_3(f) |^2) \tag{A.10}$$

It can be demonstrated that the time-averaged tke ($\langle tke \rangle$ in the following) is:

$$\langle tke \rangle = \int_{0}^{+\infty} psd(f) df \tag{A.11}$$

Where *psd* is expressed as single sided.

A.1   Autocorrelation Theorem

Consider a time signal of a generical fluctuating velocity component u(t). Assuming that this signal is known over an infinitely long interval $[-\infty, +\infty]$.

The following Theorem intends to demonstrate:

$$PSD(f) = |Fu(f)|^2 \qquad (A.12)$$

where u is a generical velocity component, *PSD(f)* is the Power Spectral Density, *F* denotes the Fourier Transform. Since the two times correlation function $R(\tau)$ is:

$$R(\tau) = \int_{-\infty}^{+\infty} u(t) \cdot u(t+\tau) dt \qquad (A.13)$$

With the Fourier Transform of *R(τ)* is possible to obtain the Power Spectral Density *PSD(f)*

$$PSD(f) = \int_{-\infty}^{+\infty} R(\tau) e^{2\pi i f \tau} d\tau = \int_{-\infty}^{+\infty} \int_{-\infty}^{+\infty} u(t) \cdot u(t+\tau) e^{2\pi i f \tau} dt d\tau \qquad (A.14)$$

If it is considered $t+\tau=y$, Eq. (A.12) can be reduced as:

$$PSD(f) = \int_{-\infty}^{+\infty} \int_{-\infty}^{+\infty} u(t) \cdot u(y) e^{2\pi i f(y-t)} dt\, dy \qquad (A.15)$$

which can be further reduced as:

$$PSD(f) = \int_{-\infty}^{+\infty} \int_{-\infty}^{+\infty} (u(t)e^{-2\pi i f t}) \cdot (u(y)e^{2\pi i f y}) dt dy \qquad (A.16)$$

Since $(u(t)e^{-2\pi i f t})$ is independent of *y* and $(u(y)e^{-2\pi i f y})$ is independent of t, the two integral can be separated:

$$PSD(f) = \int_{-\infty}^{+\infty} (u(t)e^{-2\pi i f t)}) dt \int_{-\infty}^{+\infty} (u(y)e^{2\pi i f y}) dy \qquad (A.17)$$

In the second member of Eq. (A.17), it is shown the product of the two integrals of the time histories of complex numbers. One is respectively the complex conjugate of the other because the exponentials have the same modulus and argument but opposite sign. Thus, it is obtained:

$$PSD(f) = F\mathrm{u}^*(f) \cdot F\mathrm{u}(f) \tag{A.18}$$

where the asterik denotes the complex conjugate. Finally Eq. (A.12) can be rewritten as:

$$PSD(f) = |F\mathrm{u}(f)|^2 \tag{A.19}$$

Appendix B

SPECTRA CALCULATION

B.1   *tke* spectrum and *psd*(fⱼ)

This paragraph pertains the calculation of the tke spectrum and of the *psd*(f) of discrete signals.

For the *tke* spectrum, given the discrete time history of the specific turbulent kinetic energy:

$$tke(t_k) = 0.5 \cdot (u_1^2(t_k) + u_2^2(t_k) + u_3^2(t_k)) \tag{B.1}$$

it is possible to obtain the *tke* spectrum by performing the FFT algorithm using the DFT:

$$DFTtke(f_j) = \sum_{k=1}^{K} tke(t_k) \cdot e^{\left(\frac{-i2\pi(t_k-1)(f_j-1)}{K}\right)} \tag{B.2}$$

For the calculation of the *psd*(f) of discrete signals, the Power Spectral Densities of the discrete time histories of the fluctuations of the velocity components $u_1(t_k)$, $u_2(t_k)$ e $u_3(t_k)$ are calculated, respectively, with the Autocorrelation Theorem illustrated in the Appendix B.2, using *FFT* instead of the Fourier Transform. Thus, the discrete *psd(*f_j*)* is:

$$psd(f_j) = 0.5 \cdot (|DFTu_1(f_j)|^2 + |DFTu_2(f_j)|^2 + |DFTu_3(f_j)|^2) \tag{B.3}$$

The tke spectrum and *psd(*f_j*)* obtained with Eq. (B.2) and Eq. (B.3), respectively, are affected by annoying fluctuations which make them difficult to read. This issue is solved with the method described in Appendix B.2.

The *psd*(f) for the different grids at 5 m above the ground, using the method of Appendix B.2 to reduce the undesired fluctuation, are obtained and reported in Figure B.1. They show the characteristic "-5/3" power law" that follows the

Kolmogorov's theory, the attenuated region already shown in the *tke* spectra and an inertial sub-range that, as for the *tke* spectra increases refining the grid.
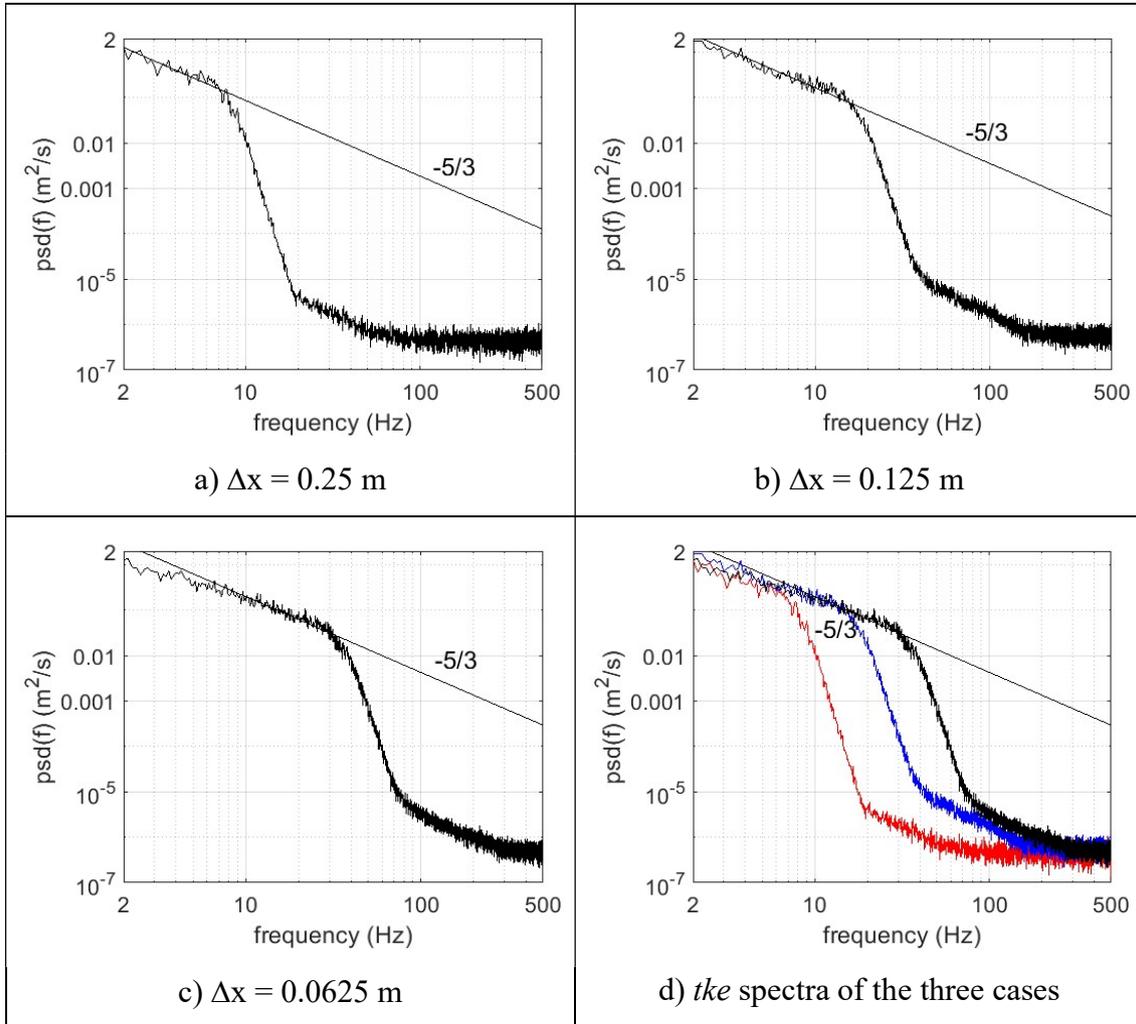

Figure B. 1: *psd*(f$_j$) at 5 m of height.

B.2   Method to reduce the fluctuations for *tke* spectrum and *psd*(f$_j$)

In Figure B.2 the *tke* spectrum is shown without any windowing technique to reduce the fluctuations. This *tke* spectra appears difficult to read. When the length of a

data set to be transformed is larger than necessary, as in our case, to provide the desired frequency resolution, a common practice is to subdivide it into finer sets and to window them. Here every set is multiplied by a Tukey window function [124]. To mitigate the "loss" at the edges of the window, the individual sets may overlap in time. In particular, the *tke* spectrum is obtained by dividing the *tke* time history, $20 \leq t_k \leq 100$, in 13 sets with 8 s of extension, with 2 s of overlapping (see Figure B.5). An ensemble average of the *tke* spectrum of every set is performed, obtaining a *tke* spectrum with reduced fluctuation (see Figure B. 4).

In Figure B.5 the *psd*(f) is shown without performing any windowing technique. The same annoying fluctuation already found in the *tke* spectrum can be noted. We reduced these fluctuations also for *psd(*f_j*)*, with the same method, dividing in sets $u_1(t_k)$, $u_2(t_k)$ and $u_3(t_k)$. On every set, for each fluctuating velocity component, the Power Spectral Density is computed. The Power Spectral Density of every fluctuating velocity component is calculated by ensemble averaging the sets. Eq. (B.3) is applied to these ensemble averaged Power Spectral Density obtaining a *psd(*f_j*)* with reduced fluctuation. In Figure B.6 the *psd*(f) obtained with this procedure is shown. Now, the readability of this *psd*(f) can be considered satisfactory for our aim.
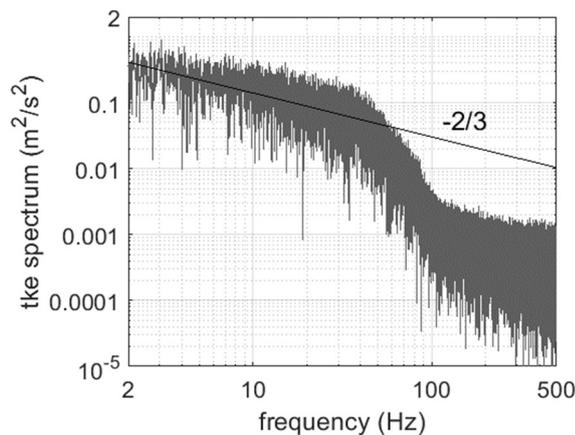

Figure B. 2: *tke* spectra without windowing.
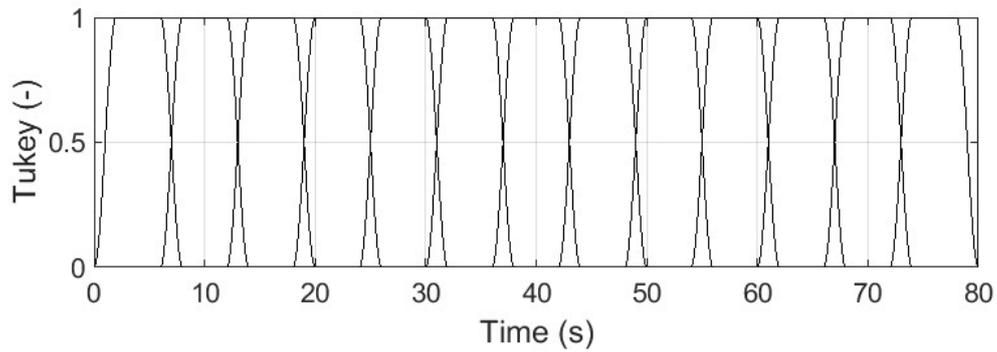
Figure B. 3: Division in sets of the signal with Tukey windows
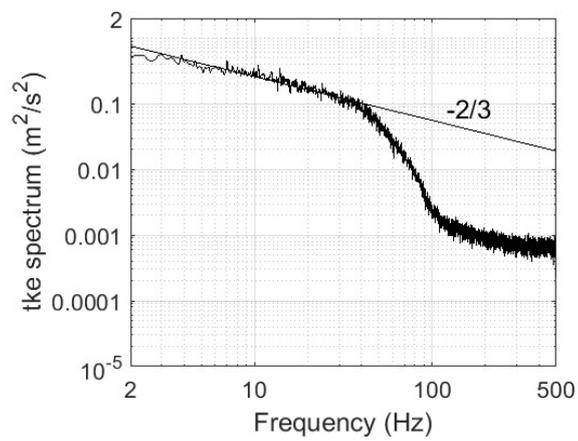

Figure B. 4: *tke* spectra with windowing.
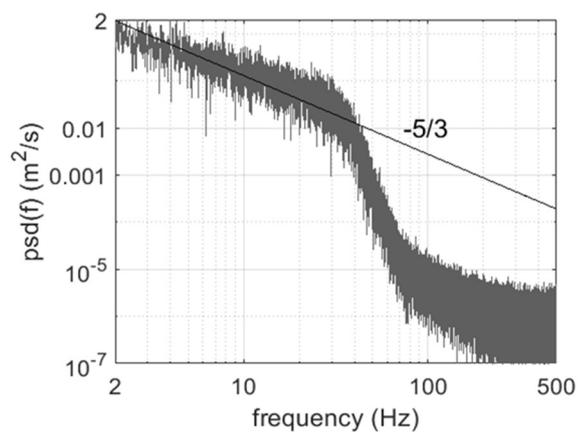

Figure B. 5: *psd*(f_j) without windowing.
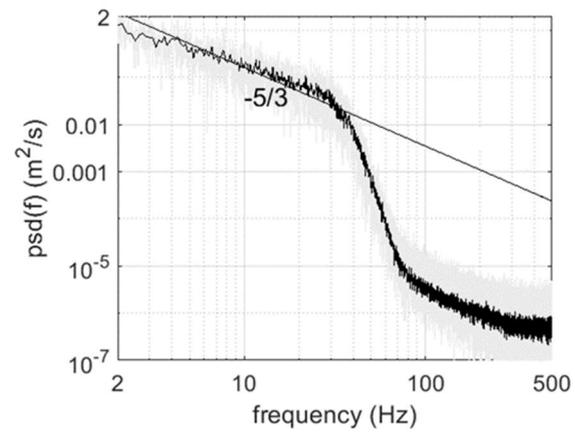
Figure B. 6: *psd*(f$_j$) with windowing.

Appendix C

TKE AND POWER SPECTRA

C.1   *tke* and power spectrum in the frequency domain

Consider a tke spectra in its inertial subrange interval, I, of wavenumbers ($\forall f \in I$).

Assuming the existence of signal $t^{-\alpha}$ known for $t > 0$, where α is our unknown of the problem.

We intends to demonstrate:

$$tke(f) \propto f^{-(2/3)} \tag{C.0}$$

Doing the one sided Fourier transform of $t^{-\alpha}$ for $t > 0$, we obtain:

$$G(f) = \int_0^{+\infty} t^{-\alpha} e^{-i2\pi ft} dt \tag{C.1}$$

The change of variable $z = i2\pi ft$ allows us to obtain:

$$G(f) = \int_0^{+\infty} \left(\frac{z}{i2\pi f} \right)^{-\alpha} e^{-z} \frac{dz}{i2\pi f} \tag{C.2}$$

which can be rewritten as:

$$G(f) = \int_0^{+\infty} (i2\pi f)^{\alpha-1} z^{-\alpha} e^{-z} dz \tag{C.3}$$

$(i2\pi f)^{\alpha-1}$ can be placed outside the integral and $G(f)$ can be rewritten as:

$$G(f) = (i2\pi f)^{\alpha-1} \int_0^{+\infty} z^{-\alpha} e^{-z} dz \tag{C.4}$$

Since the integral is not dependent on the frequency, the following proportionality relation can be written:

$$G(f) \propto f^{\alpha-1} \tag{C.5}$$

As a consequence, given a signal $\xi(t)$ such that:

$$\xi(t) \propto t^{-\alpha} \, , \, t > 0 \tag{C.6}$$

if we do its Fourier Transform we obtain:

$$\xi(f) \propto f^{(\alpha-1)} \tag{C.7}$$

If we consider as signal the time history of a component of velocity $u_i(t)$ such that:

$$u_i(t) \propto t^{-\alpha} \, , \, t > 0 \tag{C.8}$$

where α is a constant. Thus, its spectrum is:

$$|u_i(f)| \propto f^{(\alpha-1)} \tag{C.9}$$

In the interval I of frequencies of the inertial sub-range, the PSD of the time history of a fluctuating velocity component $u_i(t)$ obtained with the autocorrelation theorem (see A.1 "Autocorrelation Theorem"), for the Kolmogorov theory follows the "-5/3" power law. Thus it can be written:

$$|u_i(f)|^2 \propto f^{-(5/3)} \tag{C.10}$$

It is worth noting that the absolute value is needed because the velocity spectrum, $u_i(f)$ is a complex-valued function following the relation:

$$u_i(f) = a(f) + ib(f) \tag{C.11}$$

where i here denotes the imaginary number. Thus the square of $u_i(f)$ would allow us to obtain:

$$u_i(f) = a^2 - b^2 \tag{C.12}$$

Doing the absolute value of $u_i(f)$, instead, we obtain:

$$|u_i(f)| = \sqrt{a^2 + b^2} \tag{C.13}$$

Doing the square of Eq. (C.13) we obtain:

$$|u_i(f)|^2 = a^2 + b^2 \tag{C.14}$$

If we consider Eq (C.9), and the Kolmogorov power law, we can write:

$$-(5/3) = 2 \cdot (\alpha - 1) \tag{C.15}$$

Thus, Eq. (C.15) can be rewritten as:

$$\alpha = 1/6 \tag{C.16}$$

Furthermore, doing the square of both the side of Eq. (C.8), we obtain:

$$u_i^2(t) \propto t^{-2\alpha} \tag{C.17}$$

Introducing the variable γ such as

$$\gamma = 2\alpha \tag{C.18}$$

with Eq. (C.16) we obtain :

$$\gamma = 1/3 \tag{C.19}$$

Thus, following Eq. (C.9), doing the spectrum of the square of $u_i(t)$ we obtain:

$$|u_i^2(f)| \propto f^{(\gamma-1)} \tag{C.20}$$

Substituting Eq. (C.19) in Eq. (C.20) we obtain:

$$|u_i^2(f)| \propto f^{-(2/3)} \tag{C.21}$$

What achieved for the generic component of fluctuating velocity $u_i(t)$ can be done for the three component of fluctuating velocity $u_1(f)$, $u_2(f)$, $u_3(f)$ that are:

$$|u_1^2(f)| \propto f^{-(2/3)} \tag{C.22}$$

$$|u_2^2(f)| \propto f^{-(2/3)}$$

$$|u_3^2(f)| \propto f^{-(2/3)}$$

As a consequence, being *tke(f)*:

$$tke(f) = \frac{1}{2}(|u_1^2(f)| + |u_2^2(f)| + |u_3^2(f)|) \tag{C.23}$$

then :

$$tke(f) \propto f^{-(2/3)} \tag{C.24}$$

C.2 *tke* **and power spectrum in the wavenumber domain**

Consider a tke spectra in its inertial subrange interval, I, of wavenumbers ($\forall k \in I$). Assuming the existence of signal $x^{-\alpha}$ known over for $x > 0$, where α is our unknown of the problem.

We intends to demonstrate:

$$tke(k) \propto k^{-(2/3)} \qquad\qquad , \forall k \in I \qquad\qquad\text{(C.25)}$$

where I is the interval of wavenumbers of the inertial subrange.

If we consider as signal a component of fluctuating velocity in the space $u_i(x)$ such that:

$$u_i(x) \propto x^{-\alpha} \ , \ x > 0 \qquad\qquad\qquad\text{(C.26)}$$

Thus, its spectrum is:

$$|u_i(k)| \propto k^{(-\alpha 1)} \qquad\qquad\qquad\text{(C.27)=}$$

In the interval I of wavenumbers, the PSD of $u_i(t)$ distributed in space obtained with the autocorrelation theorem (see A.1 "Autocorrelation Theorem"), for the Kolmogorov theory follows the "-5/3" power law. Thus it can be written:

$$|u_i(k)|^2 \propto k^{-(5/3)} \qquad\qquad\qquad\text{(C.28)}$$

If we consider Eq (C.27), and the Kolmogorov power law, we can write:

$$-(5/3) = 2 \cdot (\alpha - 1) \qquad\qquad\qquad\text{(C.29)}$$

Thus, Eq. (C.29) can be rewritten as:

$$\alpha = 1/6 \qquad\qquad\qquad\text{(C.30)}$$

Furthermore, doing the square of both the side of Eq. (C.26), we obtain:

$$u_i^{\ 2}(x) \propto x^{-2\alpha} \qquad\qquad\qquad\text{(C.31)}$$

Introducing the variable γ such as

$$\gamma = 2\alpha \qquad\qquad\qquad\text{(C.32)}$$

with Eq. (C.30) we obtain :

$$\gamma = 1/3 \qquad\qquad\qquad\text{(C.33)}$$

Thus, following Eq. (C.27), doing the spectrum of the square of $u_i(x)$ we obtain:

$$|u_i^2(k)|\propto k^{(\gamma-1)} \qquad\qquad (C.34)$$

Substituting Eq. (C.32) in Eq. (C.33) we obtain:

$$|u_i^2(k)|\propto k^{-(2/3)} \qquad\qquad (C.35)$$

What achieved for the generic component of fluctuating velocity $u_i(x)$ can be done for the three fluctuating component of velocity $u_1(x)$, $u_2(x)$, $u_3(x)$ that are:

$$|u_1^2(k)|\propto k^{-(2/3)} \qquad\qquad (C.36)$$

$$|u_2^2(k)|\propto k^{-(2/3)}$$

$$|u_3^2(k)|\propto k^{-(2/3)}$$

As a consequence, being $tke(k)$:

$$tke(k)=\frac{1}{2}(|u_1^2(k)|+|u_2^2(k)|+|u_3^2(k)|) \qquad\qquad (C.37)$$

then :

$$tke(k)\propto k^{-(2/3)} \qquad\qquad (C.38)$$

Appendix D

INHOMOGENEOUS WAVE

A particular solution of an inhomogenous wave equation is the following one-dimensional plane inhomogeneous wave:

$$\sigma(x_3,t)=\sigma_0\exp(-ik_{3,p}x_3)\exp(k_{3,d}x_3)\exp(-i2\pi ft) \tag{D.1}$$

where $k_{3,p}$ stands for propagative wavenumbers and $k_{3,d}$ for dissipative wavenumbers. A further solution of an inhomogeneous wave equation is the following cylindrical inhomogeneous wave:

$$\sigma(r,t)=\frac{\sigma_0}{\sqrt{r}}\exp(-ik_{r,p}r)\exp(k_{r,d}r)\exp(-i2\pi ft) \tag{D.2}$$

where r is the radius parameter of the cylindrical coordinates.

In Fig. D.1 is shown in red the inhomogeneous wave of Eq. (D.1) and in black the homogeneous wave ($k_{3,d}\equiv0$). A clear attenuation due to the loss introduced by the term $\exp(k_{3,d}x_3)$ is shown by the inhomogeneous wave. In Fig. D.2 is shown in red the inhomogeneous wave of Eq. (D.2) and in black the homogeneous wave ($k_{r,d}\equiv0$). The amplitude reduction of the cylindrical homogeneous wave (black line of Fig. D.1) that is not present in the plane one (black line of Fig. D.2) is due to the geometrical spreading. An attenuation that further reduce the amplitude of the cylindrical wave is instead due to the loss introduced by the term $\exp(k_{3,r}r)$ in the inhomogeneous wave (red).
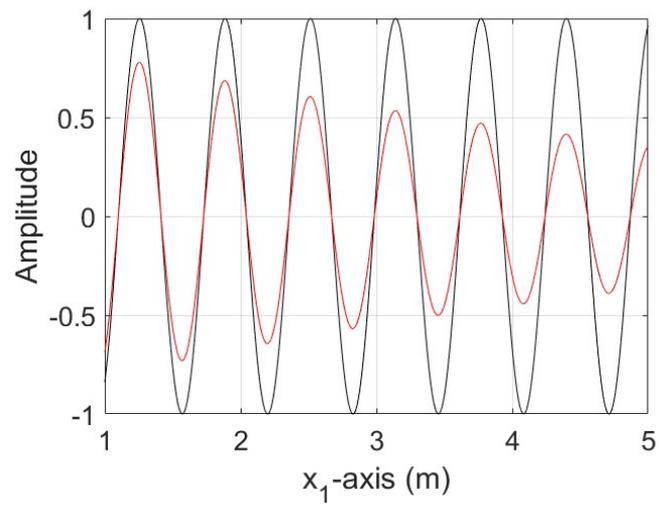
Figure D. 1: Homogeneous plane wave (black) and inhomogeneous plane wave (red).
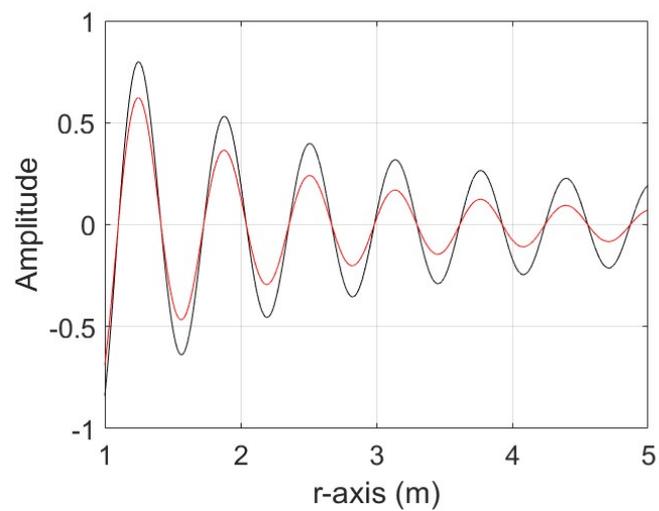
Figure D. 2: Homogeneous cylindrical wave (black) and inhomogeneous cylindrical wave (red).